Experimental investigation of wind farm flow effects

Camilla Hamre Aasnæs

Master's thesis in Ocean Technology

University of Bergen

Department of Physics and Technology

January 2022

Acknowledgements

Several people have contributed to this master's thesis, and it wouldn't be possible to complete this work without them. Therefore, I would like to acknowledge my gratitude towards supervisors, fellow students, and other contributors.

First and foremost, I would like to thank my supervisors, Jan Bartl and Gloria Stenfelt, for their excellent guidance during the experimental tests and many constructive discussions during the evaluation of the results from the experiments, as well as proofreading and feedback regarding the formalities of the thesis.

A special thanks goes to Joakim Rinke Bjørnsen for letting me take part in carrying out his experiments, sharing thoughts and theories, and providing me with all relevant guidance in MarinLab, as well as sharing all his results from his experiments.

Additionally, I would like to thank the lab engineers Robert Larsson and Harald Moen at HVL for guidance in the workshop and help with mounting the setup in the MarinLab.

Furthermore, I would like to thank my dearest friends and family for supporting me through this year.

Abstract

In order to optimize the energy efficiency in a wind farm, it will be essential to consider the arrangement of the turbines relative to each other. One of the effects that may influence the efficiency is the blockage effect. This effect can cause an overestimation of the efficiency in a wind farm, when predictions are made based only on the wake flow.

In this thesis, lab-scale experiments have been carried out in the MarinLab towing tank at Høgskulen på Vestlandet to investigate the velocity deficits and the turbulent kinetic energy development in small wind farm setups of five to seven turbines. The goal is to analyze how flow interaction effects between the individual wind turbines will affect both the upstream and downstream flow of the farm. Experiments have been performed on three different setups consisting of five to seven submerged porous disks with a diameter of 0.2 meters. An acoustic Doppler velocimeter is used to measure the velocities at different upstream and downstream locations. From the experiments performed, it is observed that a setup of aligned turbines i.e., low total blockage ratio experiences a more significant velocity deficit upstream, a higher level of turbulence in the wake, and a slower recovery for the wake compared to the other setups. In contrast to that, a setup with laterally offset turbines i.e., high blockage ratio, had a lower velocity deficit in front of the disks upstream, a lower maximum value of turbulent kinetic energy, and a faster regeneration of the flow rate compared to the other setups.

Moreover, it is observed for the offset farm setup that the inflow to the second row is accelerated causing an increased velocity deficit and higher turbulence levels. Correcting for accelerated inflow resulted in a very similar second-row wake flow compared to the first-row wake flow.

The upstream induction zone in front of the central first-row turbine was not observed to be significantly influenced by the investigated wind farm setups in this set of experiments. A rather small number of turbines at a sufficiently large spacing is assumed to be the main reason for not observing any significant wind farm blockage effects in this experiment.

Sammendrag

For å kunne optimalisere energieffektiviteten i en vindpark vil det være vesentlig å vurdere turbinenes plassering i forhold til hverandre. En av effektene som kan påvirke effektiviteten er blokkeringseffekten. Denne ble nylig diskutert for overestimering av effektivitet, da det stort sett ble brukt en vindskygge-tilnærming for å forutsi effektiviteten ved vindparker. Det er utført mange ulike studier på disse fenomenene for å undersøke hvordan blokkeringseffekten kan påvirke et stort antall turbiner.

I denne oppgaven er det utført laboratorieskalaeksperimenter i MarinLab ved Høgskulen på Vestlandet for å undersøke hastighetsunderskuddet og den turbulente kinetiske energiutviklingen i små vindparkoppsett bestående av fem til syv turbiner. Målet er å analysere hvordan strømningsinteraksjonseffekter mellom de enkelte vindturbinene vil påvirke både oppstrøms og nedstrøms i en vindpark. Det er utført eksperimenter på tre ulike oppsett bestående av fem til syv porøse disker med en diameter på 0.2 meter. En akustisk Doppler hastighetsmåler har blitt brukt til å måle hastighetsprofilene ved ulike avstander i vindparken. Fra eksperimentene som er utført, har det blitt observert at et oppsett av ordnete turbiner (lavt blokkeringsforhold), opplever det største hastighetsunderskuddet oppstrøms, de høyeste nivåene av turbulens i kjølvannet og den sakteste gjenopprettingen av kjølvannet. I motsetning til dette, hadde oppsettet med forskjøvede turbiner (høyt blokkeringsforhold), det laveste hastighetstapet foran diskene, det laveste maksimalnivået av turbulent kinetisk energi og den raskeste regenereringen av strømningshastigheten.

Videre ble det observert at diskene i andre rad opplevde en høyere innløpshastighet som førte til høyere hastighetsunderskudd og turbulensnivåer for oppsettene med forskyvning. Ved å korrigere denne, observerte man en tilnærmet lik kjølvannsstrømning for diskene i andre rad sammenlignet med dem i første rad.

Induksjonssonen oppstrøms foran den midtre turbinen i den første raden ble ikke observert å være tydelig påvirket av de undersøkte vindparkoppsettene i de gjennomførte eksperimentene. Et lite antall turbiner med tilstrekkelig stor avstand antas å være hovedårsaken til å ikke kunne observere noen vesentlige vindpark blokkeringseffekter i disse forsøkene.

Contents

1 Introduction

1.1 Background

As a result of man-made greenhouse gas emissions, the world is facing a major common problem in the form of global warming. Through the Paris Agreement, countries worldwide have committed to a shared ambition to avoid dangerous climate change by limiting global warming to well below two degrees Celcius above pre-industrial levels. By achieving the objectives of the Paris Agreement, each country is dependent on a large-scale restructuring of how energy is used and produced. As the world's population increases, the energy demand is expected to double over the coming decades. It will require a significant investment to meet the energy needs of nine billion people, as well as reducing greenhouse gas emissions, air pollution, toxicity, and impacts on land, water, and other ecosystems [1]. The most important act to slow down climate change is for the energy industry to find energy sources free of carbon dioxide pollution.

By reducing the emissions, fossil fuels need to be replaced by renewable energy sources such as wind, water, and solar and a reduction in energy consumption across the world. If this adjustment succeeds, emissions will decrease, and the consequences of climate change will be less significant. It is essential to produce renewable energy. In 2015 United Nations Environment Programme published a report that provided a comprehensive comparison of the greenhouse gas mitigation potential of various energy generation technologies. They concluded that wind power, together with solar power, is the technology that has the lowest toxicity scores [1].

In 2020 the market for renewables grew by three percent, while the demand for all other fuels declined [2]. According to Global Wind Energy Council [3], this was the best year in history for the global wind industry, with year-over-year growth of 53%. Installation of more than 93 GW of wind power in a challenging year where Covid-19 has caused disruptions in the global supply chain and project construction shows that the wind industry has remarkable resilience. As stated by the International Energy Agency [2], renewable energy sources will account for more than 50% of the increase in global power supply in 2021, where solar cells and wind expects to contribute to two-thirds of the growth in renewable energy. Wind energy is estimated to

grow by 275 TWh, which corresponds to 17% from the record year 2020. This year will be the most significant registered increase in renewable production. In other words, the development of wind energy is constantly growing.

In 2019, Ørsted announced that they had adopted new methods for estimating future energy production in their offshore wind farms to realize how much efficiency in a park decreases due to the presence of other wind turbines. This modification was related to the work of Bleeg et al. [4]. They performed field measurements and simulations, and they discovered that the blockage effect caused a more distinct wind speed reduction upstream of a wind farm than previously expected. Previously, when calculating the turbine interaction losses in a wind farm, the only effect considered was the wake effect. Therefore, turbine interaction models are also known as wake models. They are used to investigate how the flow behind a turbine may affect other turbines in a wind park and to estimate the future power yields. These models have usually not considered the blockage effect, and it is thus likely to be assumed that the turbine interaction losses in the wind industry have been underestimated. To optimize the energy output in wind farms, it will be necessary to get a better understanding of the science behind wind resources and energy estimation. Therefore, it is important to identify the presence of the blockage effect in wind farms.

1.2 The evolution of wind turbines

Wind energy is produced by turbines capturing kinetic energy from the wind and converting it into electricity. The wind is a renewable energy source, as the air is constantly set in motion by the temperature and pressure differences created by the solar radiation towards the globe. Therefore, wind turbines provide pure energy as it does not require environmentally dangerous fuel transports, produces no emissions, and leave no environmentally hazardous waste behind. Since the beginning of the 1980s, the size of wind turbines has doubled approximately every fourth year. The most massive turbines that were in operation after the year 2000 was 60-90 meter high and had a rotor diameter of about 80 meters with an energy output of 2 MW [5]. As of May 2020, Siemens Gamesa announced that they are working on developing the world's largest wind turbine, which will consist of a rotor diameter of 222 meters and with an

installed capacity of up to 15 MW [6]. Besides that, the turbines have grown in size, there have also been improvements in multiple details. Computerized control systems have become both cheaper and more advanced. New blade profiles get more energy from the wind, and modern power electronics make it possible to operate the turbines at variable speeds to optimize energy production. At the same time, as the wind turbines themselves have increased in size, the individual installations have grown. Earlier, they built one turbine at a time, then groups of three to four. Today large wind farms are built on land or at sea, where the largest installations in Europe consist of hundreds of wind turbines in the same area [5]. One of the largest wind farms in Norway is the Midtfjellet wind park, and it is shown in Figure 1. The wind park is located at Fitjar, outside of Bergen, and consists of 55 wind turbines that annually produce 433.7 GWh [7].

Figure 1: A part of Midtfjellet wind farm located at Fitjar. Photo captured by author

According to Global Wind Energy Council, global wind power growth needs to triple over the next decade to avoid the worst impact of climate change. That means that the world needs to be installing an average of 180 GW of new wind energy every year to limit global warming to well below 2 degrees above pre-industrial levels [3]. Even though 2020 was the best year in history for global wind industry experienced, the installation of new capacity was only 93 GW, this was a 53% increase from 2019, but this is not enough to stay on a net-zero pathway and

to achieve net-zero by 2050 [3].

1.3 Offshore wind energy market

The benefits of offshore wind are better and more stable wind resources, large accessible areas, and likely lower conflicts of interest than on land. In addition, average onshore wind turbines with a capacity of 3 MW produce enough electricity for 1,500 households. An offshore wind turbine with 3.6 MW can supply energy to over 3300 households per year [8]. Thus, offshore wind turbines are also more efficient than those installed on land.

The technology of offshore wind turbines has developed majorly in recent decades. The first offshore wind farm was installed in the early 1990s, and in recent years the technology has accelerated. In 2009, offshore wind farms accounted for only 1% of global wind installations. Ten years later it increased to over 10%. Today, a single isolated offshore wind turbine has more capacity than the world's first two offshore wind farms combined. It is not just the capacity factor on the turbines that are developing. There are also studies on floating foundations to facilitate wind farms in deeper seas, as nearly 80% of the world's potential in offshore wind is in water deeper than 60 meters. Here, the wind is stronger and more consistent, and it is estimated that the floating offshore wind market will grow significantly over the next decade.

Global Wind Energy Council has presented prospects for the offshore wind industry. As earlier mentioned, 2020 was a record year for wind energy development as a total of 93 GW was installed, of this 6.1 GW was offshore wind, and it was the second-best year for offshore wind, only beaten by 2019 when it was installed 6.2 GW [3]. The number of annual installations is expected to quadruple by 2025 and will lead to an increased market share for offshore wind energy from 6.5% to 21% by 2025 [3]. These estimates are shown in Figure 2, and it can be observed that a total supply of 70 GW offshore worldwide is estimated in the period from 2021 to 2025. The reasons for this positive growth in the offshore wind market are a decline in the Levelized Cost of Energy (LCOE), which is a measure of lifetime costs divided by energy production. According to BloombergNEF (BNEF), the average LCOE for global offshore wind will be reduced by 67.5%, from 84$/MWh in 2012 to an expected value of 58$/MWh in 2025,

due to the scope of larger projects that have a higher capacity factor [9]. In 2019 The Ocean Renewable Energy Action Coalition (OREAC) published a report which stated that 1.4 TW of offshore wind by 2050 is achievable. This industry will experience incredible growth in the next few years. Therefore, it will be important to investigate various aerodynamic effects that can affect and increase the capacity factors of wind farms [9].

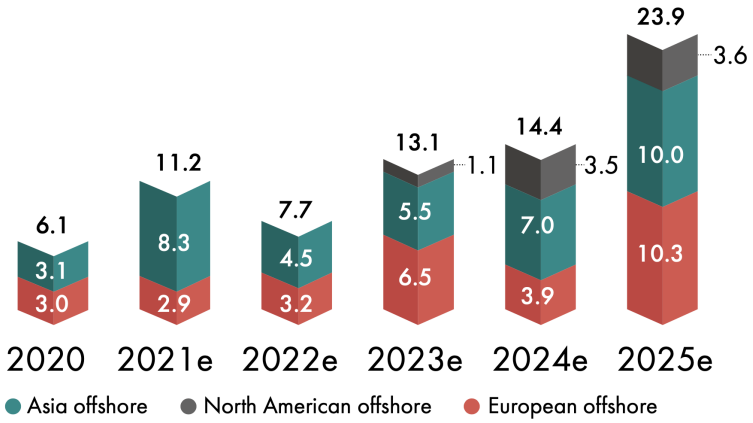

Figure 2: Market outlook 2021-2025 for new installations in offshore wind presented in GW [9]

1.4 Previously work

Numerous of analytical, computational, and experimental approaches have been used in recent years to investigate the flow effects in a wind farm. Medici et al. [10] compared experiments and simulations and observed that the velocity at x = -2D for a single isolated turbine decreased to $0.03aU_0$ where a is the induction factor, and U_0 is the free stream velocity. Garrett & Cummings [11] used a model to show that the limit of power extraction for a tidal turbine in a channel was dependent on the blockage ratio of the channel. Nishino & Willden [12] introduced the idea of scale separation where they defined a global blockage factor and a local factor for tidal turbines, they investigated how the maximum power coefficient depended on the two factors. Nishino & Draper [13] found that the limit of power extraction for a closely spaced lateral array of wind turbines increased when optimizing the local blockage.

Bleeg et al. [4] conducted field tests at three onshore wind farms and stated that the wind speed upstream for a wind farm decreases by 3.4% at two diameters upstream of a turbine.

Reynolds-Averaged Navier-Stokes simulations visualized that the slowdowns occurred due to wind-farm-scale blockage, leading to lower energy production of the front row turbines than a single isolated wind turbine. Hägglund [14] performed wind farm flow experiments using 250 scaled rotating turbine models in a wind tunnel. The tests showed a small effect on the upstream flow due to the turbines downstream, where the wind speed difference was under 1%. By increasing the density of the wind farm, the reduction in the wind speed at the center turbine could reach 2.5%, and it was also observed a smaller velocity deficit at the turbines on the edges of the wind farm. Segalini & Dahlberg [15] reproduced the experiments of Hägglund and performed numerical studies which indicated that the velocity decrease in the front row depends on the wind farm layout, where they proposed a simple functional dependency between the velocity decrease, number of rows and spacing. They observed that the magnitude of the blockage depended on the thrust forces on the flow imposed by the turbines, and a higher turbulence with a corresponding lower wake loss implied a higher relative blockage.

Ouro et al. [16] conducted numerical analyses to study how the turbines interact in arrays due to the velocity deficit and the turbulence levels in the wake. They carried out high-fidelity numerical simulations using a Large-Eddy Simulation-Actuator Line Method to investigate the impact of row spacing. They found that the lack of recovery has a negative effect on back-row turbines whose efficiency dramatically drops compared to those in the front row. Nishino & Ouro [17] investigated how turbines in a larger array depended on the balance of the negative effects from the wake interactions and the positive effect of the bypass flows due to the local blockage. They performed Large-Eddy Simulations on 28 different layouts. Where they experienced that the efficiency in an aligned array decreased when reducing the streamwise spacing, whereas for a laterally offset array, the efficiency increased due to the positive local blockage effect when the turbine spacing was sufficiently small.

Garnes et al. [18] performed scaled experiments in the towing tank at MarinLab at HVL to investigate the blockage and wake effects for a single rotor. They compared their results to experiments performed on the same actuator disk in a wind tunnel at NTNU, showing a valid similarity. Also, Bjørnsen [19] executed lab-scale measurements in MarinLab, researching how

the blockage and wake effects of an array consisting of three disks varied when changing the lateral distance between the disks. He observed significant blockage effects when y = 1D and 2D, where the center disk experienced a more significant velocity deficit than the edge. At y = 4D, the disks tend not to be influenced by each other and behave as single isolated turbines.

1.5 Aim of thesis

Numerous experiments have been performed investigating the wind farm flows in larger wind farms (hundreds of turbines [14] [15]) and local blockage effects on a small number of turbines and actuator disks (one [18] and three turbines [19]). It would be interesting to study how the wind farm blockage in a medium-sized array consisting of two rows would influence the wind farm flow effects. In this thesis, it will be performed experiments in MarinLab on five to seven actuator disks with a laterally offset or inline arrangements. This thesis aims to research the wind farm flows in three different setups, investigating the velocity deficit upstream and downstream and the development of the turbulent kinetic energy downstream.

2 Theory

This chapter will present relevant wind turbine aerodynamics theory to get an introduction to wind farm flows. Additionally, how to perform lab-scaled experiments will be presented, as well as results from other relevant studies.

2.1 One dimensional momentum theory for an Ideal Wind Turbine

A common simplification of a rotating, horizontal-axis wind turbine is to use actuator disks. This simple structure is easier and cheaper to manufacture and to use in experiments, as well as they are more robust than using rotating parts. The turbine is simplified by using a porous disk which allows the flow to pass through the rotor [20]. Actuator disks are designed to match a specific rotating wind turbine, where the diameter and the drag coefficient to the disk are similar to the rotor. The density of the disk is increasing towards the center. Developing a standard actuator disk design that can produce the desired wake would be efficient and practical to create uniformity and comparability between experiments.

The one-dimensional momentum theory [21] is a model based on the assumption of an ideal actuator disk to simplify the effects of a fluid passing through a rotor. The disk is considered ideal, which means that the flow is frictionless, stationary, and incompressible, and the flow outside the stream tube is not affected by other forces. As well as there is no rotational velocity component in the wake. In the absence of blades, there will not be any tip vortices present in the wake when performing experiments with actuator disks.

Wind turbine extracts mechanical energy from the wind's kinetic energy. When simplifying lab-scale experiments, the rotor is replaced with an actuator disk. The disk acts as a drag device that slows down the speed from u_0 far upstream of the rotor to u_r at the rotor plane and u_w in the wake. Due to this, the streamlines must diverge as shown in Figure 3. Where the drag force is obtained by a pressure drop over the rotor. Close upstream of the rotor there is a small pressure rise from the atmospheric pressure p_0 to p_r^+ before a discontinuous pressure drop Δp to p_r^- over the rotor. Downstream of the rotor, the pressure recovers continuously to the atmospheric level, p_0.

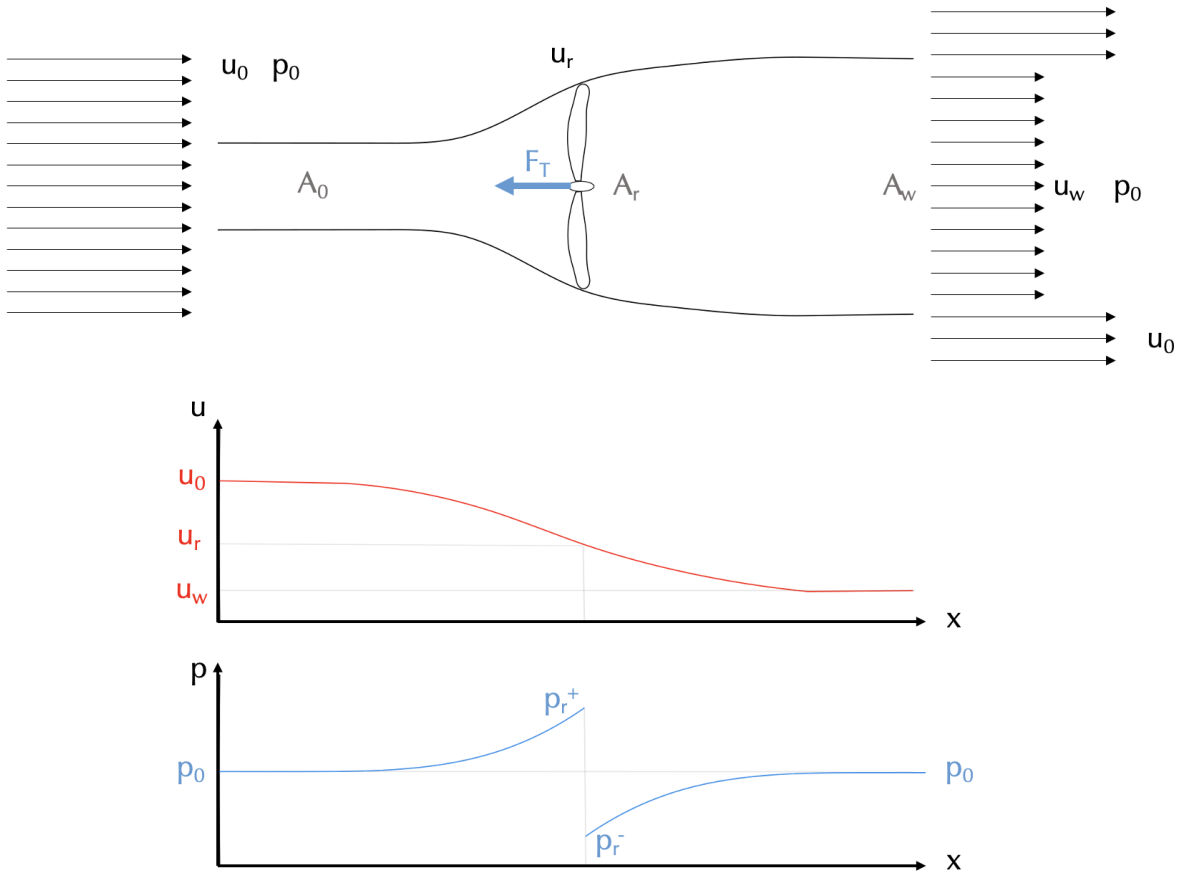

Figure 3: Illustration of the streamlines past the rotor and the axial velocity and pressure upstream and downstream of the rotor. Figure with inspiration from [21]

As mentioned the flow is considered ideal and there are no external forces that act on the fluid upstream or downstream of the rotor. Because of these assumptions the Bernoulli equation is valid from far upstream to just in front of the rotor and from just behind the rotor to far downstream in the wake

$$p_0 + \frac{1}{2}\rho u_0^2 = p_r^+ + \frac{1}{2}\rho u_r^2, \tag{1}$$

and

$$p_r^- + \frac{1}{2}\rho u_r^2 = p_0 + \frac{1}{2}\rho u_w^2 \tag{2}$$

By combining equation (1) and (2) yield

$$\Delta p = \frac{1}{2}\rho(u_0^2 - u_w^2) \tag{3}$$

Earlier, assumptions were presented that the flow passing through the turbine is stationary

and that the fluid is incompressible. For a stationary flow, it is possible to use the continuity equation to determine how much mass flow passes through the turbine. The continuity equation is an equation that expresses that a physical quantity is preserved, in other words, it neither disappears nor occurs during a reaction or process. This means that the mass flow rate, $\dot{m}$, will be equal for the different sections of the flow passing the turbine

$$\dot{m} = A_0 u_0 = A_r u_r = A_w u_w \tag{4}$$

As well as the mass is conserved, the momentum will also be conserved, the equation for momentum conservation is

$$\rho A_0 u_0^2 = \rho A_w u_w^2 + \Delta p A_r = \rho A_w u_w^2 + \frac{1}{2}\rho(u_0^2 - u_w^2) \tag{5}$$

To yield the velocity in the rotor plane is is possible to divide equation (5) by (4)

$$u_0 = u_w + \frac{\frac{1}{2}(u_0^2 - u_w^2)}{u_r} \rightarrow u_r = \frac{1}{2}(u_0 + u_w) \tag{6}$$

Where the velocity in the rotor plane is the mean of the speed and the velocity in the wake.

The axial induction factor, a, is the ratio of reduction of the far upstream velocity u_0 to the velocity at the rotor u_r. The axial induction factor is defined as

$$u_r = (1 - a)u_0 \tag{7}$$

By combining equation (6) with (7) yield

$$u_w = (1 - 2a)u_0 \tag{8}$$

While the induction factor increases from 0, the wind speed behind the rotor slows more and more. If $a = 0.5$, the wind speed has decreased to zero velocity behind the rotor, and the simple theory is no longer applicable. Therefore this theory is only valid for an induction factor less than 0.5 [22].

By using the assumptions of an ideal rotor, it is possible to derive simple relationships between the velocities, the thrust, and the absorbed shaft power. The thrust force, F_T is the force in the

streamwise direction resulting from the pressure drop over the rotor, and it is used to reduce the flow speed from u_0 to u_w.

$$F_T = \Delta p A_r = \frac{1}{2}\rho(u_0^2 - u_w^2)A_r = \frac{1}{2}\rho u_0^2 4a(1-a)A_r \tag{9}$$

Where A is the area of the rotor and is found by the following expression πR^2. The thrust force F_T is often non-dimensionalized with respect to F as a power coefficient C_T

$$C_T = \frac{F_T}{F} = \frac{\frac{1}{2}\rho A_r u_0^2 4a(1-a)}{\frac{1}{2}\rho A_r u_0^2} = 4a(1-a) \tag{10}$$

Likewise, it is possible to define a power coefficient that can express how efficiently a turbine converts the energy in the wind to electricity. The equation for absorbed shaft power, P is

$$P = F_T u_r = \frac{1}{2}\rho A_r u_0^3 C_T(1-a) \tag{11}$$

The available power in a cross-section that is equal to the swept area A_r by the rotor is

$$P_{available} = \frac{1}{2}\rho A_r u_0^3$$

The expression for the power coefficient, C_p, is derived by is by dividing the power P by the available power in the cross-section $P_{available}$

$$C_p = \frac{P}{P_{available}} = \frac{\frac{1}{2}\rho A_r u_0^3 C_T(1-a)}{\frac{1}{2}\rho A_r u_0^3} = C_T(1-a) = 4a(1-a)^2 \tag{12}$$

To calculate the theoretical maximum power coefficient of power for an ideal wind turbine it is necessary to differentiate C_p with respect to a which yields

$$\frac{dC_p}{da} = 4(1-a)(1-3a) \tag{13}$$

From this expression it can be seen that $C_{p,max}$ equals 16/27 for $a = 1/3$. This is also known as Betz limit which states that no wind turbine can convert more than 59.3% of the kinetic energy of the wind into mechanical energy turning a rotor [23].

Figure 4 shows the graphical representation of the equations for C_p and C_T. One can observe from the figure, that the maximum power output where a = 1/3, C_T has a value of 8/9. As

earlier mentioned this is an ideal model which is not valid for axial induction factors that are higher than 0.5 [22].

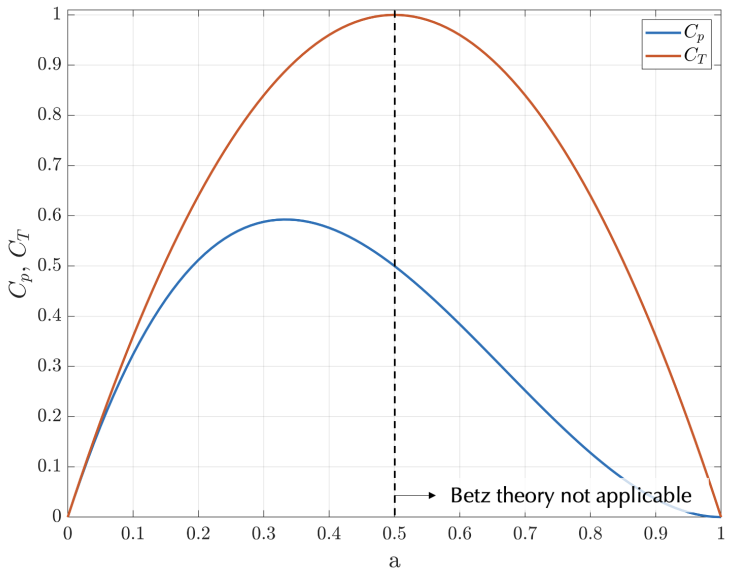

Figure 4: The power coefficient, C_p, and thrust coefficient, C_T as a function of the axial induction factor a

2.2 Actuator disk

Field tests of wind farms are expensive, difficult and unable to be controlled, in contradiction to experiments carried out in laboratories. Using small-scale models makes it possible to analyze wind farms in wind tunnels or water tanks. This enables a deeper understanding of physical phenomena that occur under different conditions, such as different wind speeds and turbulence intensity [20]. Modeling small-scale wind farms with rotating turbines for testing is very complex. Hence, simplifications are often made. Figure 5 shows the geometry of the disks used in the experiments in this thesis.

2.2.1 Comparison of a free rotating wind turbine and actuator disk

Since static actuator disks are easier and cheaper to manufacture, they are used in numerous experiments to simplify rotating turbines. Furthermore, it is still being established how convenient the simplification is and how the disk's geometry influences the results.

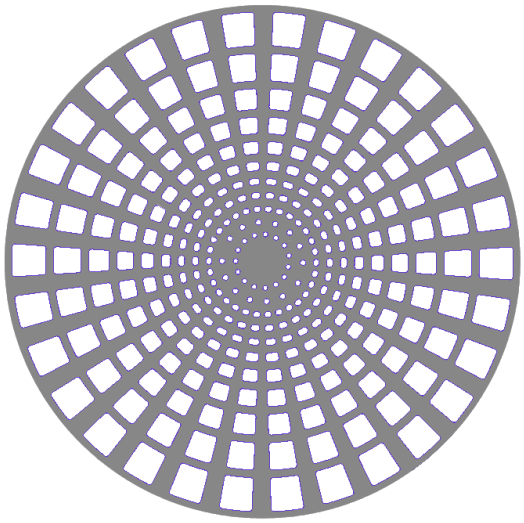

Figure 5: CAD drawing of the actuator disk used in this thesis

While actuator disks are designed to resemble a specific rotating wind turbine by having the same diameter and matching the drag coefficient, there are no standards for the design and production of the disks. Helvig et al. [20] have conducted experiments to investigate how comparable a well-matched actuator disk is to a rotating turbine. Using particle image velocimetry (PIV), they compared drag coefficient, mean velocity, and mean vorticity in the wake of the disks with a two-bladed rotating model. The experiments were performed on two different disk designs with three different solidities. The first design had uniform circular holes, and the second design consisted of trapezoidal holes, which increased in size with the radial coordinates. There were three different solidities; 35%, 40%, and 60%.

The study concluded that the trapezoidal disk with a solidity of 35% was the closest match for the rotor in terms of the drag coefficient and mean wake vorticity. The averaged drag coefficient of the two-bladed rotor and the actuator disk was 0.57 and 0.56. The disks used in this thesis are designed to imitate a three-bladed wind turbine. From Section 2.1 the maximum power output occurs while the drag coefficient is 0.89. Therefore, it is desirable to manufacture a wind turbine with that given drag coefficient. Hansen et al. [24] have performed experiments on the disks in this thesis to investigate the drag coefficient, which resulted in a C_d approximately 0.88. From analyzing CAD drawing of the porous disk, the solidity of the disk is 57%. Therefore, it will be interesting to compare the trapezoidal disk with 60% solidity from Helvig et al. with the porous disks in this thesis. The trapezoidal disk with 60% solidity experienced a drag

coefficient around 1.1, and in the wake area, the disk induces an area of reversed flow due to its more significant blockage. As well as it creates two distinct areas of high magnitude vorticity that cover large parts of the wake; this may be caused by vortices that are created at the disk edges or by the interaction between the wake and the free stream. In addition, vortices right behind the disks can be affected by turbulence flow through the holes in the disks [20]. Helvig et al. concluded that actuator disks are suitable for capturing mean flow properties, but instantaneous phenomena in the wake are not always adequately captured.

2.2.2 Comparison of actuator disk in wind tunnel and water tank

Garnes et al. [18] performed experiments on the same actuator disk used in this thesis. They aimed to research upstream blockage and downstream wake for one single disk, and compared their results with tests on the same disk in a wind tunnel at NTNU. The comparison in the two different test facilities is shown in Figure 6 where the measurements are performed at x = 3D.

From Figure 6 it can be observed the velocity deficit for the disk in MarinLab at HVL is higher than in the wind tunnel at NTNU. A reason for this can be that there will be no present turbulence in the water at HVL, but at the wind tunnel at NTNU, the wind will have inlet turbulence that will affect the wake. As mentioned earlier, additional turbulence in the flow will lead to a faster recovery in the wake. These results confirm that MarinLab is a test facility sufficiently competent for performing wake- and blockage effects measurements.

When investigating the flow around a wind turbine, it is usual to perform lab-scale measurements in a wind tunnel to research how the air flow affects the turbine. In this thesis the experiments will be conducted in a water tank. This is a justifiable method, due to water and air are both fluids with a different density and viscosity. As well as they are characterized as Newtonian fluids, meaning that the viscosity is constant, and the shear stress and shear rate have a linear relation. This allows both fluids to scale regarding Reynolds number, which is defined as the ratio between the initial and the viscous forces.

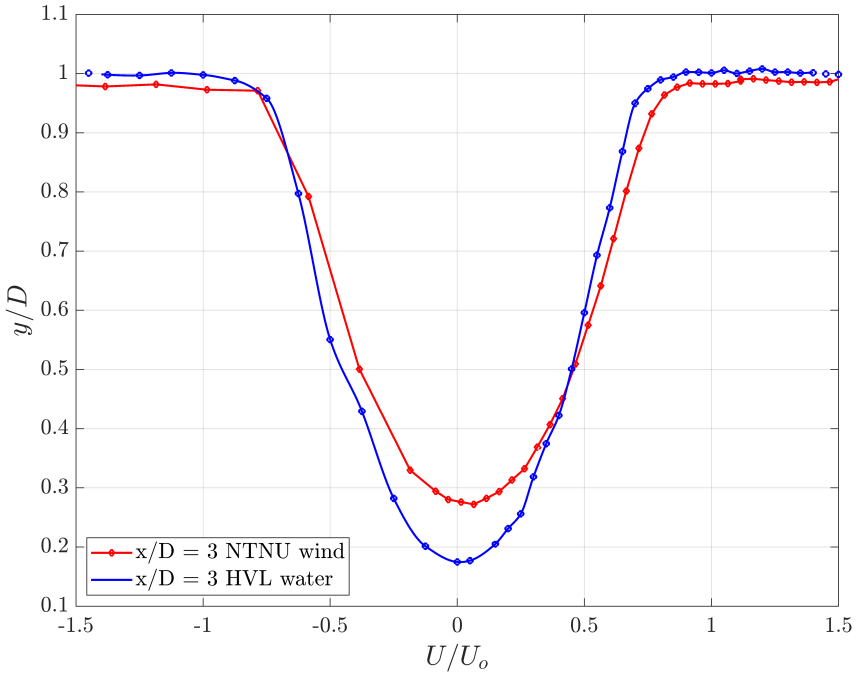

Figure 6: Comparison of the velocity deficit for one single actuator disk at x = 3D in the wind tunnel at NTNU and the water tank at HVL [18]

2.3 Wake

As a wind turbine generates electricity from the energy in the wind, the energy leaving the turbine is lower than the energy in front of the turbine. There will be a wake effect behind the turbine where the wind flow experiences an increase in turbulence, as well as a velocity deficit [25]. For an isolated wind turbine, the wake effect does not influence the energy output. But for turbines in a wind farm, the outcome is different. To minimize power losses in wind farms, it is important to study the wake effects behind turbines. Due to their interference effects that act upon turbines downstream, as shown in Figure 7. As well as high levels of turbulence intensity can impose fatigue loads on turbines placed downstream [26].

According to Göçmen et al. [28], the wake of a wind turbine is generally divided into the near-wake, within 2-4 rotor diameters behind the turbine, and the far-wake, which applies further downstream. In the near-wake region, the flow is influenced by the rotor geometry that leads to the formation of the blade tip and root vortices. In addition, the gradients of pressure and axial velocity are steep, and the wake is expanding. In the far-wake region, the geometry of the

Figure 7: Visualisation of downstream wakes at Horns Rev Offshore Wind Farm in Denmark [27]

rotor is less important, and turbulence is the dominating physical property here [28]. In the actuator disk theory, it is assumed that the free stream flow is separated from the flow in the wake. In reality, this is not the case. The velocity difference between the air inside and outside the wake will result in a shear layer. This shear layer will expand until it reaches the wake axis, as shown in Figure 8, which defines the end for the near-wake region [29].

Turbulent eddies are formed in the shear layer. The turbulence in the wake is an efficient mixer, that blends the low-velocity fluid in the wake with the high-velocity fluid outside it. This will transfer momentum into the wake, which will lead to an expansion in the wake and a reduction in the velocity deficit. Due to ambient shear flow, the turbulence in the shear layer is non-uniform, which leads to two peaks in the turbulence intensity in the near wake. Hence, in the far wake, the turbulence level is dominating, and the velocity deficit will decrease gradually, this will lead to a fully developed wake [29].

Turbulence is also caused by different sources as tip vortices, turbulent boundary layers over the blades, mechanical turbulence from the presence of nacelle and tower, and turbulence in the atmosphere. The tip vortices are formed due to the difference in the pressure between the lower and upper sides at the tip of the blade. They follow a helical path with rotation opposite to the rotor, as shown in Figure 9 below. The tip vortices are present in the shear layer and

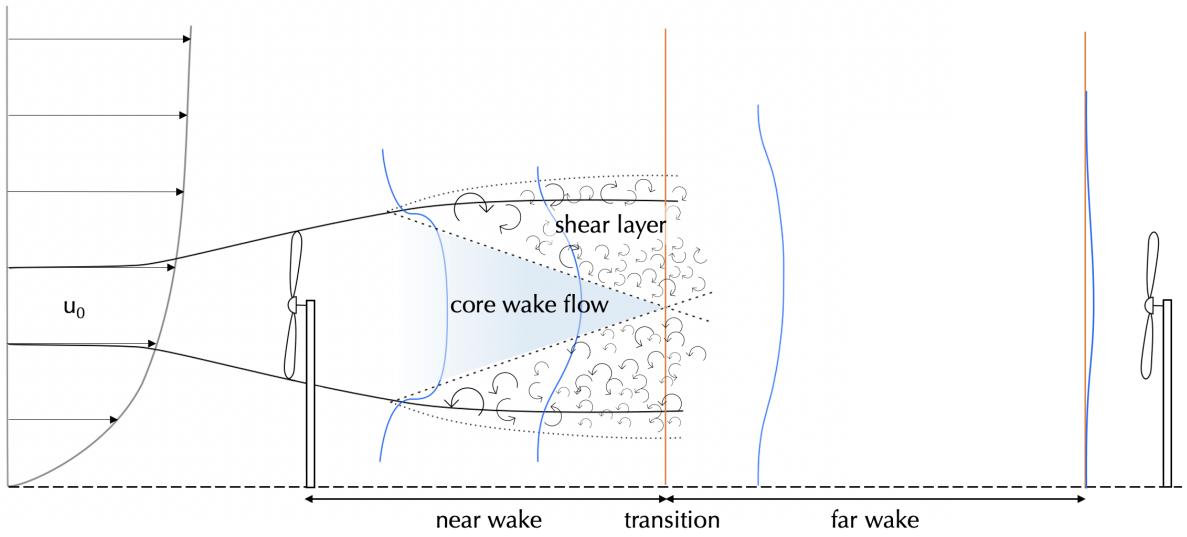

Figure 8: Illustration of the velocity profile in the wake behind a turbine with one turbine placed downstream. Figure inspired by [29]

will break down after approximately 4D [29].

Another assumption from the simplified one-dimensional momentum theory is that the airflow over an actuator disk only will experience a speed reduction and no rotation. In reality, the flow passing over the turbine blades will exert torque on the rotor. A reaction torque will act on the flow and causes it to rotate in the opposite direction. This means that a vortex formation will occur in the wake, which transmits unwanted rotational kinetic energy to the fluid flow, and will result in a reduction in the power coefficient of the turbine [29].

2.3.1 Turbulence in wind farm wakes

As earlier mentioned, it is important to study the wake formations in a wind farm to optimize the power output. In a wind farm, the turbines will be affected by the upwind wakes, and for a large wind farm, the power loss caused by the wake effect normally accounts for about 10% to 20% of the produced output for a year. A commonly used approach to simulate the interaction effect of different wakes is to combine analytical wake models with simple superposition assumptions [30]. By aligning multiple wind turbines with the wind direction, it has been observed that the turbines in the second row experience the maximum power loss, while the row further downstream experiences smaller losses. Figure 8 above, shows how the wake from an upstream

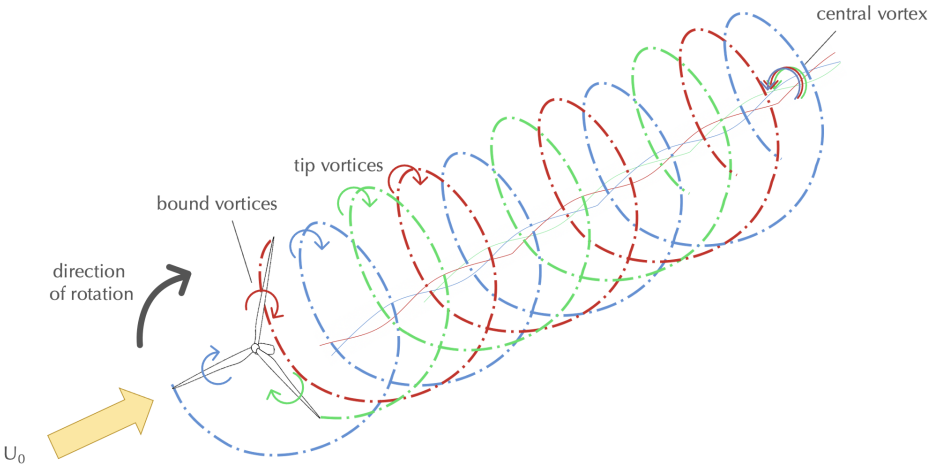

Figure 9: Illustration of a typical vortex system downstream of a three bladed rotating turbine. Figure inspired by [29]

turbine affects a turbine downstream. The upstream turbine will extract kinetic energy from the wind and will start to rotate. The rotating turbine will generate a wake that will increase the velocity deficit and the turbulence intensity. This flow will hit the downstream turbine and result in a reduction in the power output and an increase in fatigue loads due to high fluctuations in the wake flow.

In the far-wake region, turbulence plays a leading role in flow development. The turbulent conditions re-energize the low-momentum wake regions in wind farms [29]. The flow velocity inside the wake differs from around the wake, resulting in a shear layer that expands when moving downstream. Turbulent eddies in the shear layer transfers the momentum into the wake from the surrounding flow. Hence, the wake and the surrounding flow start to mix. The ambient turbulence level in the wake will impact the decay of the velocity deficit. A stronger ambient turbulence intensity will give a faster wake recovery.

There are two standard methods to measure the turbulence in the wake of a turbine. The first is to measure the turbulence intensity, TI and is defined by

$$TI = \frac{u'}{u_{mean}}, \tag{14}$$

where u' is the standard deviation from the average of the wind velocity, and u_{mean} is the

magnitude of the average wind velocity. TI is often presented in percentages [%].

In principle, the intensity differs from each wind direction. Therefore this approach is used when measuring one dimension [29]. When measuring velocity for multiple directions, it is usual to use turbulent kinetic energy, TKE, to measure the turbulence in the flow. Turbulent kinetic energy is the part of the kinetic energy per mass that is associated with eddies in a turbulent flow. In general, TKE is defined to be half of the sum of the variances of the velocity components. This is because the turbulent part for the wind is the standard deviation from the average, which is the square root of the variance. The formula for TKE is

$$TKE = \frac{1}{2}\left((u')^2 + (v')^2 + (w')^2\right), \tag{15}$$

where u', v' and w' are the standard deviations from the mean velocity. The unit for TKE is m^2s^{-2}. This is the measure for turbulence that will be used in this thesis.

2.4 Blockage effect

Energy extraction from a wind turbine induces a reduction of the wind speed upstream; this effect is defined as the upstream blockage effect. Developers have recently taken an interest in researching this effect. This effect has previously been neglected when predicting the energy production in wind farms. Which may have resulted in an over-prediction of energy production and biases in the power curve measurements [31]. The upstream blockage effect of a single isolated wind turbine is already accounted for in Section 2.1 as the axial induction factor. In a study performed by Medici et al. [10], they observed that the induced velocity at x = -2D was $0.03aU_0$. Therefore it is assumed to measure free-stream velocity between 2D and 4D upstream for a single isolated wind turbine. Because the distance between wind turbines in a wind farm is more extensive than 3D, the downstream turbines should not influence the ones upstream. Many wind farm estimations are performed with wake-only approaches, where the upstream effect is negligible.

Dahlberg & Hägglund [14] performed experiments that indicated that the assumption on the first row is unaffected by the rest of the wind farm is wrong. They conducted experiments with

almost 250 turbines, changing the distance between the first row and the rest of the farm. The results from the test showed that the turbines experienced a more significant decrease in velocity when reducing the distance between the first row and the wind farm. They also observed that the turbines on the edges experienced a lower speed reduction than the turbine in the center. The blockage effect was also recognized by Ørsted when they 2019 announced that they had overestimated the production at offshore wind installations, based on the research of Bleeg et al. [4]. They compared observations at three wind farms with RANS simulations and concluded that turbines in a farm would underproduce. Hence, the numerical simulation indicated that the wakes-only approach could neglect a substantial fraction of the total turbine interaction loss. Models based on wakes-only will, in general, overpredict the production of wind farms.

2.4.1 Blockage effect for a turbine in a channel

Tidal turbines will also experience a blocking effect that affects the energy production of the turbine. The difference between wind turbines and tidal turbines is that the tidal turbines are placed in a channel, with a limited area between the seabed and the sea surface, as shown in Figure 10. It leads to a more significant blockage for the free-flow velocity that hits the turbine than for wind turbines that have an almost infinite free-flow area around the turbines. This will lead to an accelerating bypass flow, U_b, which will lead to a higher pressure difference at the disk, which will make the power output of the turbine larger. It can be shown using the mass continuity and momentum conservation described in Section 2.1, whereas for this case the bypass flow is added in this derivation [11].

Figure 10 is similar to Figure 3, the only difference is that the turbine with swept area A_d is located in a channel with a cross-section area of A_c and that there is a bypass flow outside the wake, U_b.

As shown in Figure 4 the maximum power output occurs when a is 1/3, and by using Equation (2.1) the velocity in the wake

$$U_w = \frac{1}{3}U_0 \tag{16}$$

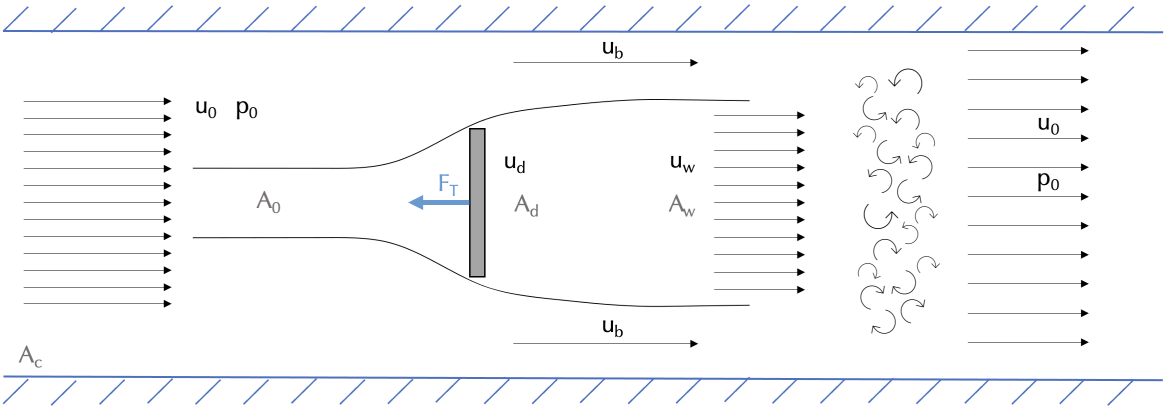

Figure 10: Illustration of a single tidal turbine in a channel. Inspiration from [11]

To express the magnitude of the bypass flow, U_b, and the velocity at the disk, U_d, the following equations are used

$$U_b = U_0 \frac{3+\epsilon}{3(1-\epsilon)} \quad , \quad U_d = U_0 \frac{2}{3(1+\epsilon)}. \tag{17}$$

Here ϵ is the blockage ratio A_d/A_c.

From the one-dimensional momentum theory in Section 2.1 it was stated that due to the Betz limit, it was not possible for a wind turbine to convert more than 59.3% of the kinetic energy in the wind into mechanical energy rotating a rotor. However, a turbine in a tidal channel can exceed Betz limit with the following equation

$$P_{max} = \frac{16}{27}(1-\epsilon)^{-2}\frac{1}{2}A\rho {U_0}^3 \tag{18}$$

The additional efficiency $(1-\epsilon)^{-2}$ compared with the maximum power for an isolated turbine occurs due to the restraining influence of the channel boundaries, increasing the pressure drop across the turbine [11].

2.4.2 Scales of blockage

The model of Garett & Cummings suggests that the efficiency increases as the channel blockage increases by adding more turbines across the cross-section as the efficiency depends on $(1-\epsilon)^2$. Nishino & Willden [12] wanted to extend the model based on Garrett & Cummings to explore

the efficiency of a long array of tidal turbines that partially blocks a broad channel cross-section. They saw the need to define the blockage effects in different scales; local, array, and global blockages. The local blockage is the ratio of the local channel area relative to one turbine. Array blockage concerns the flow through an array of tidal turbines, and the global blockage concerns the whole channel area covered by n turbines. Nishino & Willden assumed that the flow behind each turbine mixes faster than the horizontal expansion of the flow around the whole array. That made it possible to model the flow in different scales as the conservation of mass, momentum, and energy was considered. The new model stated that when turbines block a small part of the span in a shallow channel, there will be an optimal distance between the turbines to maximize efficiency. The efficiency will increase while the spacing reduces to the optimal value due to the local blockage effect, but will decrease as the reduction in spacing between the turbines will block a large scale of the channel, and the flow will choke. With an increase in local blockage, the efficiency will increase from the Betz limit of 0.593 to another limiting value of 0.798 but then decrease as the local blockage will further increase.

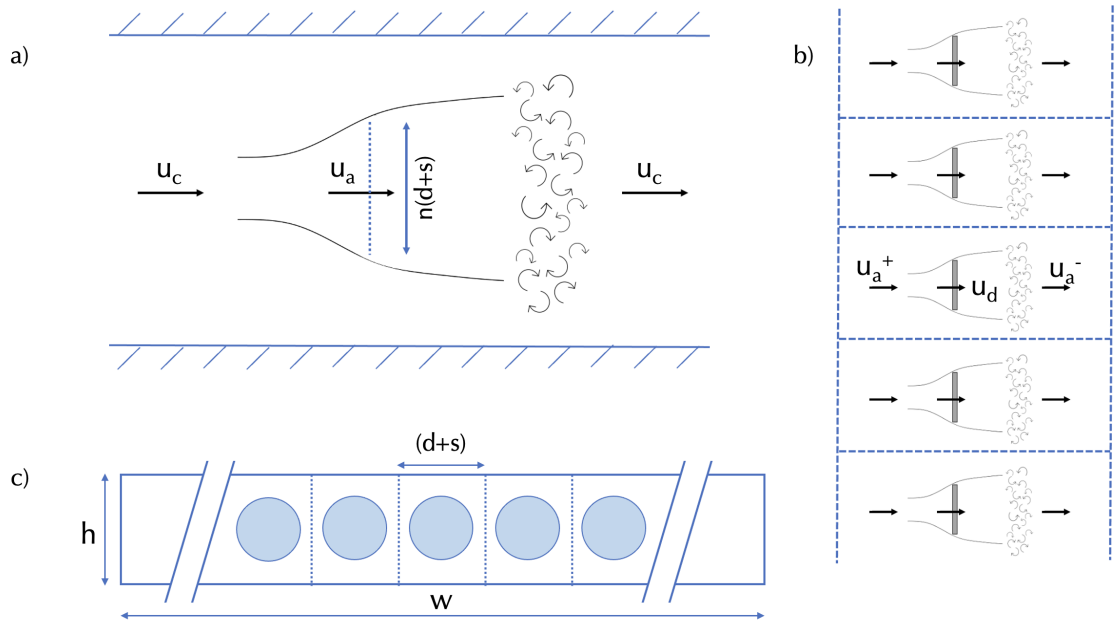

Figure 11: Schematic of tidal turbines partially blocking a channel cross-section. a) Array-scale flow expansion and mixing. b) Local-scale flow expansion and mixing. c) Cross-sectional view of the channel. Drawing inspired by [12]

Nishino & Draper presented a paper researching the power extraction for a closely-spaced lateral array of wind turbines, investigating if the power coefficient for each turbine would

increase significantly if when optimizing the lateral spacing. They observed a similar but less significant power increase due to the effect of the local blockage [13].

2.5 Spacing

As earlier mentioned the general task of a wind turbine rotor is to extract as much kinetic energy from the moving airstream as possible. This results in lower wind speeds behind a wind turbine, which affects the performance of downwind turbines. A wind farm will not be able to produce the same amount of energy as several isolated turbines would in the same prevailing wind. This loss of energy is called array loss. To minimize the array losses, it is important to optimize the geometry of the wind farm. Having a larger distance between each turbine the array losses will decrease. However, it will restrict the number of turbines in the located area, as well as the costs of cabling, will increase [32]. The spacing is therefore an optimization problem between compactness of the wind farm, and the adequate separations between turbines, to minimize the array loss due to wind shadowing from upstream turbines. Figure 12 shows a regular array of turbines in a wind park concerning the prevailing wind direction. There are two directions to be acknowledged; downwind and crosswind.

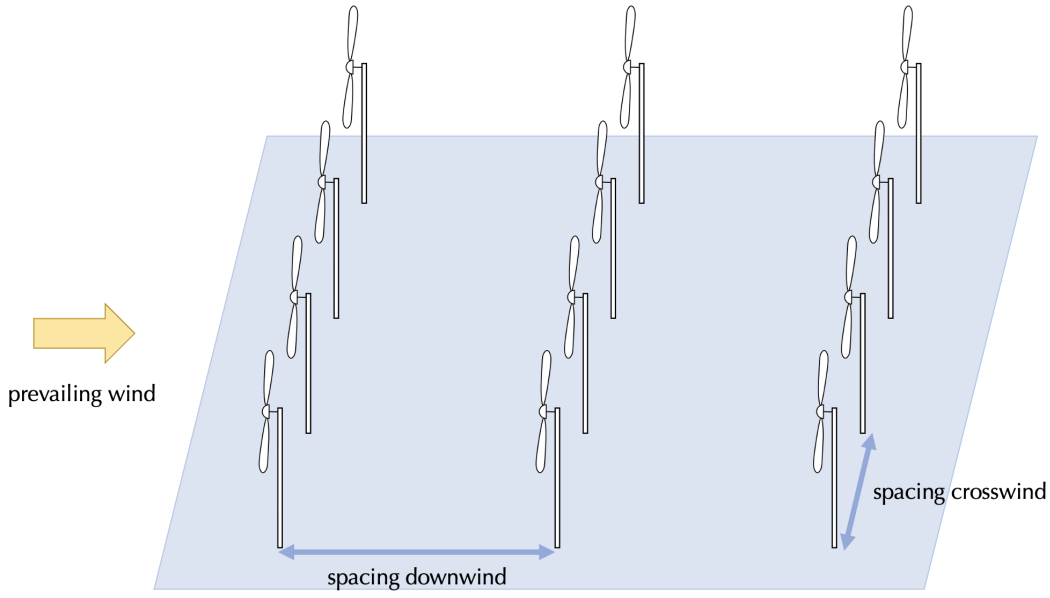

Figure 12: Arrangement of wind turbines in a wind farm placed downwind and crosswind

In general, the spacing between turbines should be 3-10 times the rotor diameter, and it depends on the prevailing wind direction. In the crosswind direction, the distance between turbines

should be larger than 3-4 rotor diameter [33]. To limit the total array losses to below 10% it is recommended that in the downwind direction the spacing should be 8-10 diameters [32].

2.6 Numerical analyses on tidal turbine farms

Another method to extend the knowledge about how turbines interact in arrays is by using high-fidelity numerical simulations as the Large Eddy simulation-actuator line method. Ouro et al. [16] performed this type of analysis comparing how a spacing of four and eight diameters between the rows and 1.5 diameters between the turbines. The results from the case where the streamwise distance is four diameters between the rows will be presented because this is the same distance in this thesis. Figure 13 shows the a contoured velocity plot and the velocity profiles at x = 6D, 8D, 10D and 12D. It is observable that the turbines in the second row are influenced by the low-velocity wake generated behind the front row. When comparing the LES with experiments performed by Olczak et al. [34], the individual wakes at x = 6D are clearer from LES. Further downstream at x = 8D, the results agree better with each other. At x = 10D and 12D, the wake has not recovered fully, and the single merged wake is visible.

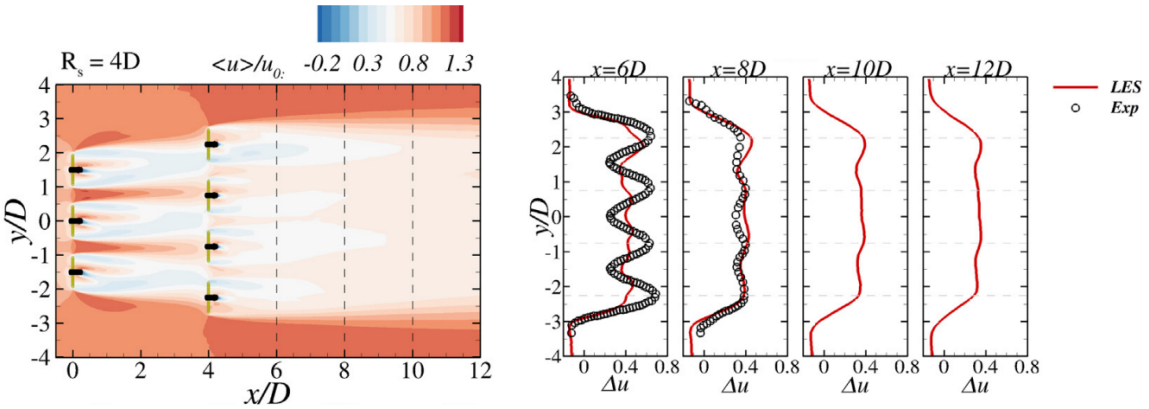

Figure 13: Contours of mean streamwise velocity for a two row array with an inter-row separation of 4D and profiles of velocity deficit for the cases comparing LES results [16] and experimental data [34]

Figure 14 shows the turbulence intensity and kinetic energy for the array. The second row operates in a highly turbulent wake of the upstream turbines. The outer turbines partially operate in the highly turbulent wake and are also influenced by the ambient free-stream flow, leading to significant turbulence on the edges further downstream. Regarding the turbines in the middle, their wake develops with high turbulence levels and decays rapidly, as they are

surrounded by the shear layers formed from the edge turbines that indicate high turbulence levels. It can be observed in both contour plots. The turbulence levels at x = 10D and 12D, where the wakes tend to merge, are decayed to the similar values of free-stream conditions.

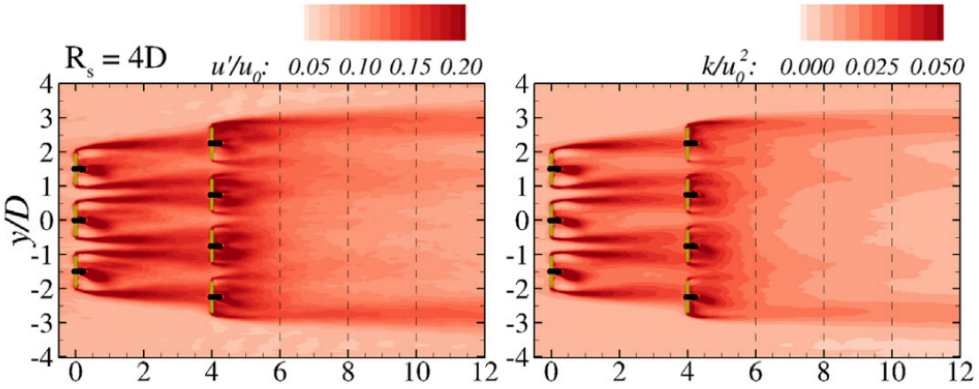

Figure 14: Contour of streamwise turbulence intensity (left) and turbulent kinetic energy (right) for to arrays of turbines with an inter-row separation of 4D [16]

Ouro & Nishino [17] have also performed Large-Eddy simulations. They investigated the balance between the adverse effects from turbine-wake interactions with the positive impact of the bypass-flow acceleration due to local blockage in an infinitely large array. They were investigating aligned and laterally offset layouts with different spacing downwind and crosswind. Figure 15 depicts the contoured mean velocity with a downwind spacing of 9 diameters and crosswind of 4 diameters for a laterally offset and an aligned arrangement. The wakes are primarily recovered in the laterally offset arrays when reaching the following row further downstream. Due to lateral blockage, the recovered wake accelerates further and affects the turbines in the next row. For the laterally offset arrangements, the lateral wake expansion is limited compared to an aligned layout. The flow that passes the lateral gaps between the turbines creates high-speed streaks for the aligned cases, resulting in a more significant velocity difference between the wake and the bypass flow.

When investigating the turbulence in the different cases, it is visible from Figure 16 that turbines in an aligned layout lead to a notably stronger flow unsteadiness inside and outside the wake than in the laterally offset cases. In the near-wake, the downwind and crosswind turbulence intensities are significantly more extensive in the aligned cases than for the laterally offset ones. The low turbulence intensity regions in the laterally offset cases are apparent in the bypass

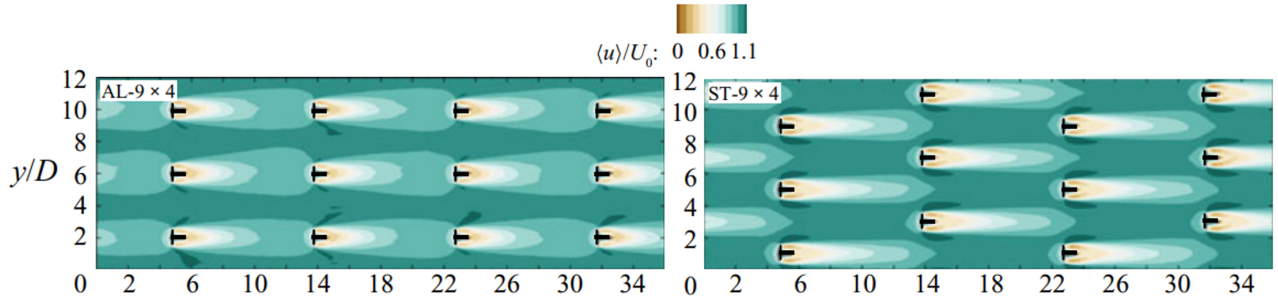

Figure 15: Contour of mean streamwise velocity for aligned (left) and laterally offset (right) cases with row separation of 9D and a lateral spacing of 4D[17]

flows simultaneously as the region where the wake of an upstream turbine is fully recovered. It shows that a larger blockage ratio in a channel will reduce the turbulence intensity regardless of the turbine arrangement. Due to constraining the formation of high-momentum, quicker wake recovery occurs in lower blockage cases resulting from more extensive entrainment of ambient flow into the wake. Although a lower blockage ratio results in a higher wake recovery in the near wake, it does not always hold in the far wake. Contrary to the wakes with a higher blockage, they will have a slower recovery rate in the immediate region but higher in the far wake. When comparing the aligned and laterally offset cases for a given streamwise spacing, the velocity recovery rate in the near wake is higher in the aligned cases due to more significant turbulent mixing enhanced.

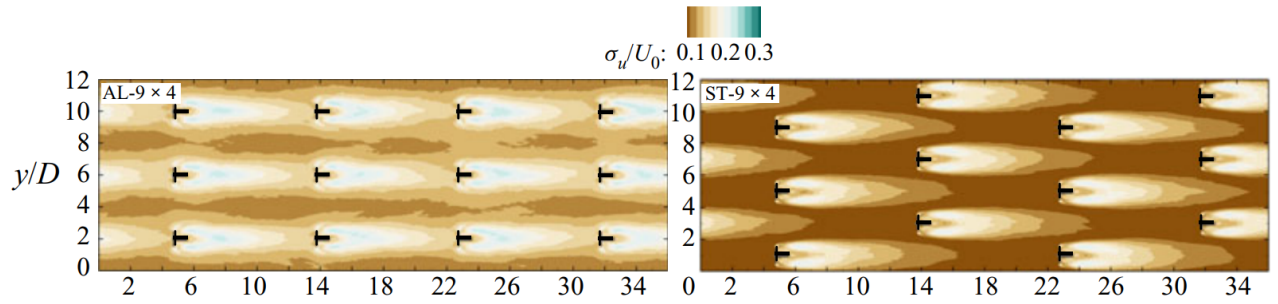

Figure 16: Contour of streamwise turbulence intensity for aligned (left) and laterally offset (right) cases with a downwind separation of 9D and a crosswind spacing of 4D [17]

2.7 Scaling

For model experiments to be a complete representation of the full-scale reality, three types of similarity are required in principle:

1. Geometric similarity
2. Kinematic similarity
3. Dynamic similarity

To meet the first requirement for geometric similarity, a full-scale turbine will be scaled down by the factor λ, so that the dimensions and shape of the model correspond to the original turbine. This means that all the dimensions of the model must have the same mutual size ratio as in full scale [35]. To achieve kinematic similarity, the flow around the model in the towing tank must correspond to the flow around the turbine in full scale. As well as a similarity in speed ratios. Because of this, the velocity vectors needs to have the same direction in the model and full-scale, which means that the streamlines are geometrically similar [35]. Dynamic similarity requires that the ratio between the different forces is equal, regardless of the size of the body. Some of the most important forces that act in an experiment performed in a towing tank are the inertial forces, viscous forces and gravity forces [35]. The ratio between inertial forces and viscous forces is called Reynolds number and is defined by the following expression:

$$Re = \frac{F_i}{F_v} = \frac{\rho U^2 L^2}{\mu U L} = \frac{\rho U L}{\mu} = \frac{U L}{\nu} \tag{19}$$

Here U is the flow rate, L the length of the object and ν is the kinematic viscosity. The viscosity represents the internal friction of the liquid, it is obtained by dividing the dynamic viscosity by the density of the fluid. The similarity in Reynolds' number will ensure that viscous forces are correctly scaled. And the following equation needs to be fulfilled:

$$Re = \frac{U_m L_m}{\nu_m} = \frac{U_s L_s}{\nu_s}. \tag{20}$$

Another force ratio that must be equal to achieve dynamic similarity is the relationship between the forces of inertia and the gravitational forces on the model and a turbine [35]. This is given by the following equation:

$$\frac{F_i}{F_g} = \frac{\rho U^2 L^2}{\rho g L^3} = \frac{U^2}{gL} \tag{21}$$

The square root of this expression is Froude's number. If a model has the same geometry and Froude number as the original object, they will have the same coefficient of wave resistance and they will have the same appearance of the wave system behind them. Thus, Froudes numbers must be equal to meet the requirement of dynamic similarity, and the following equation must be satisfied

$$Fr = \frac{U_m}{\sqrt{gL_m}} = \frac{U_s}{\sqrt{gL_s}}. \tag{22}$$

To achieve dynamic similarity both (20) and (22) must be fulfilled, the problem is that these two cannot be fulfilled at the same time. This makes it physically impossible to perform a model test with an equal ratio of inertia, gravity, and viscous forces [35]. Since this case will observe how a fluid affects a turbine, one cannot scale based on Froude's number, because free surface effects and waves are absent. A wind turbine in a wind farm out at sea will experience wind currents and be surrounded by air, the porous disks in this experiment will be submerged in water and experience a flow that acts on them. Both air and water are viscous liquids. Therefore it will be necessary to scale with respect to Reynolds' number.

Table 1: Reynolds number for a full scale turbine and model scale in air and water

	D [m]	u [m/s]	ρ [kg/m^3]	μ [Ns/m^2]	Re
Full scale	200	10	1.246	$1.778 \cdot 10^{-5}$	$1.402 \cdot 10^{8}$
Model scale in air	0.2	0.5	1.204	$1.825 \cdot 10^{-5}$	$6.597 \cdot 10^{3}$
Model scale in water	0.2	0.5	998.91	$1.1076 \cdot 10^{-3}$	$9.019 \cdot 10^{4}$

In Table 1, specifications for a 11 MW wind turbine in full scale, model scale in air and water are presented.

As earlier mentioned to ensure correctly scaled viscous forces, the Reynolds number for the model scale and full scale needs to be similar, according to (20). To fulfill the equation the

velocity for the model in the water tank yields

$$U_{ms} = \frac{Re_{fs} \cdot \mu_{ms}}{D_{ms} \cdot \rho_{ms}} = \frac{1.402 \cdot 10^8 \cdot 9.019 \cdot 10^{-4} Ns/m^2}{0.2m \cdot 998.91 kg/m^3} = 632.9 m/s \tag{23}$$

To achieve a similar Reynolds number for the model scale as the full scale turbine, the velocity needs to be 633 m/s. This is not possible to perform in MarinLab, and it is showing that there will be a discrepancy in the Reynolds number between full scale turbines and experiments performed in towing tanks or wind tunnels.

When researching the aerodynamic effects that act on turbines and porous disks the experiments are usually performed in a wind tunnel. Although it is most common to test turbines in wind tunnels, there are many experiments on scaled turbines in water basins. Okulov et al. [36] performed tests in a tank to understand and describe the resulting wake features for two rotors subjected to different operating and spatial conditions. In this thesis the experiments will be performed in MarinLab, where the fluid that acts on the disks is water. This can be justified by the fact that both water and air are fluids with different densities and viscosities, and it is considered when looking at the Reynolds number for the model. As shown in the table above, the carriage will be run at a towing velocity of $U_0 = 0.5$ m/s, which corresponds to a Reynolds number of $9.02 \cdot 10^4$. Although Reynolds' number does not match a full-scale wind turbine, this will be a simplification of a wind farm that will lead to seeing the physical interactions and effects that work on the various disks. The advantage of performing the tests in MarinLab is that the velocity of the carriage will be easy to control and that there will be no turbulence in the still water before the tests are conducted, contrary to the air in wind tunnels. In addition, the wind tunnels do not have very long test sections, this gives another advantage when testing in MarinLab to measure the far wake.

One of the challenges by performing experiments in a towing tank, is that the drag energy from the actuator disk can transfer waves in the free water surface. This is an effect that can

be observed visually by a dip in the free water surface and a formation of waves just behind the disks. By measuring the velocity in the z-direction, it is possible to observe the influence of the water surface. This dip in the water is caused by changes in the pressure in the region around the actuator disk [37]. To ensure that there are no free surface effects present when measuring the velocity components, it is important to investigate which depth the z-component is no longer influenced by the water surface. Experiments performed by Bjørnsen determined that a depth of 30 cm below the water surface was sufficient to minimize the free water surface effects, and that a velocity of 0.5 m/s was acceptable when running the tests [19].

3 Experimental method

The purpose of this chapter is to provide an overview of the experimental setup for the conducted tests and an introduction to the measurement instrument used in the experiments. In addition the measurement campaign will be presented and how the post processing of the results are being executed.

3.1 Experimental setup

All the experiments in this thesis will be performed in MarinLab at HVL. MarinLab is a hydrodynamic research facility consisting of a tank with dimensions 50m $\times$ 3m $\times$ 2.2m filled with water with a temperature of approximately 16°C. The tank is equipped with a fully automated wave generator from Edinburgh Designs that can create waves with a maximum wave height of 0.5 m and a wave period of 2 seconds. In addition, MarinLab is equipped with two carriages where various devices can be installed. The carriages are mounted on a rail and driven by a wire connected to a motor, which can achieve a maximum speed of 5 m/s and acceleration of 1.2 m/s^2 [38]. Figure 17 shows how the setup for the experiments is mounted on the carriages in MarinLab.

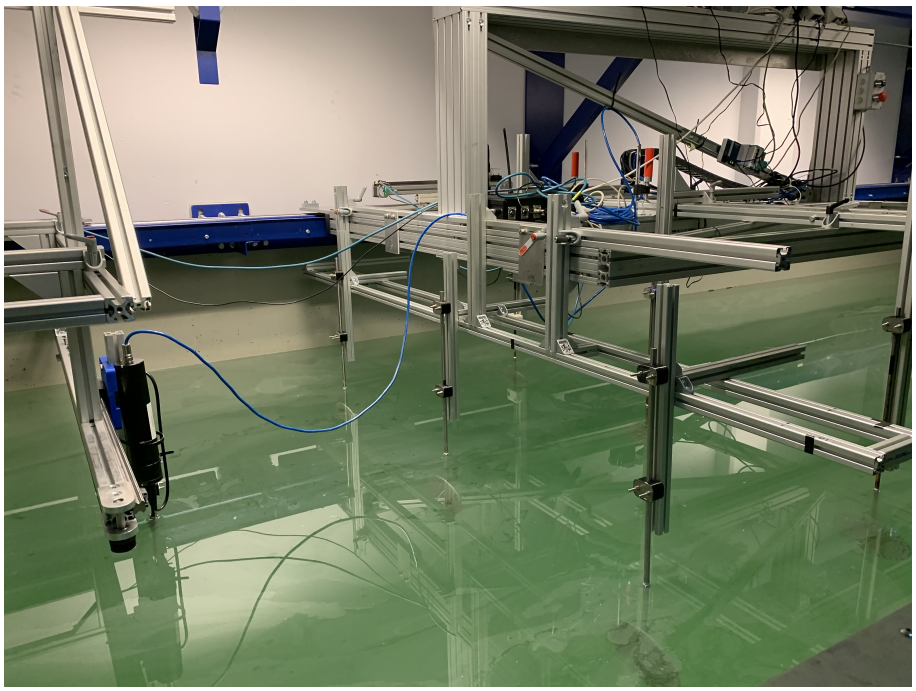

Figure 17: Picture of the actual setup in MarinLab of upstream and downstream measurements for WF6

The water in MarinLab is still, therefore the carriages will operate the disks and measurement device through the water with a given speed. This will, in principle, be similar to experiments performed in a wind tunnel, where the air is in motion while the disks are fixed, it will just be opposite. Figure 18 below shows a simplified sketch of the design for measuring the variation in the speeds in front of and behind the disks.

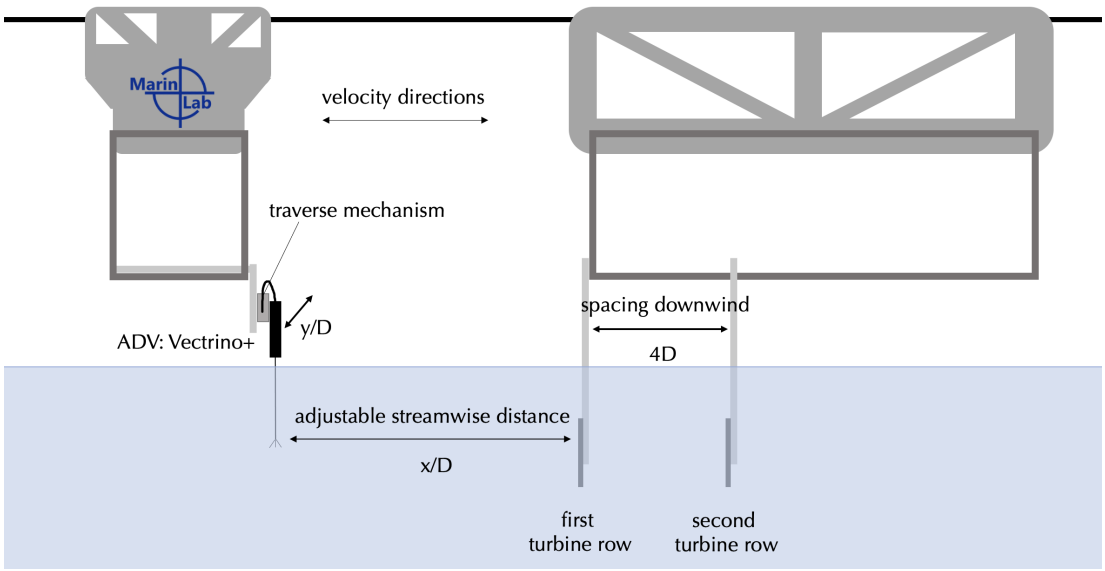

Figure 18: Schematic of the experimental setup on the towing carriages for upstream measurements

An automated traverse produced by the laboratory engineers at MarinLab will be used to move the measurement instrument. The traverse has a length of 1980 mm, and it can change position with a controlled stepper motor with millimeter precision. It is operated by a virtual instrument (VI) in LabVIEW, where it is possible to perform a calibration on the traverse. This will be achieved in preparation for measuring a new velocity profile to prevent a displacement in the y-coordinates for the measurement results. The measuring instrument mounted on the traverse is Vectrino+, an ADV manufactured by Nortek, and is shown in Figure 19.

3.1.1 Acoustic Doppler Velocimeter

The acoustic Doppler velocimeter measures the velocity of water by exploiting a physical principle called the Doppler Effect. This is the change in frequency of a sound wave when a wave source moves with respect to an observer, or vice versa. To measure the Doppler

Figure 19: Vectrino+ ADV from Nortek [39]

effect, the velocimeters measure velocity by transmitting a pair of short sound pulses with a specific frequency into the water column. Some of the sound waves reflect the instrument, the detected return signal will be further processed by the instrument. The reflected signal will be shifted, due to the Doppler Effect, in accordance with the water velocity. The frequency shift is expressed by following equation

$$F_{Doppler} = -F_{source}\frac{V}{c}, \tag{24}$$

where $F_{Doppler}$ is the change in the received frequency, F_{source} is the frequency of the transmitted sound, V is the velocity of the origin corresponding to the receiver and c is the speed of sound.

The sound pulses do not reflect from the water itself, but from passive tracers suspended in the water. The experiments that will be performed in this report will use seeding power, as the passive tracers. This is the moving particles that will generate a change in pitch or frequency in the return signal that the instrument measure. To ensure that the quality of the data and allow a proper calculation of the velocities, the received echo needs to be over a specific level. A measure of the magnitude of the acoustic reflection from the water is signal strength. This is a function of the type and number of particles in the water. With a weak echo, the calculation will be noisy, and the velocity data will show significant short-term variability. Signal strength is outputted by the instrument and there are two ways to access signal strength either as a raw

signal amplitude or "Signal-to-Noise ratio", SNR. SNR is a measure of the level of the signal concerning the background noise level. When collecting raw data it is recommended an SNR that is above 15 dB, and at least 5 dB if collecting mean data [39].

Another measure that is important to be aware of is the correlation. This is a measure of the similarity of the two pulse echoes that are being measured. If the correlation is zero, it means that there is no similarity between the two echoes. Correlation of 1 means that the two echoes are identical. For Nortek instruments, the correlation value will lay in the interval of 0-100%. The aim is a high correlation because it gives confidence that the system measured two pulses that originally were sent out and is determining a valid phase shift. To reduce the variance of a data set, it is normal to discard measurements with correlations lower than a threshold. This is a good idea because correlation is a strong indicator of data quality in the sense of a valid Doppler phase shift determination. In the early days of the acoustic Doppler velocimeter, the users determined that correlations above 70% were considered to be generating good quality data [39]. Today many users still use this number to screen out bad data, although a generalization to some universal value is unwarranted and a close examination of the data set will be the best way to set a correlation threshold for discarding bad data points.

3.2 Measurement campaign

The experiments will be performed on porous disks with a diameter of 0.20 m. Between the disks and the rows, the distance will be 4D. The number of disks will differ for the three different setups. The name for each setup is WFN, where the N represents the amount of disk in the wind farm. The front row for each setup will consist of three disks. WF5 will consist of five disks in total, where the second row will have two disks, that will have a laterally offset arrangement. For WF7, the arrangement will be the same, but there will be added two more disks in the second row. WF6 will have three disks in the second row with an inline arrangement where the disks are located in the wake of the first row. Figure 20 shows the arrangement for the three different submerged setups that will be tested.

In Figure 21 the red dotted lines represent the disks in the second row in WF5, whereas the

(a) (b) (c)

Figure 20: Pictures from conducting the experiments at MarinLab. a) The setup for downstream measurements of WF5 b) Measurements of WF6 c) Upstream measurements of WF7

blue lines illustrate the disks in the second row for WF7. While the grey disks, that are placed right behind the front row in WF6. As earlier mentioned the velocity profiles upstream and downstream are measured by the ADV Vectrino+. It is mounted to the automated traverse that can move the ADV with millimeter precision to a given position to get horizontal speed profiles with different distances to the disks. The velocity profiles for upstream blockage will be performed at distances -1D and -0.4D concerning the front row. For WF5 and WF7 it will additionally be performed upstream measurements for three points at -2.5D, -2D, -1.5D, and -0.7D. The downstream measurements will be performed at the distances 2D, 6D, 8D, 10D and 12D from the first row. The distance from the center of the disks and the water surface is set to 0.3 m to minimize the surface effects on the water surface. Figure 21 shows the measuring points for the different setups. Where the upstream measurements are illustrated with an $\times$, the additional three point measurements as a diamond, $\diamond$, and the downstream measurements with a circle, $\circ$. The measurements will be performed from the middle disk's center in the front row to 6.5D, which is 0.2 m from the walls. Due to the assumption that the setup is symmetric, as long as the angles of the disks are correct and there is nothing else in-between the disks, the velocity fields behind the disks will be symmetrical. Therefore it will be time-saving to only measure half profiles as shown in Figure 21.

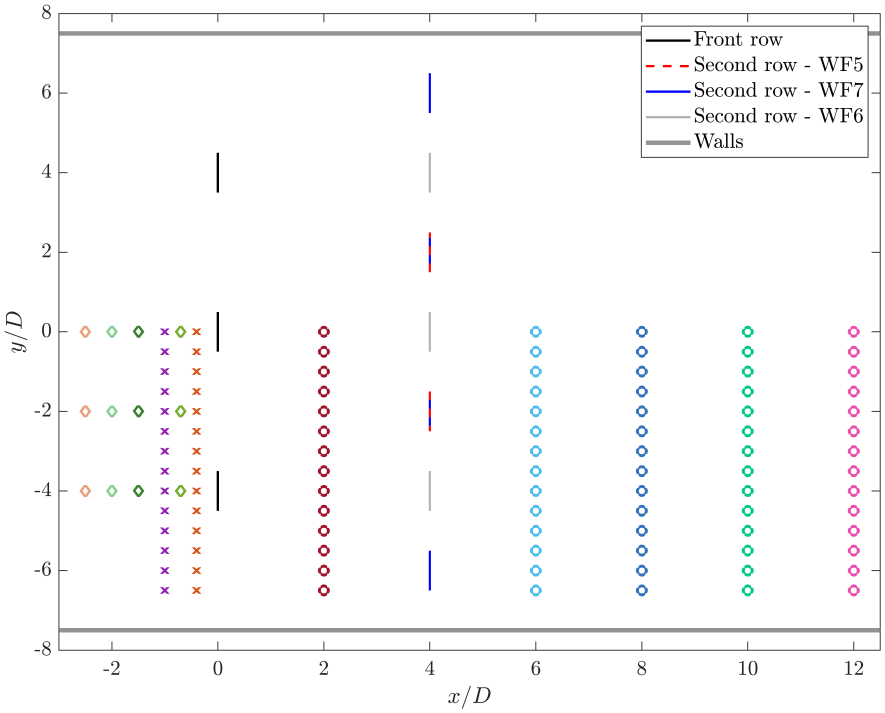

Figure 21: Illustration of the different setups and measurement points. Where upstream measurements are presented as ×, downstream measurements as ○ and additional three point upstream measurements for WF5 and WF7 as ◇

Table 2 shows the test matrix of all the scheduled experiments.

Table 2: Test matrix for all different setups showing different details for each setup

Setup		Type of measurement	Parameters	Number of measurements
WF7	Wake	Velocity profiles at 2D, 6D, 8D, 10D and 12D	U_{mean}, TKE	117
	Blockage	Velocity profiles at -1D and -0.4D Three points measured at -2.5D, -2D, -1.5D and -0.7D	U_{mean}	37
WF5	Wake	Velocity profiles at 2D, 6D, 8D, 10D and 12D	U_{mean}, TKE	103
	Blockage	Velocity profiles at -1D and -0.4D Three points measured at -2.5D, -2D, -1.5D and -0.7D	U_{mean}	50
WF6	Wake	Velocity profiles at 2D, 6D, 8D, 10D and 12D	U_{mean}, TKE	94
	Blockage	Velocity profiles at -1D and -0.4D	U_{mean}	39

3.2.1 Data processing

The Vectrino+ ADV is used to measure the velocity deficits that show the blockage and wake effects. This instrument measures four-velocity components and produces a time series for each component. Because it is necessary to investigate the velocity alternations in front and behind the disks, the ADV is mounted to measure the x-component. The carriage will move 30 meters with a speed of 0.5 m/s, and the ADV has a sampling frequency of 200 Hz; this means that the ADV performs around 12 000 measurement points in each run. The software for Vectrino+ will collect data for each run. To evaluate the measured data it is necessary to import the recorded time series into MATLAB. MATLAB will be used to evaluate and clean up the signals and for temperature correction, as well as represent the results.

Figure 22 shows a time series where the blue signals are the temperature corrected signals from the measurement, this is necessary due to a broken temperature sensor for the ADV. At the start of each run, the carriage will experience acceleration before it obtains constant velocity; therefore, it is necessary to cut the first 10 seconds in every run and the last 5 seconds due to declaration. As seen from the figure, there are significant spikes in the original signal; they occur because the acoustic signals do not reflect from the particles in the water because of poor seeding. To remove these spikes the Hampel filter is used, the goal of this filter is to identify and replace outliers in a given time series. The Hampel filtered signals can be observed in the figure by the red lines. When using the Hampel filter, it is necessary to introduce two parameters k and $n\sigma$. k represents the number of surrounding samples taken into account for filtering, and $n\sigma$ is the number of standard deviations the sample must differ from the local median to be identified as an outlier. The parameters for the Hampel filter for processing all the data in this thesis were $k = 200$ and $n\sigma = 2.4$. Additional to the Hampel filter, a low-pass filter is added to remove high-frequency noise in the signal. The allowed frequency for the passing signal is 20 Hz and is shown as with yellow color. To the right in Figure 22 the signals from 14 seconds to 21 seconds is shown, this zoomed area is presented to show a more detailed view on how the signals changes and the function of the filters, e.g., how the Hampel filter removes the outliers from the original signals. The measurement parameters that will be evaluated from the collected data is the mean velocity deficit and the turbulent kinetic energy in the downstream

wake.

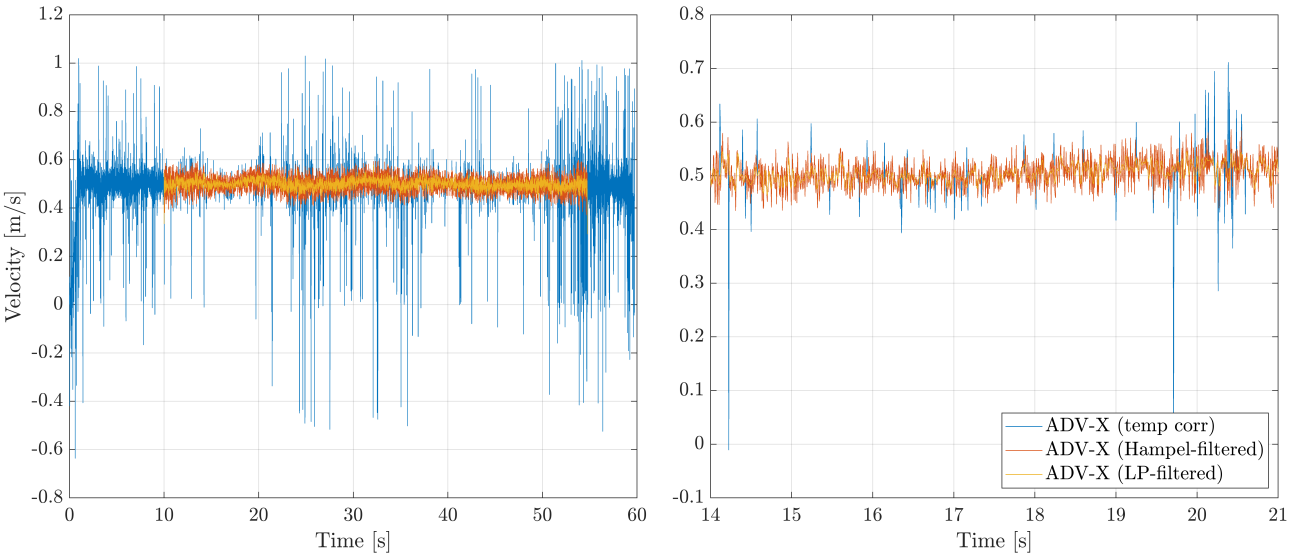

Figure 22: Graph showing the temperature corrected signals, Hampel filtered and Low-pass filtered signals (left) and a zoomed area to show how the filters processes the data (right)

To present the results is has been necessary to interpolate between the measurement points to visualize how the velocity deficit changes along x/D and y/D. Interpolation is a mathematical process of matching a point using known function values in nearby points. There are several types of interpolation, and the interpolation function used in MATLAB is makima. Makima stands for Modified Akima Interpolation. It performs a spline interpolation with low-degree polynomials in each interval and chooses the polynomial pieces to fit smoothly together [40].

3.2.2 Velocity deficit

To find the average velocity, U_{mean}, Equation (25) is used. Where N is the number of samples and U_i is the velocity measurement for each sample.

$$U_{mean} = \frac{1}{N} \sum_{i=1}^{N} U_i \tag{25}$$

In this thesis the results will be presented as the non-dimensional parameter velocity deficit, which is the ratio of the mean velocity U_{mean} and the free stream velocity U_0 as shown in Equation (26).

$$\text{Velocity deficit} = \frac{U_{mean}}{U_0} \tag{26}$$

3.2.3 Turbulent kinetic energy

Turbulent kinetic energy (TKE) is the part of the kinetic energy that is associated with eddies in a turbulent flow. To quantify the turbulent kinetic energy per mass, it is necessary to take the turbulent part for the wind, the deviation from the average, and calculate the kinetic energy of this with the following equation:

$$TKE = \frac{1}{2}((u')^2 + (v')^2 + (w')^2) \tag{27}$$

The kinetic energy is only being preserved as the average in an actual stationary turbulent current. If TKE is not normalized, the energy will depend on Reynolds' number. Therefore, it is common to normalize TKE by dividing the square of the incoming flow to obtain a non-dimensional normalized turbulent kinetic energy. This is how the development of turbulence in the wake will be presented, by using the expression $TKE/{U_0}^2$.

3.3 Measurement uncertainty

When performing experiments, multiple elements can contribute to sources of error in the measurements. The measurement error is the difference between a measured value and the actual value for a single measurement. A measurement error is composed of two types: random and systematic error. The random error is the difference between a single measurement and a large number of measurements of the same magnitude performed under the same conditions. The systematic error is the difference between the mean value of many measurements performed under the same conditions and the actual value. A systematic error will give a deviation every time we measure. It can be a constant deviation or vary systematically with time or other parameters.

Systematic error

The setup is mounted by hand, which may cause inaccuracies in the distance between the disks and ADV. The ADV must be aligned perfectly with the direction of the carriage to avoid

decomposition of the velocity component. The experimental tests in this thesis are all conducted by using an ADV. As presented in Section 3.1.1 the ADV is dependent on tiny silver-coated particles added to the tank in MarinLab to function. The particles have been distributed in the water, but they tend to sink to the bottom after some time. Therefore, it is necessary to mix the particles using the wave generator after a given time. The quality of mixing is not possible to quantify, but the signals from the ADV indicate when the mixing is sufficient.

Random error

The condition in the tank at MarinLab will differ from each measurement. As mentioned above, the particles will be in motion and have a different location during each run. The accuracy of the ADV is affected by the distribution of the particles. As well as the turbulence caused by the previous run can affect the conditions for the next run. Hence, it is vital to have a long enough pause between each run. The towing carriage and the instruments at MarinLab are not made to prevent random noise. The most significant error source in these experiments is human errors, as mentioned in systematic errors.

3.3.1 Uncertainties of ADV

As the measurement instrument depends on the distribution of the silver-coated particles in the tank, the surroundings will vary continuously, and it is, therefore, necessary to investigate the precision and accuracy of the ADV. Figure 23 shows three measurement points with corresponding error bars at y/D = 2.5, 3.5 and 6.0 when x = 8D. The measurements at y = 2.5D have been conducted four times, while the two other was three times. At y = 2.5D and 3.5D is the location of the edges on the disks. The deviation is largest at this position due to the mixing in the shear layer, and it is where some of the largest gradients are in the wake profile. At y = 6D is directly behind one of the disks, and the deviation at this point is relatively small.

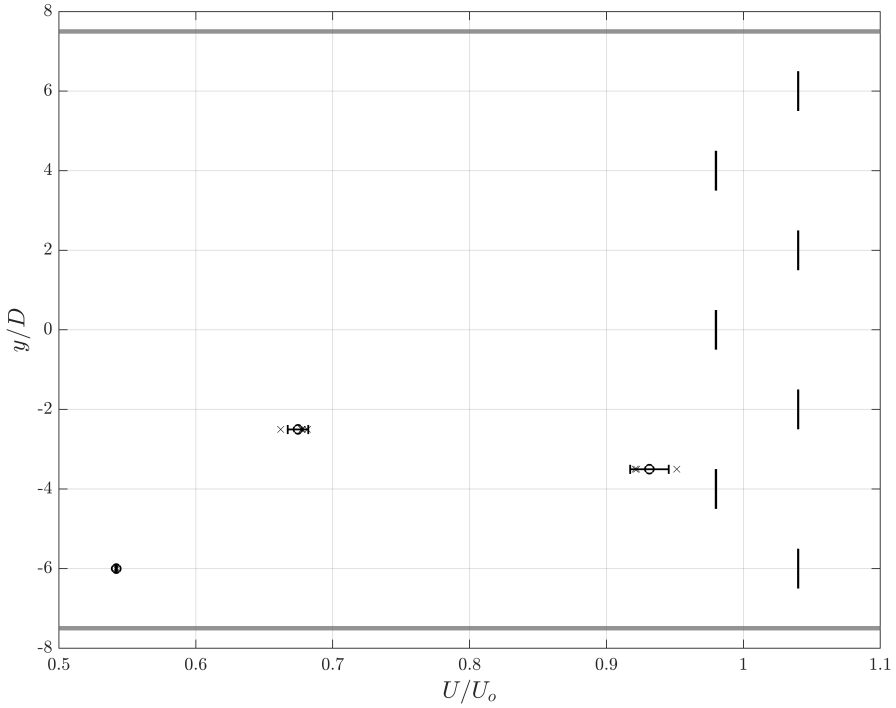

Figure 23: Measurement points at three different positions with corresponding error bars showing the standard deviation for the ADV at downstream measurements where x = 8D

Table 3 shows the relative standard deviation for the conducted measurements at the different positions, and it is relatively small, with values from 0.11% for the area behind the disk to 1.9% on the edge of the disk.

Table 3: Relative standard deviation of downstream measurements with ADV at three different positions

y/D	σ_{ADV} [%]
2.5	1.290
3.5	1.855
6.0	0.1060

Temperature correction for ADV

To assure that the ADV measured the correct velocity of the carriage, Bjørnsen performed some tests where the ADV was the only installed device without any obstacles in the water [19]. It showed a deviation in the measurements due to a broken temperature sensor. Therefore it is necessary to correct all the results from the experiments in MATLAB. When correcting the

temperature factor, the measured values agree with the velocity of the carriage. The relative standard deviation for the device with the temperature correction was 1.01% for $u = 0.5$ m/s.

3.4 Pre-experiments and results

This section will present the results from Bjørnsen [19] and how the turbulence in the water decays after a single run in MarinLab.

3.4.1 Blockage and wake effects with varying the lateral distance between the disks

This thesis builds upon the work that Bjørnsen [19] performed in 2021. He investigated the velocity deficit upstream and downstream, turbulent kinetic energy downstream, and axial forces for multiple disk separation distances for three porous actuator disks. The experiments were performed with the ADV, Vectrino+ from Nortek.

The results from the experiments showed that significant blockage effects appeared for the setup with small lateral separation distances at y = 1D and 2D. Still, at larger distances, the effects were not noticeable. Bjørnsen affirmed that disks with a separation of 4D did not seem to affect one another and operated as an isolated single wind turbine. The results for x = 4D will later be presented in this thesis to compare with an additional row. Bjørnsen stated that increasing the lateral distance between the disks can lead to a more independent functioning as a single isolated turbine. And it was suggested to add additional arrays to investigate how more disks will influence the upstream and downstream behavior at the flow for different setups.

The development of the wake for an array with a distance of 4D between the actuator disks is shown in Figure 24a. The conducted measurements performed by Bjørnsen shows that the velocity deficit is largest at x =0.4D and 1D, while the wake recovers towards x = 10D. Between the disks the jet streams are present, with an increase in the velocity.

Figure 24b depicts how the non-dimensional turbulent kinetic energy is developing in the wake for WF3. The turbulence levels in this array are building up from just behind the disks at x = 0.4D to 4D. The turbulence in the flows are decaying towards x = 10D. The contour plot

shows that there is no presence of turbulence in the jet streams between the disks.

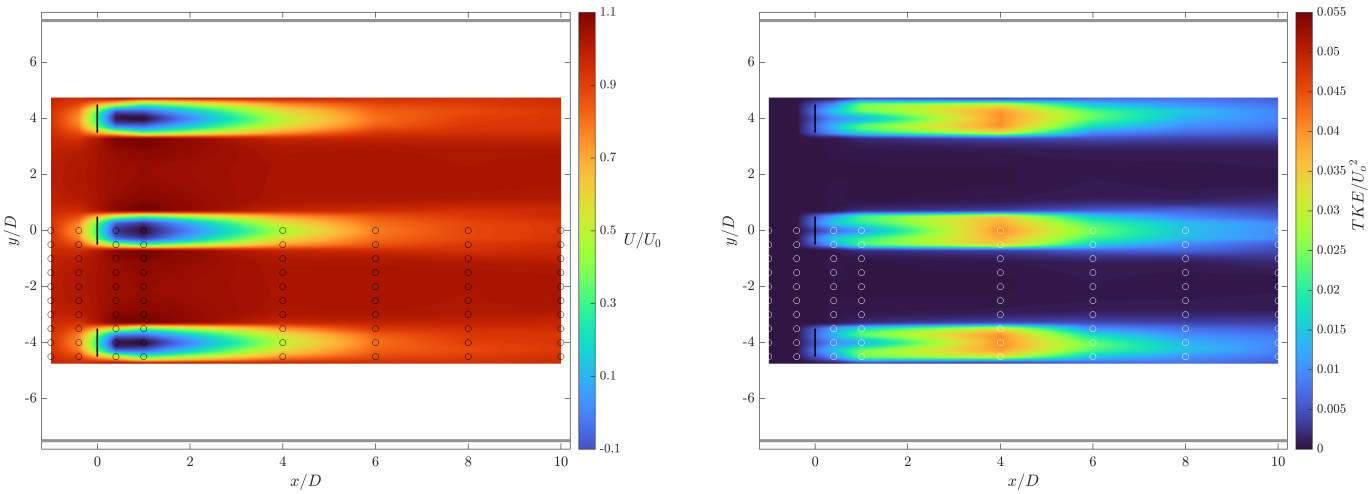

(a) Normalized velocity deficit

(b) Non-dimensional mean turbulent kinetic energy

Figure 24: Contour plot of normalized velocity fields and the non-dimensional mean turbulent kinetic energy development for WF3

As this thesis is based on the work that Bjørnsen executed [19], the front row in this setup is the same as he used. The results for the setup where the lateral distance between the disks was 4D will be used to compare how the wake changes when adding another row of disks in the wake of the front row. For this reason, Figure 24 will be further investigated in the discussion section.

In addition, different pre-experimental tests were conducted to investigate the sufficient depth at which the water surface no longer influences the w-component in the measurements. The experiments found that a depth of 30 cm showed the lowest w-component for the downstream measurements and an acceptable component for the upstream. As earlier mentioned, free water surface can cause a dip behind the setup. This dip seemed to increase with higher velocities. Therefore it was concluded that 0.5 m/s was an acceptable velocity.

3.4.2 Decay test of turbulence

To determine the length of the pause between each run was going to be, preventing turbulence in the water, it was necessary to perform a decay test. It was conducted by collecting data as

the carriage was on its way back to its starting position and the following five minutes when the carriage was standing still. Figure 25 shows the result for the test. The graph to the left shows the development of the velocity components when the carriage slows down from a velocity of 0.5 m/s to 0 in the x-direction. The time series is split into 50 second time intervals, as shown with black horizontal lines in the left figure. For each interval, the standard deviation for each velocity component has been calculated and plotted in the figure to the right. The TKE for the first interval is too large to get a detailed view of how the turbulence decays, and it is not included. The turbulence in the water decays to $2.1 \cdot 10^{-4}$ $\mathrm{m^2 s^{-2}}$ in the second interval, and the TKE decreases further to $8.7 \cdot 10^{-5}$ $\mathrm{m^2 s^{-2}}$ in the last interval. The TKE in the water is relatively small after three minutes. Therefore it will be recommended to wait for at least three minutes before starting a new run.

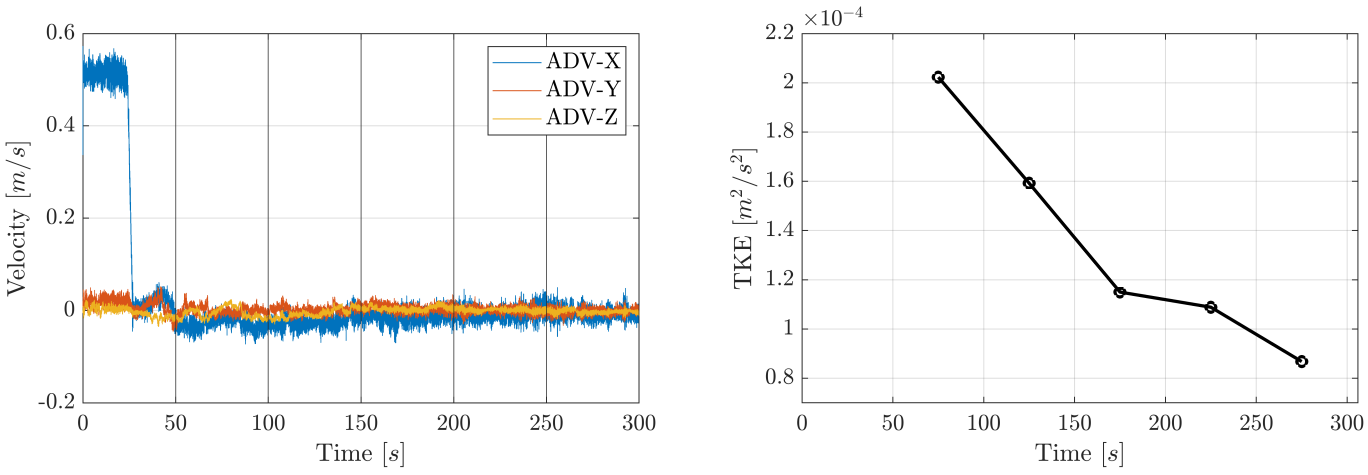

Figure 25: Decay test of the turbulence after a run in MarinLab showing the three velocity components at the left and the development of the non-dimensional turbulent kinetic energy at the right

4 Results

This chapter will present the results from the conducted experiments for the three different setups showing the velocity deficit upstream and downstream, as well as the development of the turbulent kinetic energy downstream.

4.1 Wind Farm 5

This section presents the velocity deficit profiles and turbulent kinetic energy development for WF5. The measurement points and the setup are shown in Figure 26 below. The lateral distance between the disks is 4D, the distance between the rows is 4D, where the arrangement of the disks is laterally offset. In this section, the velocity deficit and the kinetic turbulence energy development for WF5 will be analyzed and annotated.

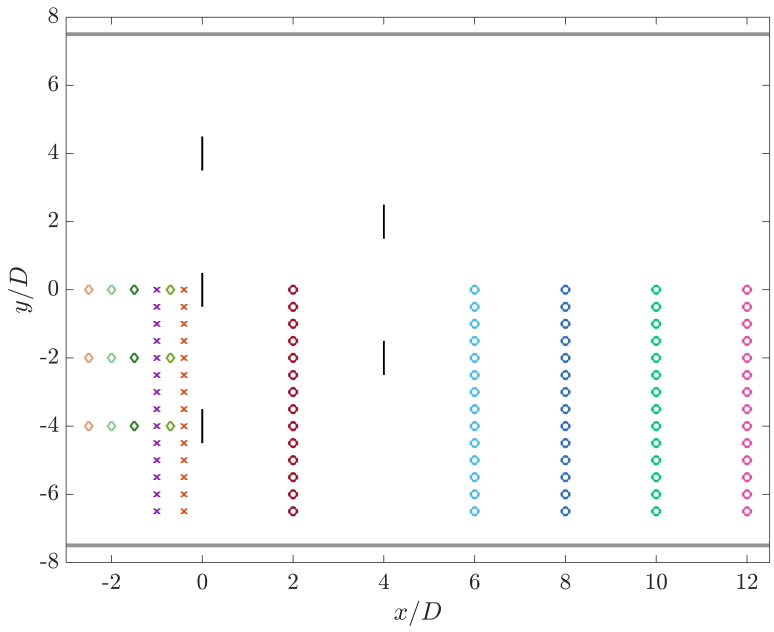

Figure 26: Illustration of the setup for WF5 with a laterally offset arrangement, displaying the measurement points for the upstream at x = -1D and -0.4D (×), downstream at x = 2D, 6D, 8D, 10D and 12D (○) and three additional upstream measurement points at x = -2.5D, -2D, -1.5D and -0.7D (◇)

4.1.1 Overview of the velocity deficit upstream and downstream

An overview of the normalized velocity in WF5 is depicted in Figure 27, where the time-averaged velocity U is normalized by the free-stream velocity U_0. Hence the conduction of measurements has only been performed at 2D behind the disks. The contour plot does not give a representative picture of the near-wake in reality. Therefore, the areas behind the disks are covered by a white box. Except for the deviations in the near-wake, the figure is a good presentation of the wind farm flows. Upstream of the front row, it is possible to observe that the velocity is decreasing due to the blockage effect. Between the rows at x = 2D, the velocity deficit behind the disks is larger than the deficit behind the disks in the second row at x = 6D. Although, the wake of both rows shows a reversed flow. At x = 6D, it is also possible to notice the presence of the accelerated jet streams between the disks. The contour plot shows that the wake has almost fully recovered at x = 12D. The velocity deficit upstream and downstream will be investigated further in the following sections.

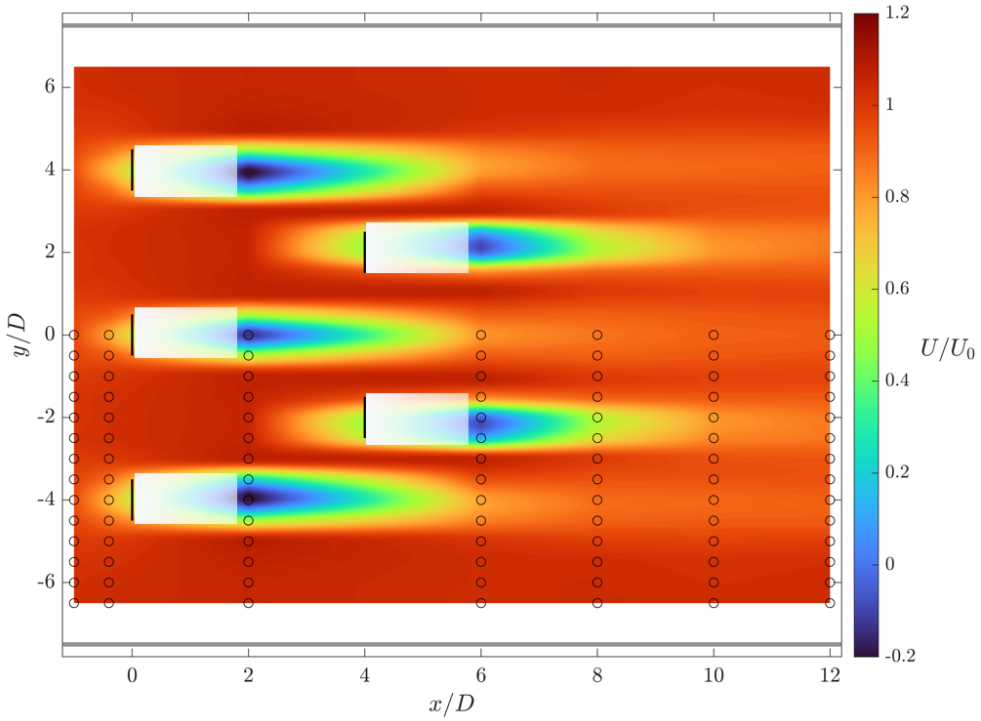

Figure 27: Normalized total velocity fields for WF5. The white boxes are present to hide the results in near wakes that are not representative from the contour plot. The black circles illustrates the measurement points

4.1.2 Overview of the non-dimensional mean turbulent kinetic energy

Figure 28 shows the non-dimensional mean turbulent kinetic energy development upstream and downstream for WF5. There is no turbulence in the front of the disks in the flow. As for the normalized velocity contour plot, the closest measurement point behind the arrays is x = 2D. This causes an incorrect picture of the turbulence in the near wake for both rows—especially when analyzing the turbulence behind the first row. At x = 2D, the turbulence development at both disks is nearly identical. Further downstream, the turbulence is decaying towards x = 12D. The lack of measurements between x = 2D and 6D shows that the assumed most significant turbulence in the wake behind the front row will not be observed. Behind the second row at x = 6D, there are two distinct peaks with a greater magnitude than at x = 2D. Further downstream, the turbulence kinetic energy builds up toward its maxima at x = 8D before it starts to decay at x = 10D towards x = 12D. The turbulent kinetic energy between the disks shows no presence of turbulence in the jet stream and shows a clear distinction of the wakes. The bypass flow outside the edge disks illustrates a similar behavior to the jet streams.

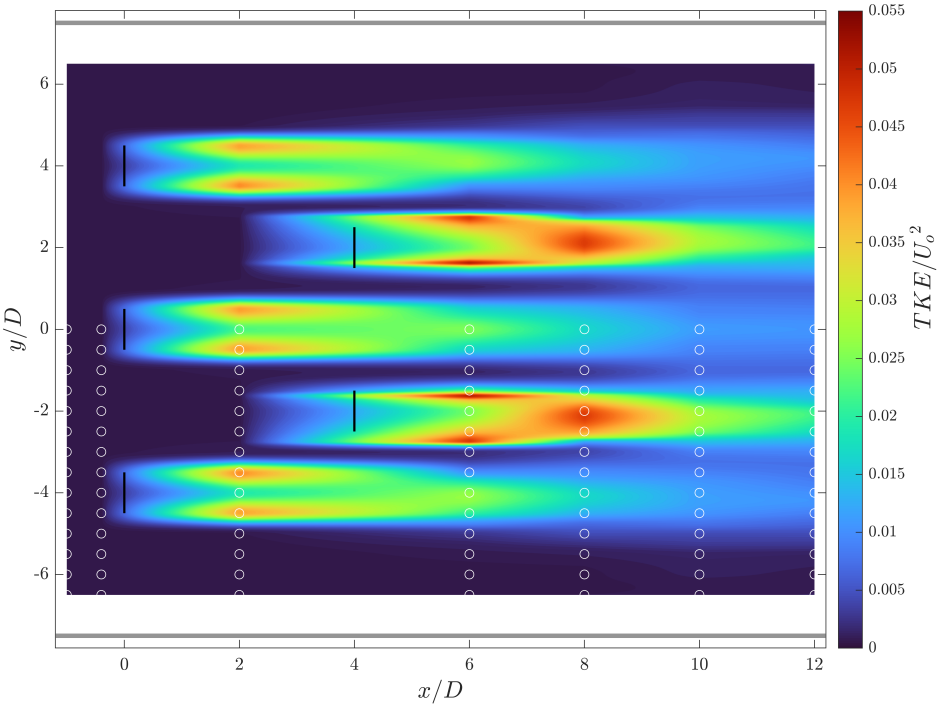

Figure 28: Contour plot of the non-dimensional mean turbulent kinetic energy development in WF5. The white circles illustrate the placement of the ADV for the conducted measurements

4.1.3 Upstream measurements

From Table 4 the upstream velocity deficits at the edge disk, center disk and between them are presented and Figure 29 shows how it develops. At x = -2.5, the velocity for the three points is almost identical and indicates that the blockage effect is not present at this distance. Towards the disk, the edge and center disk experience a larger deficit, where the edge disk is slightly larger. At x = -0.4D, the velocity in front of the center disk decreases to 79%, while the edge reduces to 76%. Between the disks, at y = 2D, the velocity increases after x = -1.5D, to 3.1% at -0.4D. The profiles at x = -0.4D and -1D will be further analyzed.

Table 4: Axial upstream velocity deficits for WF5

x/D	y/D = 0.0	y/D = 2.0	y/D = 4.0
-0.4	0.7932	1.0309	0.7724
-0.7	0.9002	1.0240	0.8964
-1	0.9606	1.0172	0.9493
-1.5	0.9990	1.0083	0.9865
-2	1.0146	1.0284	1.0081
-2.5	1.0169	1.0167	1.0159

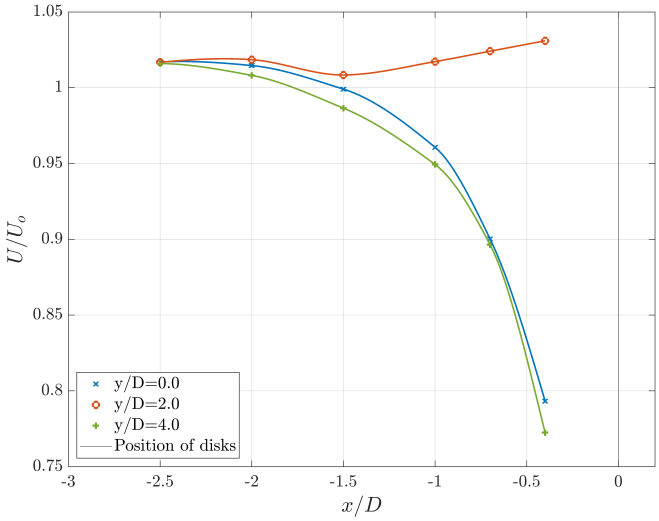

Figure 29: Axial upstream velocity deficit development for WF5 at y = 0D, 2D and 4D

The upstream velocity profiles at x = -0.4D and -1D are shown in Figure 30. At x = -1D, the velocity deficit at the disks is 95%. The jet streams are visible around y = -2D, as the velocity increases near the edges and reduces in front of the disks. Towards the wall, the velocity increases further towards an increase of 3%. At x = -0.4D, the blockage effect is more extensive, as the center and edge disk experience a deficit of respectively 79% and 77%. The suction effect between the disk leads to a 4% higher velocity approaching the disks in the second row. The dip at y = -2D can be explained by small-scale effects from the holes in the porous disks. The velocity will increase towards the wall, where the velocity of the jet stream outside the array increases to 4% above U_0.

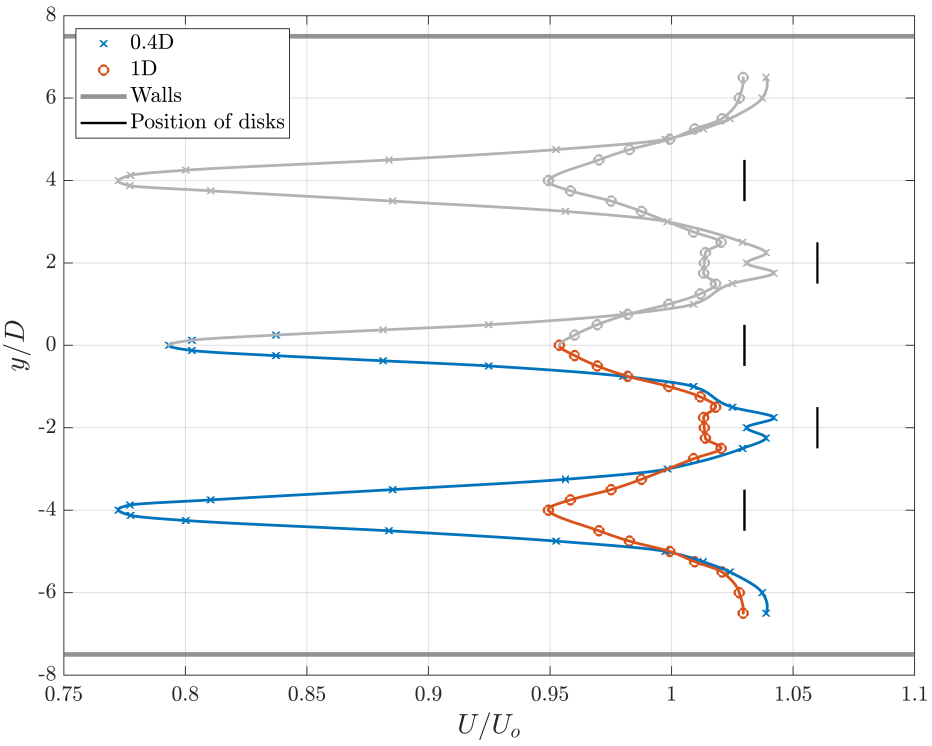

Figure 30: Upstream blockage velocity deficit for WF5 at x = -0.4D and -1D

4.1.4 Downstream measurements

In this section, the results for the downstream measurements will be analyzed on behalf of the velocity deficit and the non-dimensional turbulent kinetic energy development in the wake. It is split into two sections for x = 2D and 6D, and x = 8D, 10D, and 12D.

x/D = 2.0 and 6.0

Figure 31a illustrates the velocity deficit in the wake downstream at x = 2D and 6D. At x = 2D, the wake behind the edge disk experiences a higher deficit than the center disk, with -20% against -14%. In front of the disk in the second row, the velocity increases with 6.1% to U_0. Towards the walls in the tank, the velocity is growing towards the same magnitude as between the disks. Further downstream towards x = 6D, the wake behind the disks in the front row experiences a velocity loss of 80%. The jet streams between the disks increase towards a similar magnitude as x = 2D until the disks in the second row encounter a deficit of -5%. Towards the

walls, the bypass velocity increases to a 2% larger magnitude than the inflow velocity.

The non-dimensional turbulent kinetic energy can be investigated in Figure 31b. The development of turbulence behind the front row at x = 2D is similar at the disks, but the center disk experience slightly higher turbulence than the edge. There is no turbulence in the jet streams between the disks and in the bypass flow towards the walls. At x = 6D, the turbulence in the wake of the disks in the front row is similar. The turbulence decays between the disks until the turbulence level increases behind the disk in the second row towards a higher level than disks in the front row at x = 2D. As the turbulence levels are dependent on the free-stream velocity, the jet streams between the disks in the first row generate a higher incoming velocity in the second row. It is necessary to divide TKE by $(1.06U_0)^2$ shown as dotted lines in Figure 31b. The turbulence behind the disks in the second row gets nearly identical with the turbulence development behind the center disk in the front row. Indicating a similar behavior for the turbulence in the wake of the disks.

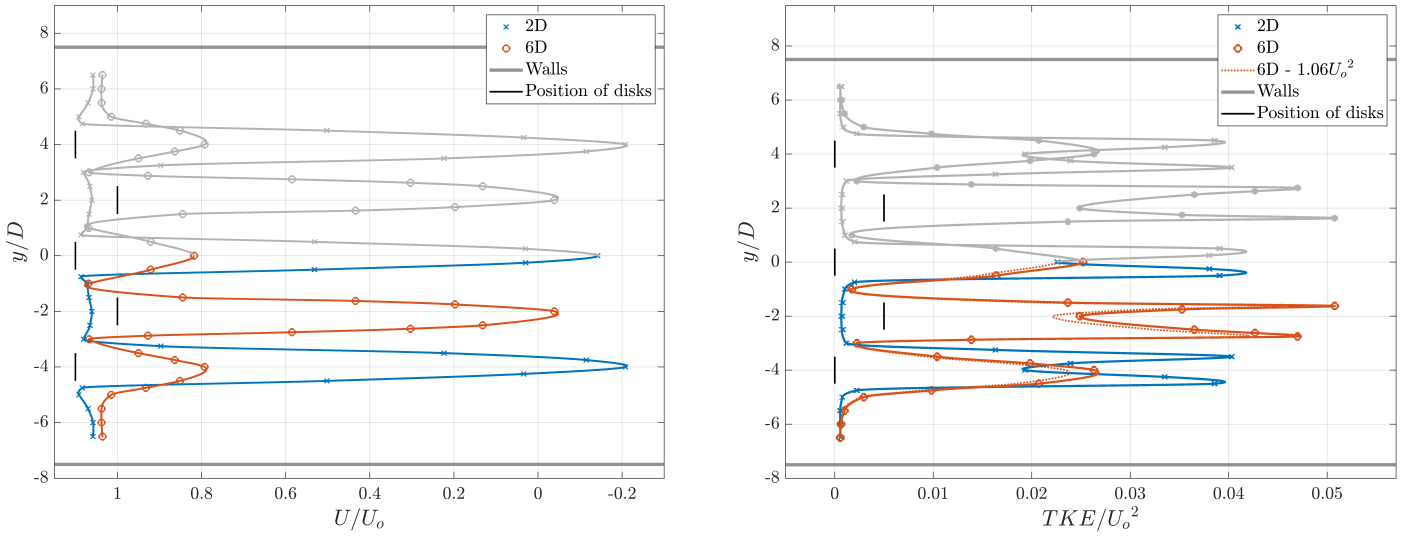

(a) Downstream velocity deficit

(b) Non-dimensional mean turbulent kinetic energy

Figure 31: Downstream velocity deficit profiles and turbulent kinetic energy development at x = 2D and 6D for WF5 with a laterally offset arrangement

x/D = 8.0, 10.0 and 12.0

The wake development further downstream is depicted in Figure 32a. At x = 8D, the velocity deficit at the center disk in the front row is 87%, while at the edge disk, it is 89%. In the jet

streams between the disks in the front and second row, the velocity builds up towards U_0 until it decreases towards 55% behind the disks in the second row. Towards the walls, the bypass flow experiences an increase of 4% in the inflow velocity. At x = 10D, the wake behind the disks in the front row has recovered to 90%, while in the second row, the deficit is 81%. Further downstream at x = 12D, the wake is still recovering and has only increased by 1% for the disks in the first row. In the second row, the deficit has decreased to 87%. The jet streams between the disks decrease further as the stream-wise direction increases, showing that the wakes tend to merge behind x = 12D.

Figure 32b shows the non-dimensional mean turbulent kinetic energy in the far wake. At x = 8D, the turbulence levels are reaching their maxima behind the disks in the second row. In the jet streams between the disks, the turbulence is almost zero, and towards the walls, the levels are even smaller. When moving further downstream, the turbulence decreases further behind the disks, where the most significant turbulence levels occur behind the disks in the second row. At the center disk in the front row, the turbulence levels at x = 10D and 12D are almost identical, while the difference at the edge disk is slightly larger. Despite a decrease in the turbulence downstream in the wake behind the disks, the turbulence levels between the disks are increasing. This may imply that the wakes tend to merge in the far wake. Similar to 32a, the flow near the walls is almost identical for all distances. The turbulent kinetic energy divided by the increased inflow velocity for the second row is illustrated with dotted lines. It shows that the turbulence behind the front row at x = 8D is similar to the turbulence in the second row x = 12D. Indicating a similar development for the turbulence behind the two different rows.

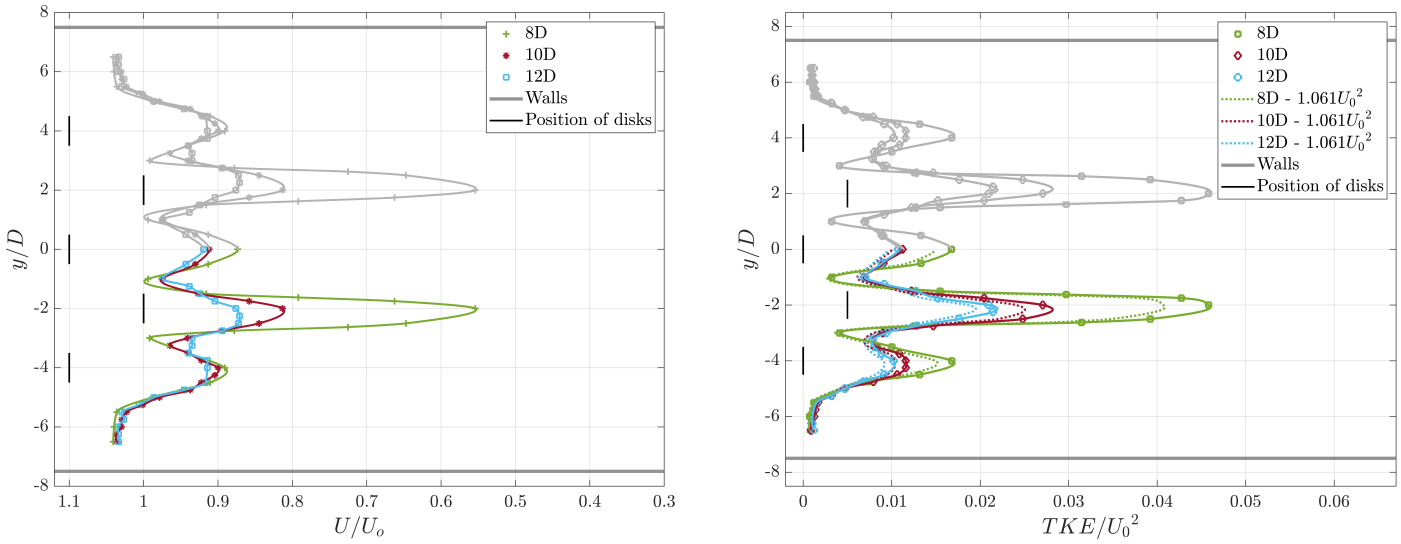

(a) Downstream velocity deficit

(b) Non-dimensional mean turbulent kinetic energy

Figure 32: Downstream velocity deficit profiles and turbulent kinetic energy development at x = 8D, 10D and 12D for WF5 with a laterally offset arrangement

Axial measurements

Figure 33 shows the development for the velocity deficit upstream and downstream for WF5. At x = -2.5D, the velocity is equal before approaching the wind farm. The velocity at y = 0D and 4D decreases towards the disks, explained by the blockage effect, which has already been investigated. From Table 5 the velocity deficits downstream at y = 0D, 2D and 4D are presented. The edge disk (y = 4D) in the front row experiences a larger deficit than the center disk (y = 0D) for all the cases, except at x = 8D. The difference between the disks is largest at x = 2D, where the edge disk has a 6.6% higher velocity deficit than the center disk. Further downstream, the difference between the velocity deficits is decreasing, and at x = 12D, it is only 0.52% difference in the velocity deficits, as the wake has recovered above 91% of U_0. The velocity deficit at y = 2D, between the disks in the front row at x = 2D, is 6.1% higher than the incoming velocity. This leads to a lower velocity deficit in the wake behind the second row at x = 6D. Further downstream, the velocity behind the disk in the second row tends to recover similar to the disks in the front row. This is observed by comparing the velocity deficits at x = 6D and 8D for the disks in the front row to x = 10D and 12D for the disk in the second row. The difference is largest at x = 12D, where the disk in the second row has a 1.8% higher velocity

deficit than the edge disk in the front row. The increased inflow velocity towards the second row leads to a lower velocity deficit in the near-wake but a slightly larger deficit downstream than the front row.

Table 5: Axial velocity deficits downstream for WF5

x/D	y = 0D	y = 2D	y = 4D
2	-0.142	1.061	-0.208
6	0.828	-0.029	0.804
8	0.873	0.554	0.891
10	0.912	0.813	0.900
12	0.919	0.873	0.914

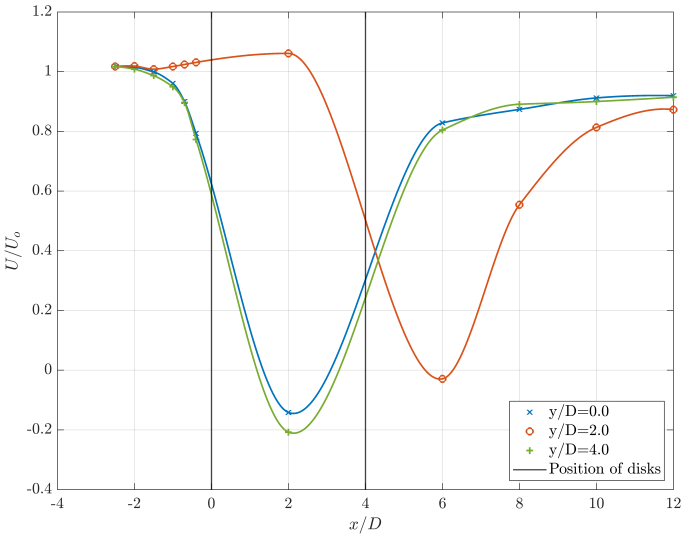

Figure 33: Axial velocity deficit development upstream and downstream at at y = 0D, 2D and 4D for WF5

4.2 Wind farm 7

This section presents the velocity deficit profiles and turbulent kinetic energy development for WF7. The measurement points and the setup are shown in Figure 34 below. The crosswind distance between the disks is 4D, the downwind distance between the rows is 4D, with a laterally offset arrangement.

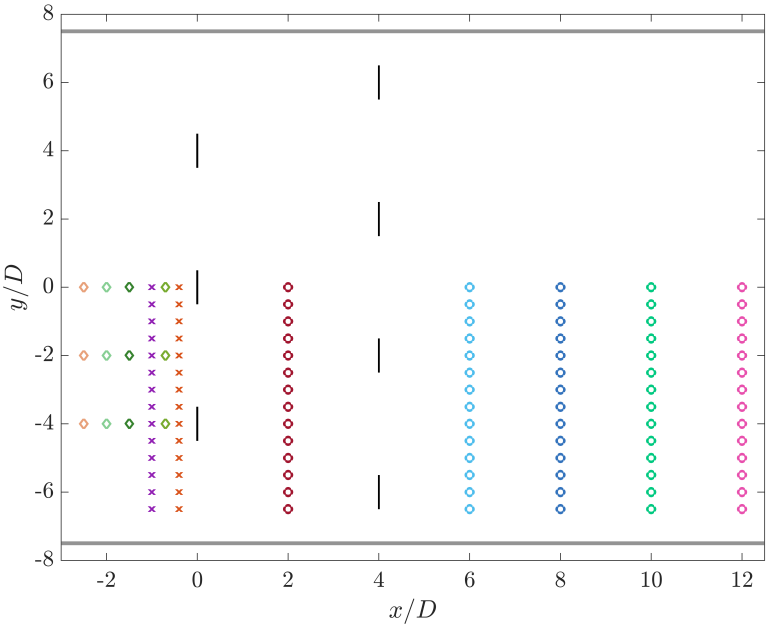

Figure 34: Illustration of the setup for WF7 with a laterally offset arrangement, displaying for the upstream measurements at x = -1D and -0.4D (×), downstream at x = 2D, 6D, 8D, 10D and 12D (○) and three additional upstream measurement points at x = -2.5D, -2D, -1.5D and -0.7D (◇)

4.2.1 Overview of the velocity deficit upstream and downstream

The normalized velocity deficit in WF7 is shown in Figure 35. Since the measurements only have been conducted at x = 2D behind both rows, the area behind the disks is not representative of the near wake phenomenon and is therefore ruled out with a white box. Except for the deviation in the near-wake, the contour plot is a suitable approach to illustrate the velocity deficits in a wind farm. The upstream velocity deficits of the first row show a decrease in the velocity right in front of the disks. At x = 2D, the velocity deficit is negative, implying a reversed flow in the wake of the front row. The velocity deficit at x = 6D behind the second row is slightly smaller than the front row. At x = 6D, the jet streams with an increased velocity between the disks

are visual. Towards x = 12D, the wake is recovering towards the free-stream velocity. In the following sections, the various aspects from Figure 35 will be more explored and commented on in deeper detail.

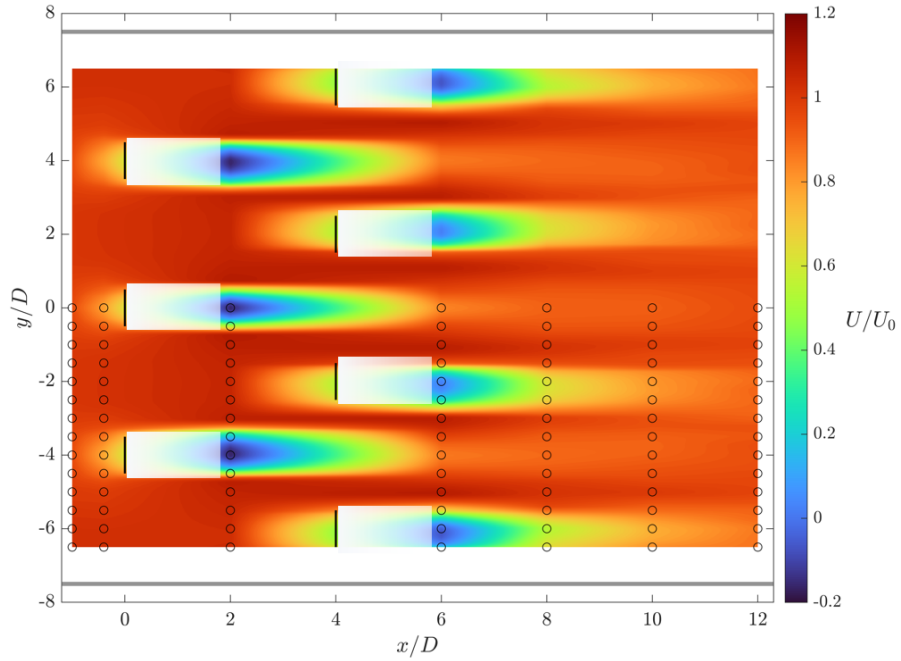

Figure 35: Normalized total velocity fields for WF7. The white boxes are present to hide the results in the near wake that are not representative from the contour plot. The black circles illustrate the measurement points

4.2.2 Overview of the non-dimensional mean turbulent kinetic energy

Figure 36 shows the non-dimensional turbulent kinetic energy development in the wake for WF7. The turbulence level is zero in front of the disks in the first row. At x = 2D, between the two rows, there are distinct peaks at the edges of the disks. The turbulence behind the front row is incomplete due to no performed measurements between x = 2D and 8D. Moving further downstream, the flow behind the second row tends to have the same distinct peaks as the front row, but the magnitude is greater. At x = 8D, the turbulence builds up towards a single peak. Further downstream, the turbulence levels behind the second row are still high at x = 12D. At this point, the turbulence in the wake for the front row is also still present. The jet streams separate the wake of the disks, and it shows that there is no turbulence in the flow between the disks. The turbulence will be further analyzed in the following section.

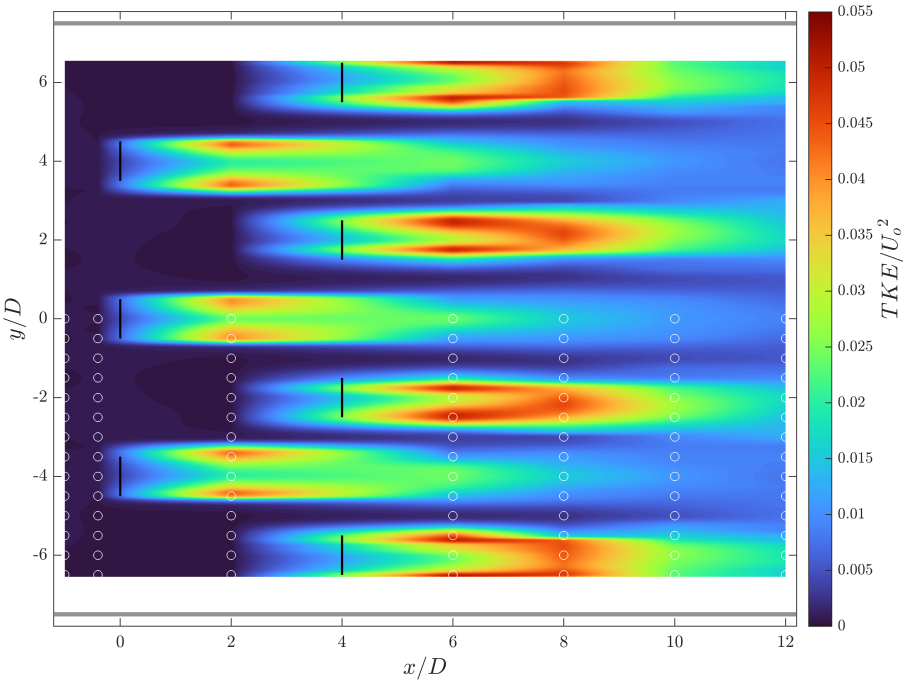

Figure 36: Contour plot of the non-dimensional mean turbulent kinetic energy development in WF7. The white circles illustrate the placement of the ADV for the conducted measurements

4.2.3 Upstream measurements

By observing the axial upstream flow in Figure 41, the velocity deficits at x = -2.5D indicate that the blockage effect will not affect the flow from this distance. Further, towards the disks, the velocity between the disks will be approximately constant with an increment of 2% above the free-stream velocity, U_0, except for x = -1D, where the velocity experience a small drop. The upstream velocity deficit will increase further towards the disks. The center and the edge disk will experience a similar velocity deficit at x = -0.7D by 20%, as shown in Table 6.

From the table, it can be observed that the edge disk will experience a higher velocity deficit than the center disk, which differs from the theory introduced by Segalini & Dahlberg [15]. The difference of the velocity deficit on the disks is largest at x = -0.4D, where the edge disk is 1.8% larger than the center disk. This is a relatively small difference, and due to uncertainties, it can be assumed that the velocity deficits are equal for the two disks. The turbulent kinetic energy profiles for x = -0.4D and -1D will be investigated further on.

Table 6: Axial upstream velocity deficits for WF7

x/D	y = 0D	y = 2D	y = 4D
-0.4	0.796	1.023	0.777
-0.7	0.907	1.022	0.900
-1	0.953	1.011	0.952
-1.5	0.999	1.020	0.988
-2	1.013	1.021	1.005
-2.5	1.021	1.019	1.016

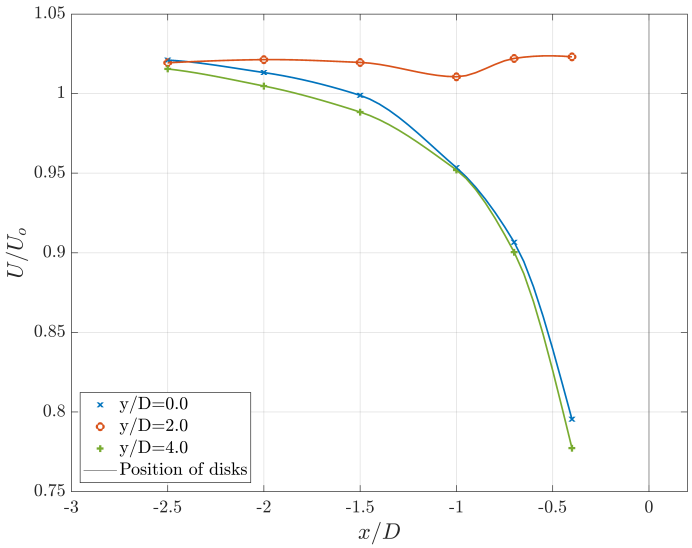

Figure 37: Axial upstream velocity deficit development for WF7 at y = 0D, 2D and 4D

Figure 38 shows the upstream velocity profiles at x = -0.4D and -1D. At -1D, the velocity deficit in front of the disks is 95 %. Between the disks, at y = -2D, it can be observed that the velocity increases 1% due to the suction effect. The jet stream at y = -5D is larger as the velocity increases by 4%. Moving closer to the disks at x = -0.4D, the flow in front of the disks experience an increase in the velocity deficit to 80% and 73%, where the edge disk experience the largest deficit, unlike the presented theory. It is noticeable that the suction effect increases closer to the disks at y = -2D and that the flow will grow by 2.5%. When investigating the flow between the wall and the edge disk, it is visible that the flow at -0.4D and -1D is similar. An explanation for this is the blockage effect from the walls that prevent the bypass flow from accelerating.

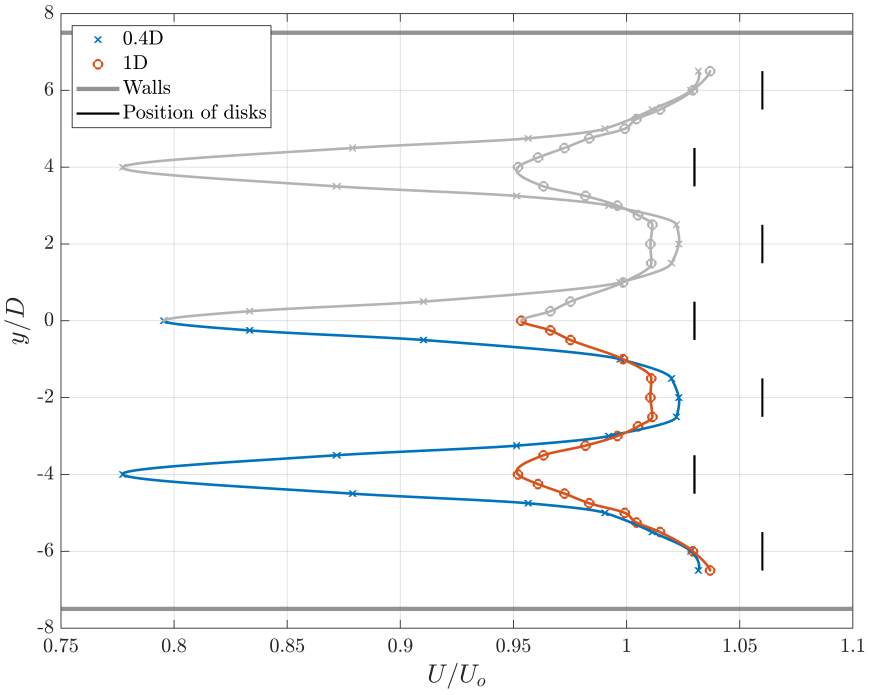

Figure 38: Upstream velocity deficit profiles when x = -0.4D and -1D for WF7, with makima interpolation between the measurement points

4.2.4 Downstream measurements

In this section, the results for the downstream measurements will be analyzed on behalf of the velocity deficit and the non-dimensional turbulent kinetic energy development in the wake. It is split into two sections for x = 2D and 6D and x = 8D, 10D, and 12D.

x/D = 2.0 and 6.0

The measurements at x = 2D are in the middle of the two rows, and from Figure 39a it shows that jet streams occur between the disks due to the blockage effects in the front row. This leads to a 6% higher velocity approaching the center disk in the second row and 4% at the edge disk. The velocity deficit for the first row is -20% for all the disks. It would be logical to compare the wake at x = 2D with x = 6D because the distance between the ADV and the respective rows is 2D. Thus, one can recognize how the blockage in the first row affects the wake in the second row. The velocity deficit is smaller for the second row at x = 6D than for the first row. The disk that experiences a higher incoming velocity will have a smaller velocity deficit at 4% for the disk in the middle. In comparison, the edge disk in the second row has a deficit of -6%.

As mentioned in Section 2.3.1, the turbulence in the wake will affect the recovery of the wake, and Figure 39b shows the ratio between the turbulent kinetic energy and the squared free-stream velocity U_0. The turbulence in the wake of the first row is approximately equal at both disks. The edge vortices cause the two distinct peaks at x = 2D on the disks. Between the disks, there is no turbulence. Due to the jet streams that are assumed to be uniform, eddies will not exist in this region. The turbulence behind the second row at x = 6D has the same form as at x = 2D, but the magnitude is larger behind both disks. As the non-dimensional mean turbulent kinetic energy depends on the incoming velocity, and it is shown that the flow approaching the disks in the second row is higher than the first row, it will be necessary to divide TKE with a 6% higher U_0. The red shows this dotted lines in Figure 39b. When dividing the TKE on the actual incoming velocity for the disks in the second row, it is shown that the turbulence levels are similar to the front row. But it is still higher levels of turbulence in the second row. An explanation for this phenomenon can be the difference in the incoming velocities at the disks. A more significant velocity in front of the disk will lead to higher turbulence in the wake, resulting in a lower velocity deficit.

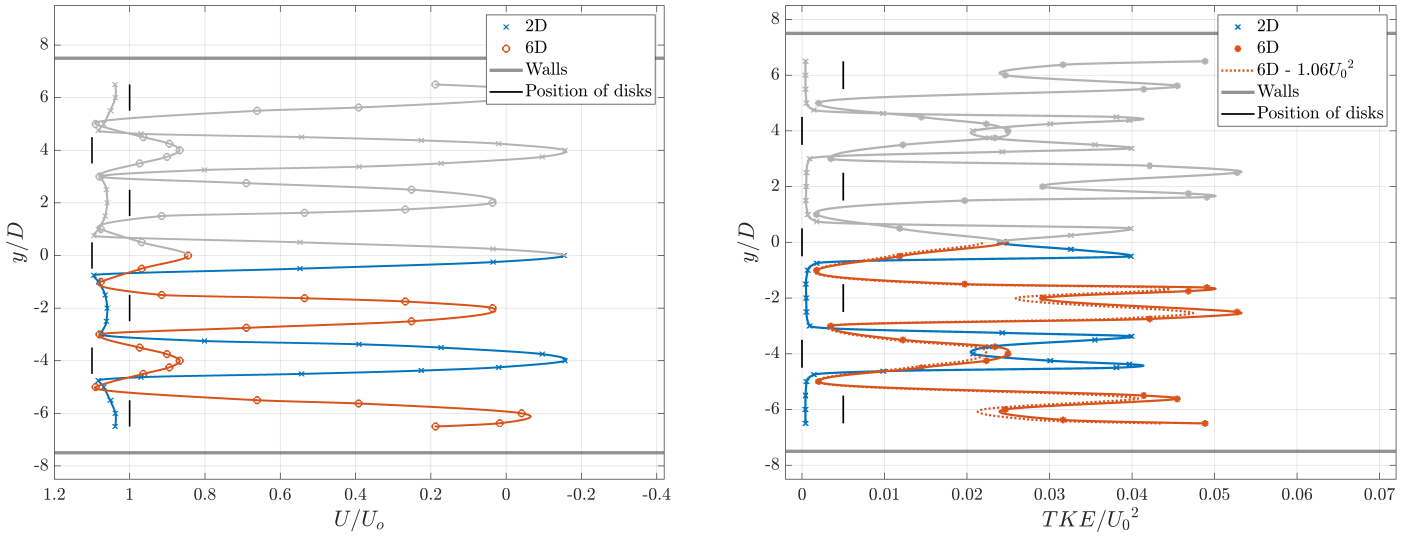

(a) Downstream velocity deficit

(b) Non-dimensional mean turbulent kinetic energy

Figure 39: Wake development for WF7 at x = 2D and 6D, with makima interpolation between the measurement points

x/D = 8.0, 10.0 and 12.0

From Figure 40a it shows that the measurements at x = 8D follow the same pattern as for x = 6D. In the second row, the velocity deficit is most significant at the edge disk with approximately 54%, whereas the disk in the middle experience a deficit of 62%. For the disks in the front row, the velocity has recovered to around 90%. The jet streams are still present between the disks, with a flow velocity of 2% higher than the incoming velocity. At x = 10D, the velocity deficit in the front row follows the same trend as for x = 8D, with a velocity deficit of 91% and 92% at the edge and center disk. The biggest difference is that the jet streams decrease, implying that the wakes start to merge. For the wakes in the second row, the deficit recovers to 81% and 77% for the center and edge disk. The velocity deficit is still larger at the edge disk, but the difference decreases. At x = 12D, the wake is unstable and, it is no longer a clear pattern. The velocity deficit is 95% at the disks in the front row. Between the disks, the flow is not exceeding the inflow velocity. Therefore, it can be assumed that the wake at this point has merged. For the disks in the second row, the velocity deficit is 89% and 86% at the middle and the edge disk. The deficit is slightly higher at the center disk.

At x = 8D, the TKE development for the disks in the first row are similar at both disks, with a magnitude of 1.6%. The disks in the second row have the same extent but a different form. The center disk has a single peak at 5%, and the edge disk has two peaks. That indicates that at x = 8D at the center disk, the TKE has reached its maxima, but there is still vortex shedding at the edge disk, and the TKE is building up towards its maxima magnitude. At x = 10D, the TKE is still a bit larger at the edge disk in the second row with 3.1%, while in the center wake, it is 2.8%. Further downstream at x = 12D, the TKE development follows the same path as x = 10D, just with a smaller magnitude. The most significant difference is that the turbulence between the disks is higher, which can be explained due to a merge in the wakes at this distance. The dotted lines illustrate the turbulence levels with a higher incoming velocity. Since the spacing between the first row at x = 8D and the second row at x = 12 is the same, it will be logical to compare the TKE at these points, showing that they are related. When comparing the green lines for x = 8D behind the first row to the dotted blue lines for x = 12D behind the second row, a similarity is observed in the turbulence levels—indicating

that the magnitude of the TKE is almost identical for the same distance behind the disks. The largest difference in the development of the turbulent kinetic energy in WF7 is that the edge disk in the second row experiences a slower growth of the turbulent kinetic energy and a slower recovery for the velocity. An explanation of this is that the distance between the centerlines of all the disks is 40 cm, while the distance between the centerline of the edge disk and the walls is only 30 cm. This will prevent the mixing of the free-stream velocity and will lead to a more significant blockage effect. Which again will lead to a higher TKE and a slower wake recovery.

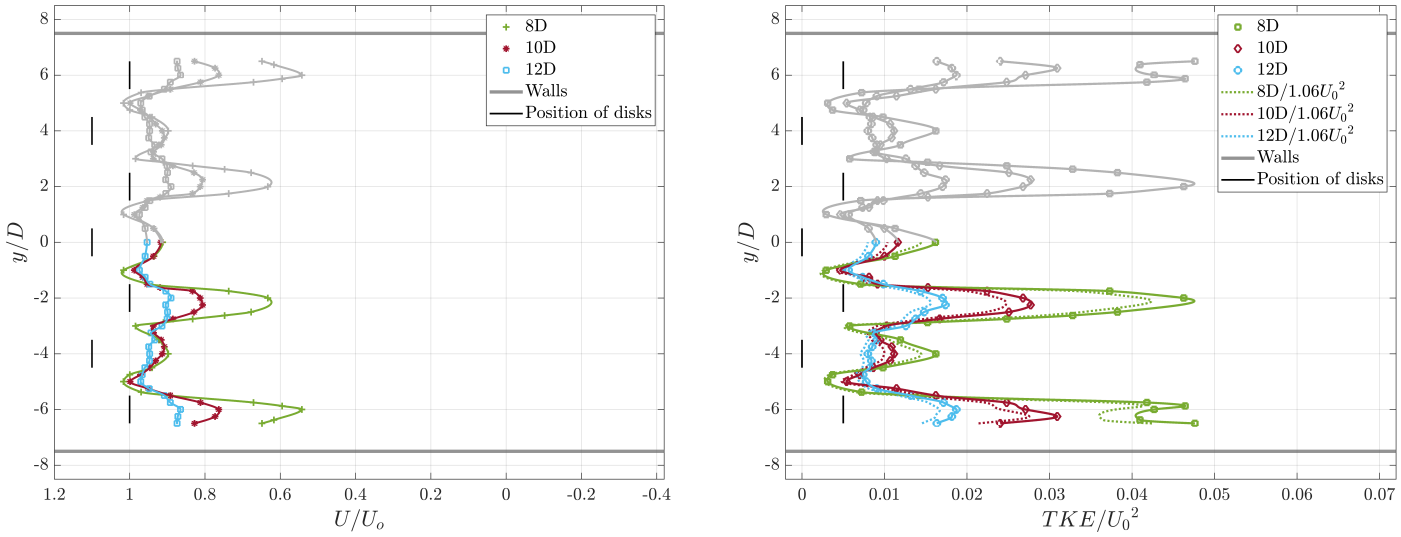

(a) Downstream velocity deficit

(b) Non-dimensional mean turbulent kinetic energy

Figure 40: Wake development for WF7 at x = 8D, 10D and 12D, with makima interpolation between the measurement points

Axial measurements

Figure 41 shows the axial development of the velocity deficit for WF7 for y = 0D, 2D, 4D and 6D, representing the center lines of the four disks. In Table 7 the velocity deficits have been quantified. The center disk and the edge disk in the front row show the same tendency, where the velocity decreases from the free-stream velocity at x = -2.5D to -15% at x = 2D. The negative velocity deficit indicates a reversed flow in the near-wake. Further downstream at x = 6D, the velocity deficit in the front row decreases to 86% and 87% behind the center and edge disk. While the wake recovers further towards the free-stream velocity at x = 12D as the velocity deficit is 96% and 95% of U_0.

The velocity deficit behind the disks in the second row differs from each other. At x = 2D, the velocity in front of the center disk (y = 2D) is 2.2% higher than the edge (y = 6D). A lower inflow velocity leads to a higher velocity deficit in the wake, which can be observed at x = 6D as the velocity deficit for the edge disk is 7.4% higher than the center disk. This is caused by the blockage effect from the walls in the water tank, as they are only 30 cm from the centerline for the edge disk. The presence of the walls prevents the bypass flow around the array to mix free-stream flow into the wake. This is affecting the recovery of the wake further downstream, as the edge disk shows a larger velocity deficit than the center disk. The difference is largest at x = 8D with 9.4% lower deficit, and smallest at x = 12D where it is 3.1%. Compared 4D behind the rows, at x = 6D, the velocity deficit is around 86%, while at x = 10D for the second row, it is 83% and 76%. While 6D behind the rows, the difference has become smaller. The front row experiences a velocity deficit of approximately 96%, while the center disk in the second row has 90% and the edge 87%. When comparing the velocity deficits in the wake for the front row against the second row, the velocity deficit in the near-wake is smaller for the second row. But the velocity in the wake for the front row shows a faster recovery.

Table 7: Axial velocity deficits downstream for WF7

x/D	y = 0D	y = 2D	y = 4D	y = 6D
2	-0.141	1.060	-0.147	1.038
6	0.856	0.033	0.870	-0.041
8	0.915	0.636	0.903	0.543
10	0.924	0.827	0.924	0.763
12	0.961	0.896	0.954	0.865

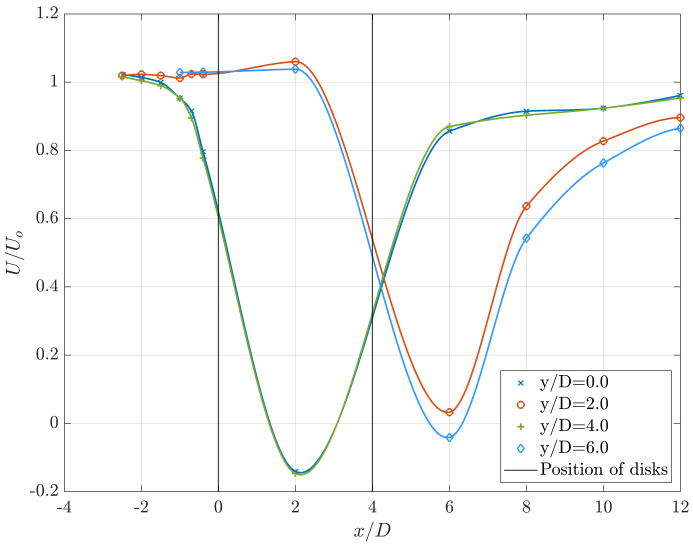

Figure 41: Axial velocity deficit development upstream and downstream at at y = 0D, 2D and 4D for WF7

4.3 Wind farm 6

This chapter will present the velocity deficit profiles and the turbulent kinetic energy development for WF6. The setup and the measurement points are illustrated in Figure 42. The disks are installed with an inline arrangement, and the lateral distance between the disks and the distance between the rows is 4D.

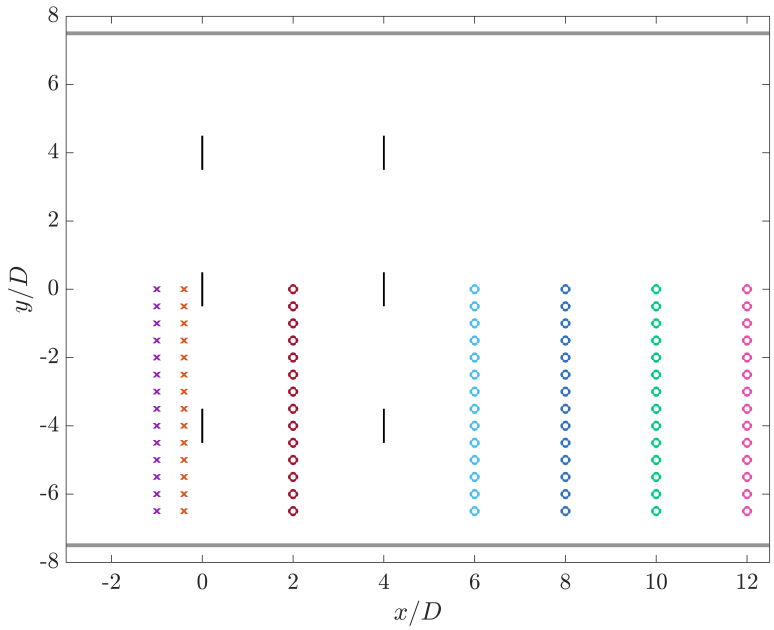

Figure 42: Illustration of the setup for WF6 with an inline arrangement, showing the measurement points for the upstream (×), downstream (○) and additional upstream measurements (◇)

4.3.1 Overview of the velocity deficit upstream and downstream

Figure 43 depicts the normalized velocity field upstream and downstream for WF6. The measurement points are illustrated by black circles (o). In front of the disks, it is possible to observe the local blockage effect upstream of the disks. Since the measurements have been performed at x = 2D behind both rows, the contour plot is not representing the near-wake correctly and is therefore covered by a white box. At x = 2D, the wake starts to mix and has a negative magnitude. When observing further downstream at x = 6D, the velocity behind the disks in the second row is larger than the front row, and the wake recovers towards the free-stream velocity x = 12D. The jet streams between the disks separate the wakes. In this

section, the results for WF6 will be explored and analyzed.

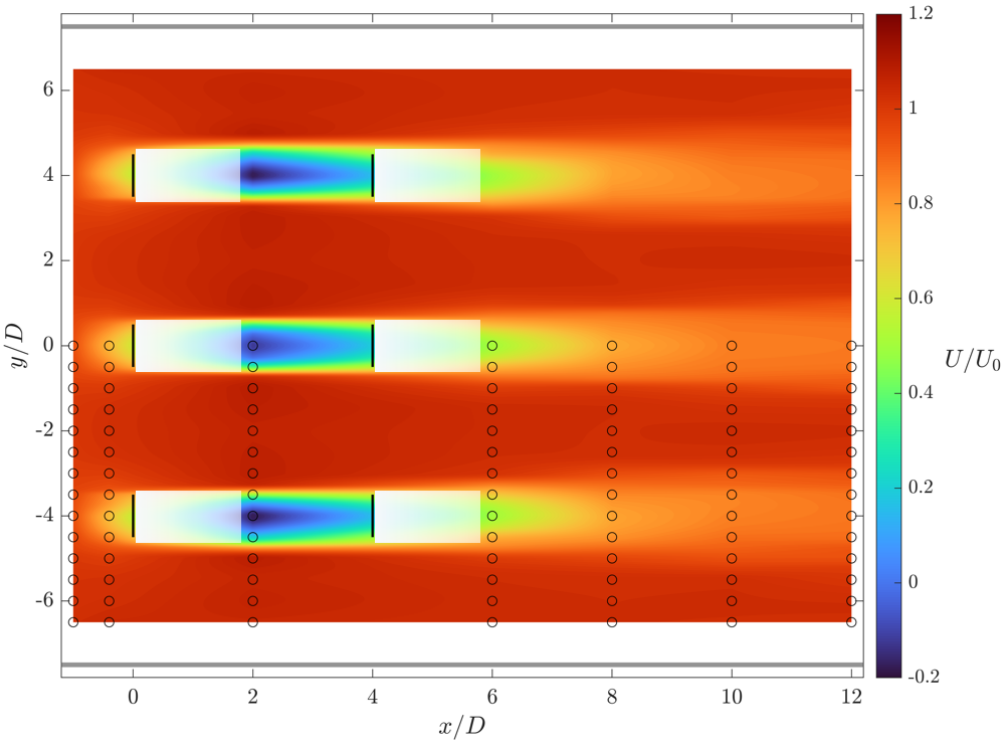

Figure 43: Normalized total velocity fields for WF6, the white boxes are present to hide the results in near wakes, which is not representative from the contour plot. The black circles illustrate the measurement points

4.3.2 Overview of the non-dimensional mean turbulent kinetic energy

Figure 44 depicts the turbulent kinetic energy development in the wake for WF6. There is no turbulent kinetic energy in the flow in front of the first row at x = -0.4D and -1D. In the wake of the front row at x = 2D, it shows that the turbulence levels are largest at the edge of the disks and that the center disk will experience more significant turbulence. Further downstream at x = 6D, the turbulence level has increased even more until it starts to decay from x = 8D to 12D, but the turbulence occurs more present in the far wake than the other setups. In between the disks and towards the walls, the non-dimensional turbulent kinetic energy is approximately equal to zero, implying that there are no eddies present in the jet streams or the bypass flow outside the arrays.

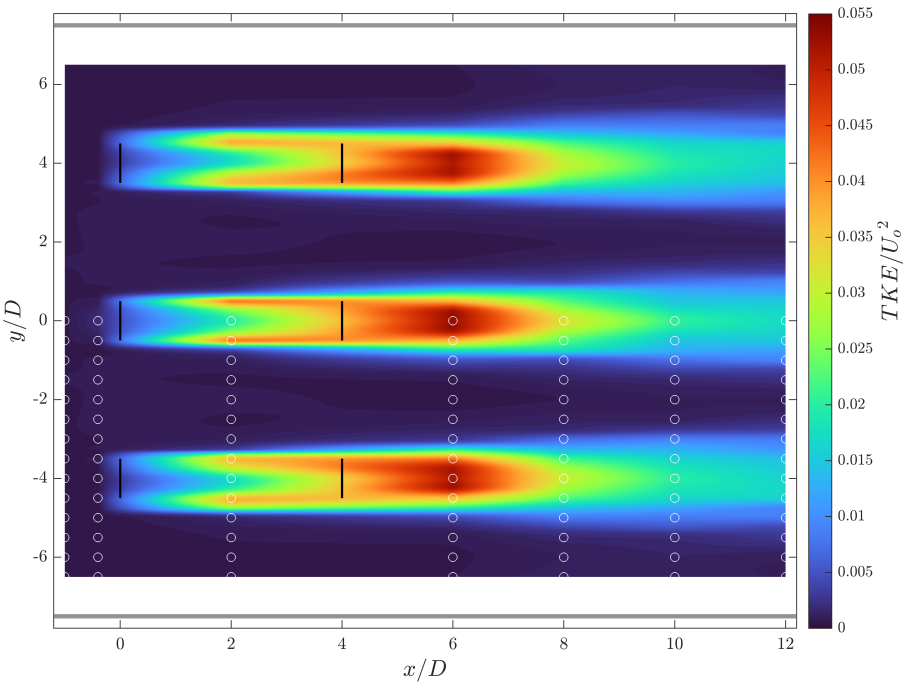

Figure 44: Contour plot of the non-dimensional mean turbulent kinetic energy development in WF6. The white circles illustrates the placement of the ADV for the conducted measurements

4.3.3 Upstream measurements

Figure 45 shows the local blockage effect for WF6 at x = -1D and -0.4D. The behavior upstream of the disks is similar to the other setups. At x = -1D, the velocity deficits at the disks are practically identical with a velocity deficit of 95%. Between the disks, the velocity increases by 2.5% due to the blockage effect. In the area between the edge disk and the walls, the velocity increases towards 4%. At x = -0.4D, the edge disk experiences a bit larger blockage than the center disk, with a velocity deficit of 73% versus 75% at the center disk. Compared to the incoming velocity, the jet stream between the disks is 2.5% higher. Near the walls, the velocity increases further to nearly 5%. It is shown that the bypass flow is increasing with a larger velocity deficit at the disks.

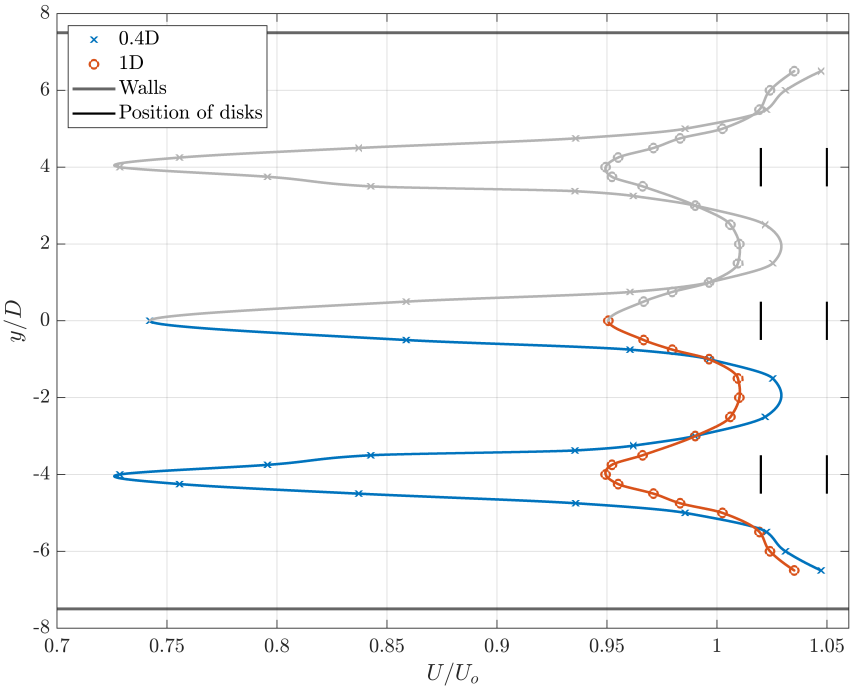

Figure 45: Upstream blockage velocity deficit at x = -0.4D and -1D for WF6, with makima interpolation between the points

4.3.4 Downstream measurements

In this section, the results for the downstream measurements will be analyzed on behalf of the velocity deficit and the non-dimensional turbulent kinetic energy development in the wake. It is split into two sections for x = 2D and 6D and x = 8D, 10D, and 12D.

x/D = 2.0 and 6.0

In Figure 46a the velocity deficit at x = 2D shows that there is a slight difference between the velocity deficit in the wakes. At the center disk, the velocity deficit is -12%, while the edge disk experience a deficit of -18%. The velocity between the disks shows that the jet streams are present. Further downstream at x = 6D, the velocity deficit is distinctly smaller, even though the distance between the second row and the ADV is 2D. Both disks experience a similar velocity deficit of 51%. The velocity in the jet streams is decreasing slightly. Figure 46b shows how the turbulence develops in the wake at the respective distances of the disks. At x = 2D, the TKE has two significant peaks due to the vortex shedding at the edge of the

disks, and the turbulence is building up. The turbulence is most effective at the edge of the outer disk. Further downstream at x = 6D, the turbulence experiences a significant increase, where the turbulence levels at both disks are nearly identical. When investigating Figure 46, it is visible that a small inflow velocity will lead to higher turbulence and velocity deficit in the wake.

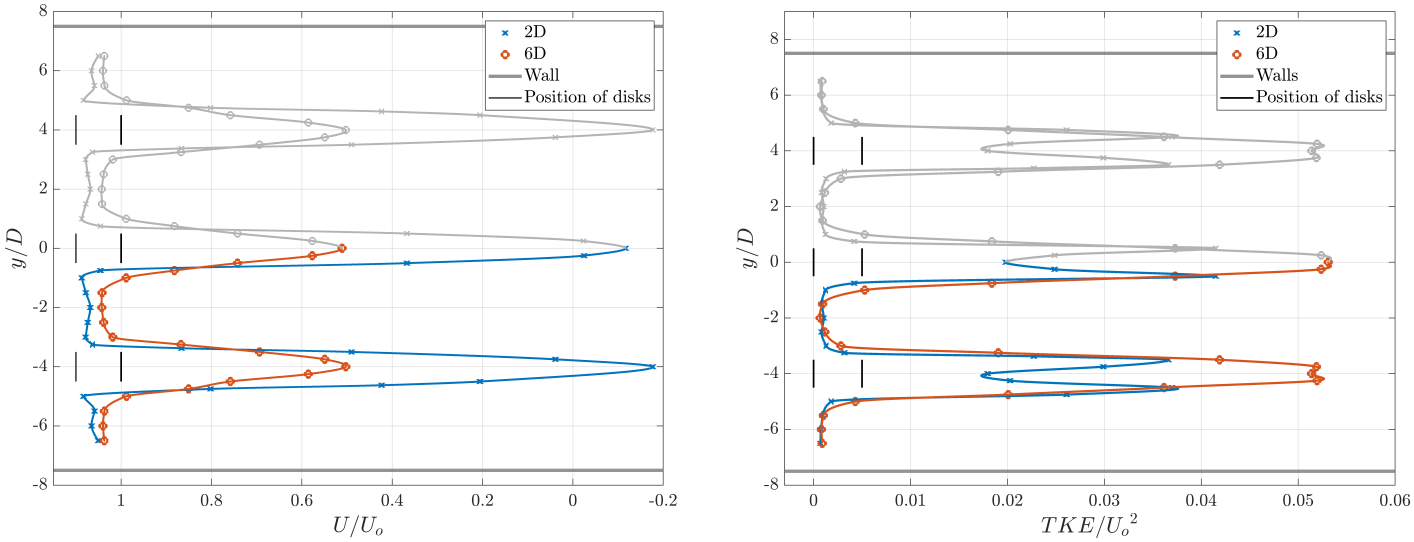

(a) Velocity deficit

(b) Non-dimensional mean turbulent kinetic energy

Figure 46: Downstream velocity deficit profiles and turbulent kinetic energy development at x = 2D and 6D for WF6 with an inline arrangement

x/D = 8.0, 10.0 and 12.0

Figure 47 shows the velocity deficit and the non-dimensional mean turbulent kinetic energy in the wake further downstream at x = 8D, 10D and 12D. When studying the velocity deficit for different distances in Figure 47a, the deficit is almost identical for the center and edge disk. At x = 8D, the velocity deficit increased to 78% behind the disks. Further downstream at x = 10D and 12D, the wake is recovering, and the velocity deficit reduces to 86% at x = 12D. Between the disks, the shape tends to change. At x = 8D, the peak is blunter than at x = 12, which becomes sharper.

Figure 47b shows the non-dimensional mean turbulent kinetic energy in the far-wake. It signifies that the turbulence is decaying further downstream in the wake. At x = 8D, the turbulence at the center is slightly larger than the edge disk, but further downstream, the magnitude is

nearly identical for both disks. When looking at the turbulence development between the disk, it is clear that the shape is similar to the velocity deficit. The peaks become narrower further downstream, but the turbulence level is the same. Indicating that the disks are operating independently and there will be no merging of the wakes.

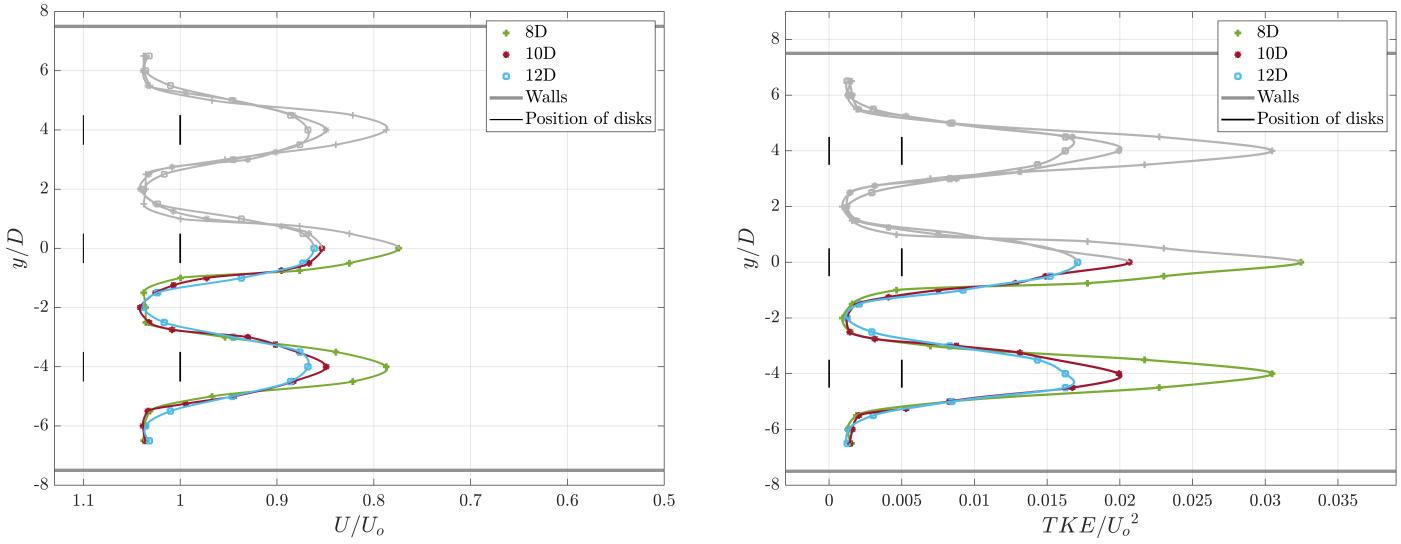

(a) Velocity deficit

(b) Non-dimensional mean turbulent kinetic energy

Figure 47: Downstream velocity deficit profiles and non-dimensional mean turbulent kinetic energy development of WF6 with an inline arrangement at x = 8D, 10D and 12D

Axial measurements

Figure 48 shows the axial development for the velocity deficit upstream and downstream at WF6, and Table 8 quantifies the velocity deficits downstream at y = 0D, 2D and 4D. The orange curve shows how the velocity develops between the center and the edge disk in the jet stream. The speed increases in front of the first row due to the disks' local blockage effect, developing further between the two rows to 6.8% above the free-stream velocity. Further downstream, the rate between the disks is stabilizing on a magnitude that is 4% larger than U_0—investigating the velocity deficit in the centerlines of the disks illustrated with blue and green lines, showing a similarity in the development for almost all distances. Upstream the front row, the blockage effect is distinct, and the velocity deficit increases towards the disks. In between the two arrays at x = 2D, the edge disk at y = 4D experiences a more significant velocity deficit than the center disk, with 6.0%. Behind the second row at x = 6D, the wake starts to recover. At x = 10D,

the velocity stabilizes at 85% of the inflow velocity, and it is only increasing with under 0.2% towards x = 12D.

Table 8: Axial velocity deficits downstream for WF6

x/D	y = 0D	y = 2D	y = 4D
2	-0.117	1.068	-0.177
6	0.511	1.043	0.503
8	0.774	1.036	0.787
10	0.854	1.041	0.849
12	0.862	1.038	0.868

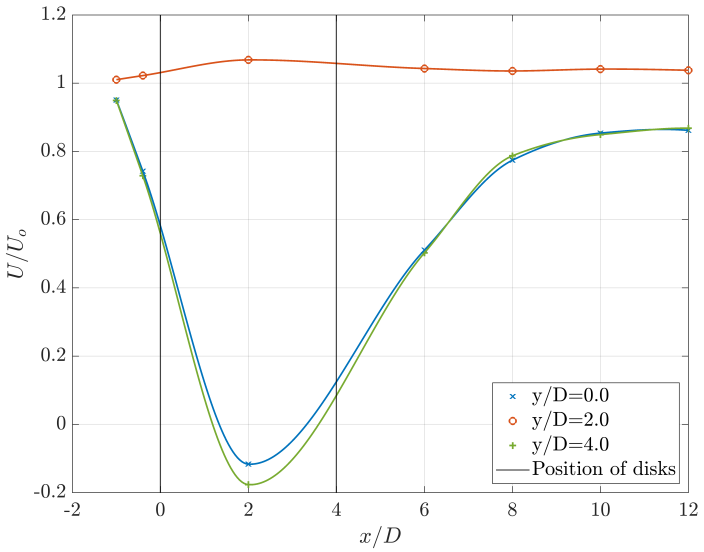

Figure 48: Axial velocity deficit development upstream and downstream at at y = 0D, 2D and 4D for WF6

5 Discussion

This chapter aims to discuss the results from the conducted test and compare them to the other setups, as well as to connect the previously presented theory to the results.

5.1 Upstream measurements

Evaluating the upstream velocity deficit shows that the local blockage effect impacts the velocity in front of the disks for all setups. Table 9 presents the velocity deficit at x = -1D and -0.4D in front of the center disk (y = 0D), in the jet streams between the disks (y = 2D), at the edge disk (y = 4D) and in the bypass flow (y = 6D). It is possible to notice from the table that velocity deficits at x = -1D show a resemblance of approximately 95% for the center and edge disk. When investigating the jet streams between the disks at y = 2D, WF5 experiences a 1% higher velocity increase than WF6 and WF7. Further towards the disks at x = -0.4D, the velocity deficit for WF6 is largest with 74% and 73% for the center and edge disk. For the laterally offset arrangements in WF5 and WF6, the velocity deficit is almost identical, where the velocity deficit for edge disks is 2% larger than the center disk. The flow between the disks at y = 2D shows a similarity in all the setups with a small increase in the jet streams by 2-4%.

Table 9: Upstream velocity deficit at y = 0D, 2D, 4D and 6D for the different setups at x = -0.4D and -1D

		y = 0D	y = 2D	y = 4D	y = 6D
WF5	x = -1D	0.954	1.014	0.949	1.028
	x = -0.4D	0.793	1.037(*)	0.772	1.037
WF7	x = -1D	0.953	1.011	0.952	1.029
	x = -0.4D	0.796	1.023	0.777	1.028
WF6	x = -1D	0.951	1.010	0.949	1.024
	x = -0.4D	0.742	1.024	0.729	1.031

* Due to a local minimum at y = 2D for WF5 the average for the three points in the peak represents the velocity deficit at this point.

The experiments performed by Hägglund [14] and Dahlberg & Seaglini [15] showed that all the turbines in the first row experienced a velocity decrease. Still, it was lower at the edges, and they concluded that the edge disks were less affected by the blockage effects. The conducted

experiments in this thesis indicate that the disk on the edge experiences a larger decrease than the center disk. This does not correspond with the theory presented in Section 2.4. An explanation for this is that the distance from the edge disk in the front row to the walls in the water tank is the same as between the disks, indicating that the edge disk in the array will not act as an actual edge disk. Although the velocity decrease on the edge disk is more significant than the center, the difference between the deficits in WF6 and WF7 are relatively small, with around 1-2%. From Table 9 the dissimilarity for the three setups is largest at x = -0.4D, where the velocity deficit for the disks in WF6 is 5% higher than WF5 and WF7. The disks in WF7 are experiencing the smallest deficit in all setups. This corresponds with the theory from Garrett & Cummings [11], where a more extensive blockage of a channel can result in a reduced velocity deficit upstream of the disks. The opposite tendency appears for WF6, where a minor blockage leads to a larger velocity deficit.

Figure 49 shows a comparison of the upstream velocity deficit for the center disk at x = -1D for SR [18], WF3 [19], WF5, WF6 and WF7. WF3 shows a slightly larger decrease in the velocity in front of the center disk, and it looks like it has a displacement to the rest of the setups. At the same time, the shape and the tendency are similar for all the different setups. The little drop for SR at x = 0D can be caused by the edges and holes in the actuator disk. For WF5, the jet streams between the disks are larger than for the other setups. The figure depicts this with a steeper gradient as the velocity increases.

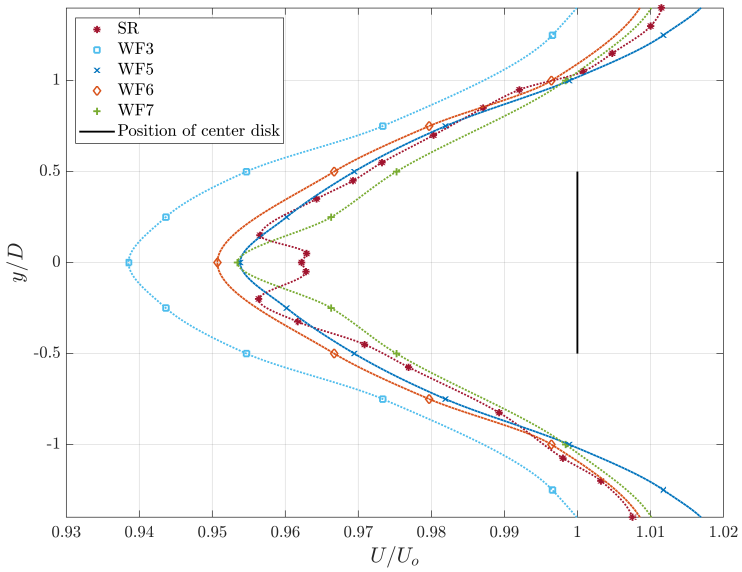

Figure 49: Comparison of upstream velocity deficit for SR, WF3, WF5, WF6 and WF7 at x = -1D

5.2 Downstream measurements

When analyzing and comparing the downstream measurements for the three setups, the development for the laterally offset arrangements shows a similarity. In addition, WF6 shows a similar pattern to WF3. Therefore, it will be logical to compare WF5 to WF7 and WF6 to WF3.

5.2.1 Comparison of WF5 and WF7

Figure 50 shows how the wake develops behind the disks in WF5 and WF7. At x = 2D, the velocity deficit for the jet streams between the disks at y = 2D is similar for both setups, while the jet streams for WF7 at y = 6D are slightly smaller. At x = 2D, the velocity deficits are almost identical for both setups, with a deficit of -14%, the exception being the edge disk in WF5, where the deficit is -8%. The negative velocity deficit implies a reversed flow in the wake. This corresponds to the findings of Helvig et al. [20], as the significant blockage from the disks induced an area of reversed flow in the wake. When investigating the velocity deficits for the different setups in Figure 50, it is possible to observe that the edge disks experience a higher velocity deficit in all of the cases, except for the edge disk in the front row of WF7 (y = 4D). It is not a clear explanation for this observation. But for WF5, it can relate to the presence of more free-stream flow in the second row, leading to more mixing in the wake that again leads to a more significant velocity deficit and a slower recovery for the wake. For WF7, this is not the case. From Figure 50 it is possible to observe a 2% difference in the velocity deficit in the jet streams that hit the disks in the second row. From Section 2.1, it was shown that a small inflow velocity would result in a smaller velocity in the wake, leading to a higher velocity deficit. Another explanation is the presence of the walls preventing the wake from recovering and slowing down the recovery of the wake.

Further downstream, the velocity deficit at x = 8D in the wake of the front row, WF5 has a slightly larger velocity deficit than WF7. In the second row, the edge disks are still experiencing a higher velocity deficit than the center disk in WF7 towards x = 12D, with one exception. At x = 10D, the velocity deficit for the disk in WF5 is similar to the center disk in WF7. At x = 12D, the wake behind the disks in the front row for WF7 has recovered towards 96% and 95%, in contrast to 92% and 91% for WF5. This corresponds to the theory presented by Ouro &

Nishino [17], where they observed that for arrays with a lower blockage ratio, the wake recovery developed slower and that the recovery in the near wake was faster. The trend in the near wake is not observed because of the lack of measurements in this area. Still, it is observed that the wake recovery in the far wake for WF5 is slightly slower than for WF7 when investigating the velocity deficit at x = 12D.

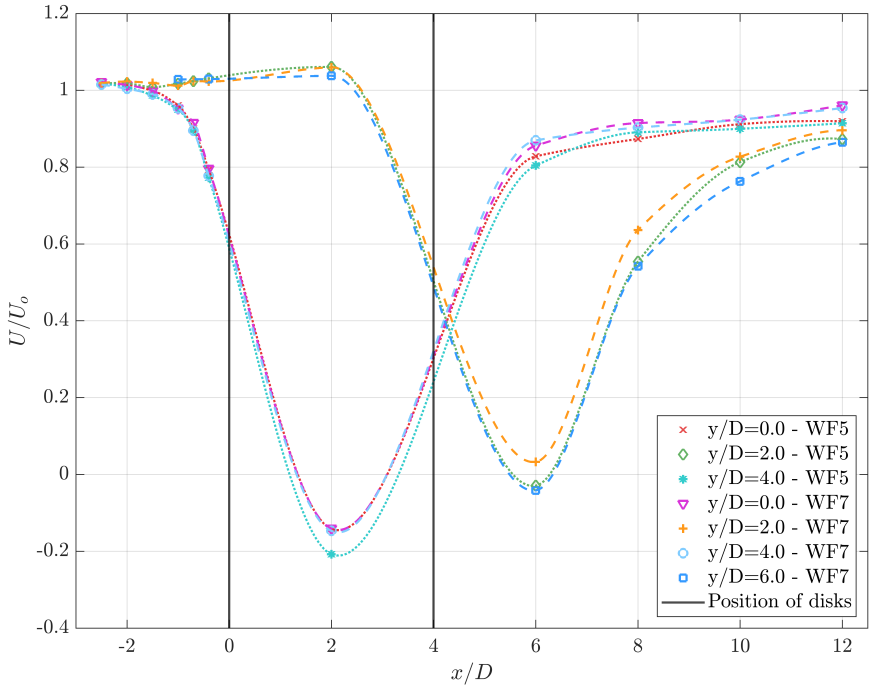

Figure 50: Comparison of the velocity developments upstream and downstream at y = 0D, 2D and 4D for WF5 (dotted lines) and WF7 (dashed lines)

Figure 51 shows how the turbulent kinetic energy develops in the wake of WF5 and WF7. The turbulence behind the disks in the front row shows a similar development. The difference is that WF7 experiences slightly higher turbulence levels at x = 2D. Further downstream, the turbulence levels behind the front row for WF5 and WF7 follow the same pattern, with almost identical magnitudes. The exception occurs at x = 12D, where the turbulence levels in the wake of WF7 are smaller than WF5. There is a significant difference in the peaks for the turbulence levels behind the front row and the second row. This is caused by a lack of measurements between x = 2D and x = 6D. As the turbulence reaches its maxima at x = 8D behind the second row, it is assumed that the turbulence levels behind the front row will experience higher magnitudes around x = 4D.

The non-dimensional mean turbulent kinetic energy behind the disks in the second row shows different behavior. At x = 6D, the turbulence levels in the wake of the center disk for WF7 are higher than the disk in WF5 and the edge disk in WF7. Further downstream at x = 8D, the development changes, and the turbulence levels for the disk in WF5 have become larger than the disks in WF7 when reaching their maxima. While the turbulence in the wake at x = 10D is decaying, the edge disk in WF7 experiences higher turbulence levels than the two other disks. At x = 12D, the turbulent kinetic energy in WF7 has decayed faster than WF5, and the turbulence levels in the wake of the disk in WF5 are higher than the disks in WF7. The figure also shows that the turbulence behind the center disk in the second row for WF7 has a steeper gradient towards its maximum than WF5 and the edge disk in WF7. This indicates that the turbulence in the wake of the center disk in WF7 builds up faster. The edge disk in WF7 and WF5 experiences a slower build-up towards its peaks. The turbulence levels for the center disk in WF7 decays faster than the other two disks.

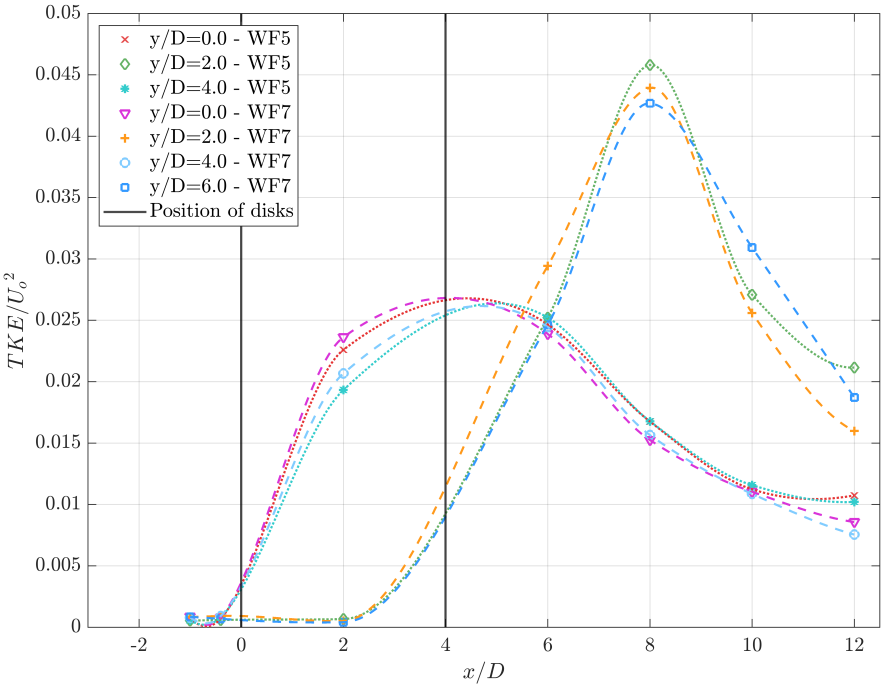

Figure 51: Comparison of the turbulent kinetic energy development upstream and downstream at y = 0D, 2D and 4D for WF5 (dotted lines) and WF7 (dashed lines)

The development of the non-dimensional mean turbulent kinetic energy behind the edge disk in WF7 is better presented in Figure 40a. It depicts how the turbulence behind the edge disk is developing slower due to the walls in the tank. The effect from the walls is still noticeable from Figure 51 at x = 10D to 12D, where the turbulence levels are higher than the center disk — indicating that the disk in the middle experience a higher level of turbulence, as well as faster recovery, compared to the disk on the edge. Similar to the observations from Ouro et al. [16]. They observed that the second row operated in a highly turbulent wake of the upstream turbines. The edge turbines operated partially in the highly turbulent wake and were influenced by the ambient free-stream flow, which led to significant turbulence further downstream. Regarding the turbines in the middle, their wake developed with high turbulence levels and decayed faster as they were surrounded by the shear layers formed from the edge turbines with high turbulence levels.

5.2.2 Comparison of WF3 and WF6

With an additional row behind WF3 placed 4D downstream, the development of the wake changes as shown in Figure 52. It must be mentioned that Bjørnsen [19] conducted more measurements for WF3, which results in a more detailed development for the velocity deficit in the wake. The jet streams between the disks are almost identical for the two setups. For WF3, the velocity deficit is largest at x =1D. The additional row at x =4D that creates WF6 affects the velocity deficit at x = 2D to be slightly larger than WF3. Therefore it is possible to assume that the velocity deficit for WF6 is even larger between the disk and x = 2D. The wake loss for the center disk and edge disk in WF3 is similar for all x/D, unlike WF6. Like the other setups(WF5 and WF7), the edge disk has a 6.0% higher velocity deficit than the center disk at x = 2D. The most interesting detail from the figure is that the velocity deficit behind the second row is 51% at x = 6D. An explanation for the lower deficit could be the short distance between the rows that prevent the wake from recovering, leading to a smaller velocity in the flow approaching the downstream turbines. In addition, the low-speed flow in the wake of the upstream row due to the high turbulence levels in the wake leads to a smaller wake loss in the second row. Further downstream, for both setups, recover. When comparing the velocity deficit of WF3 and WF6, they are similar at x = 5.5D and 8D, with a 78% velocity deficit—showing

that the velocity deficit for WF3 is decreasing slightly faster than for WF6. Bjørnsen conducted measurements towards 9.5D downstream, where the velocity deficit was 91%. For WF6, the measurements were performed at 12D, resulting in a velocity deficit of 86%. This indicates that the additional row in the wake of the front row does not lead to a larger velocity deficit in the near wake for the second row, but a slower wake recovery towards U_0 in the far wake.

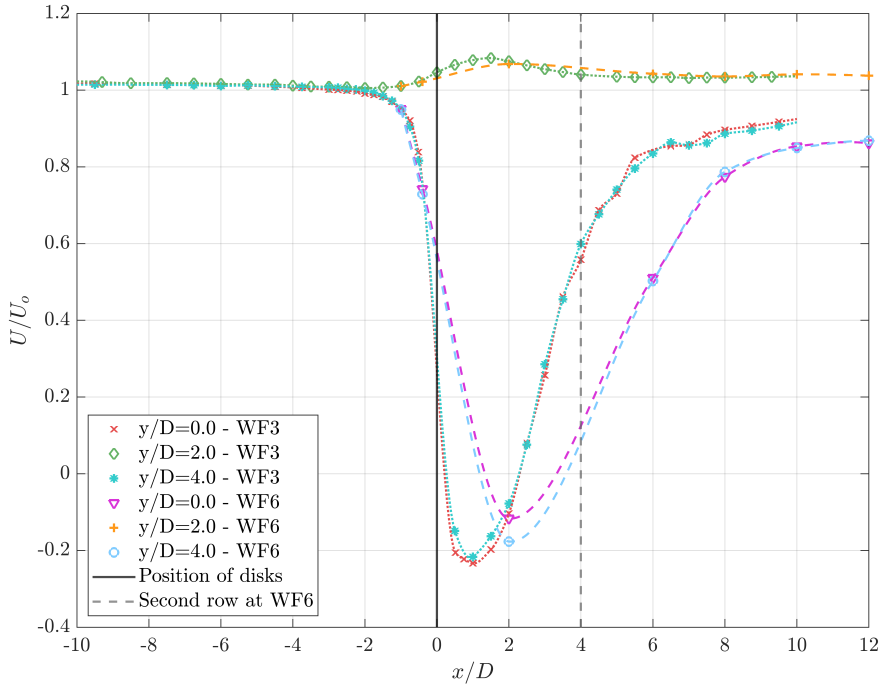

Figure 52: Comparison of the velocity developments upstream and downstream at y = 0D, 2D and 4D for WF3 (dotted lines) and WF6 (dashed lines), where the dashed line at x =4D represents the second row of turbines in WF6

When comparing the turbulent kinetic energy in the wake for the two different setups from Figure 44 and 24b, the turbulence levels for WF6 is more significant due to the disks in the second row that operates in the wake. Where WF6 has the highest turbulence levels at x = 6D, and WF3 at x = 4D. It is also clear that the turbulence levels for WF6 are higher than WF3 in the far wake. This indicates that WF6 has a slower wake recovery than WF3.

5.3 Comparing the three wind farm arrangements

To summarize the findings from the results for the conducted experiments, Figure 53 shows how the velocity deficit in the different arrays develop from x = -2.5D towards 12D for WF5, WF6, and WF7. The flow upstream of the front row shows similar behavior for all three setups, where WF6 experiences a slightly larger velocity deficit at x = -0.4D. The jet streams have an identical development towards x = 2D before the flow hits the disks in the second row for the laterally offset arrangements. For WF6, the jet stream shows a slightly larger velocity than U_0, but it decreases towards this magnitude further downstream at x = 12D. At x = 2D, the velocity behind the edge disk and center disk in the front row are similar for all the setups, as the flow reverses behind the disks, similar to the findings of Helvig et al. [20]. However, the velocity deficit is most significant for WF6. This corresponds to the observations performed by Ouro & Nishino [17]. They observed that the high-speed streaks in the jet streams for aligned setups resulted in a larger velocity difference between the wake and the bypass flow.

Moving further downstream, the shape of the velocity deficit tends to change for the laterally offset and the aligned arrangements. As the wake for WF6 slowly recovers towards 85% at x = 12D, not significantly affected by the presence of the second row placed in the wake of the front row. The velocity deficit behind the second row for WF5 and WF7 at x = 6D is smaller than the front row at x = 2D. The center disk in WF7 is showing a smaller velocity deficit than the other disks in the second row in WF7 and WF5. At x = 12D wake for the center disk in WF7 has recovered towards 90% which is 2% higher than the edge disk in WF7 and disk in WF5. A reason for this can be the different turbulence levels in their wakes, which will be further investigated.

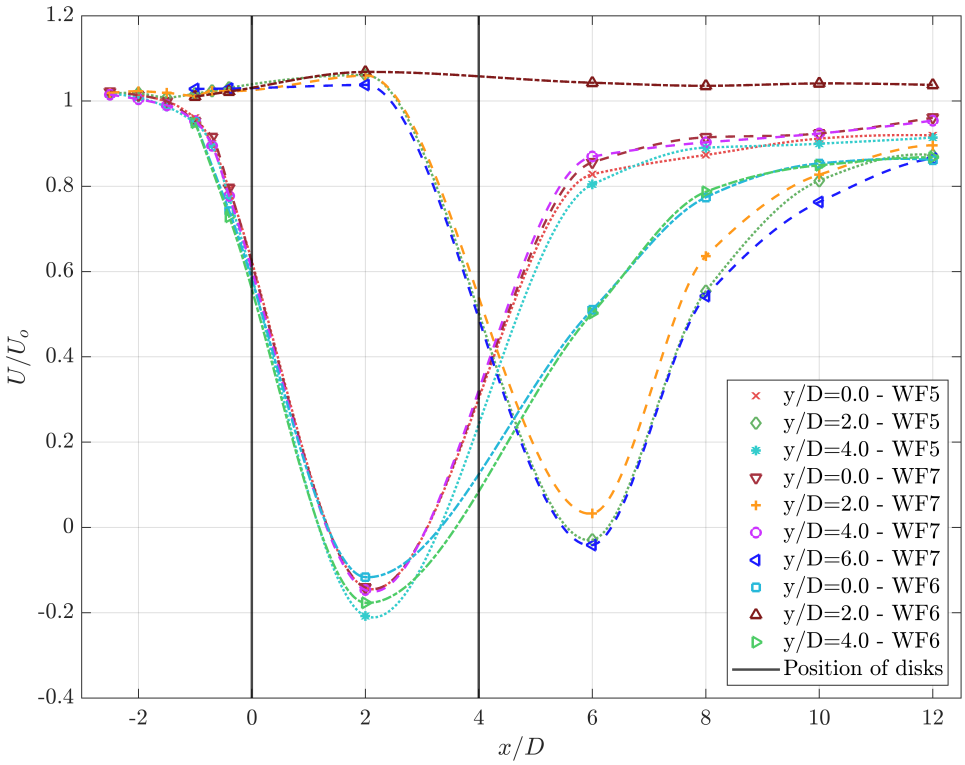

Figure 53: Comparison of the axial velocity developments upstream and downstream at y = 0D, 2D, 4D and 6D for WF7 (dashed lines) and y = 0D, 2D and 4D for WF5 (dotted lines) and WF6 (fine lines)

The development of the turbulent kinetic energy in the wake can explain how the recovery for the different setup occurs and is shown in Figure 54. The turbulent kinetic energy upstream for WF5, WF6, and WF7 is approximately zero, similar to the jet streams between the disks at x = 2D. Behind the disks in the front row, the turbulence levels for the different wind farms are almost identical, but it is highest at the center disk in WF7 and smallest for the edge disk in WF6. At x = 6D significant differences occur, the turbulence in WF6 has built up towards its maxima. While the turbulence levels in the wakes of the disks in the front row for WF5 and WF7 have started to decay at this point, it is possible to observe that the turbulence levels in the wake behind the second row are building up. At x = 6D, the center disk in WF7 builds up faster than the edge disk in WF7 and the disk WF5, which have an identical development. At x = 8D, the laterally offset wind farm arrangements have reached their maxima, and the turbulence levels for the disk in WF5 have become larger than the disk in WF7. Further downstream, the turbulence in the wakes is decaying towards x = 12D, where the center disk in WF7 shows a faster recovery than WF5 in the second row. The turbulence levels in the wakes of the first row show that both cases are recovering with a similar pattern, but for WF7, the

turbulence levels at x = 12D are slightly smaller than for WF5. The turbulent kinetic energy in WF6 is decaying towards x = 12D, but the turbulence is still present at this point in the far wake.

The differences in the turbulent kinetic energy for the three cases are interesting to analyze. The turbulence levels are highest in the wake of the second row at WF6 at x = 6D. At the same time, the turbulent kinetic energy in the wake for the center disk in WF7 is decaying faster in the far wake, as shown with its steep gradient, in addition to the lowest maximum magnitude for the three different setups. This corresponds to the theory presented by Ouro et al. [16] indicating that the wake for turbines surrounded by shear layers from edge turbines tends to decay faster. Ouro & Nishino [17] experienced that the turbulence levels for aligned arrays were significantly more extensive than for the laterally offset arrays. It shows that a larger blockage ratio in a channel would reduce the turbulence intensity in the wake. These findings agree with the results from the conducted experiments in this thesis.

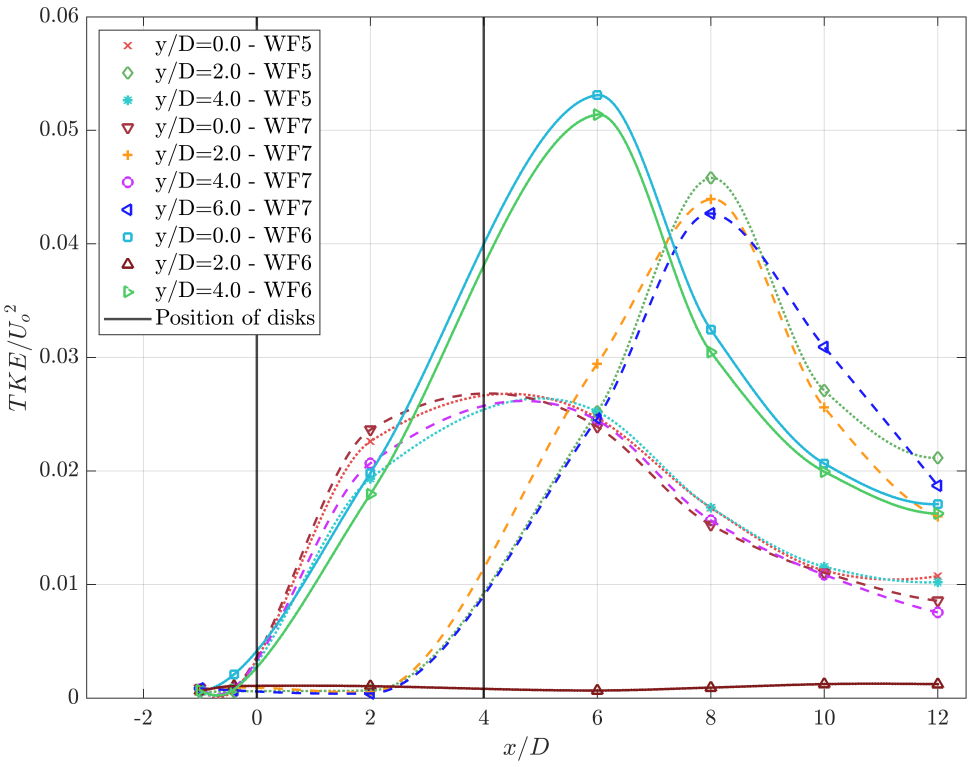

Figure 54: Comparison of the axial turbulent kinetic energy development upstream and downstream at y = 0D, 2D, 4D and 6D for WF7 (dashed lines) and y = 0D, 2D and 4D for WF5 (dotted lines) and WF6 (fine lines)

6 Conclusions

Experimental upstream and downstream measurements have been performed in the towing tank in the MarinLab at HVL. To investigate how the wake and blockage effects work on three different layouts. The front row consists of three actuator disks with a lateral distance of 4 diameters and a second row 4 diameters downstream with a variation of two to four disks with the same lateral distance. Simplified actuator disks have been used to generate satisfying mean flow properties around a turbine.

The results show that the upstream blockage effects, characterized by flow measurements in the upstream induction zone for the three different wind farms, are very similar. However, velocity deficits of different magnitude and recovery rates have been assessed in the wakes of the different wind farms. When analyzing the upstream velocity measurements, it is visible that the velocity upstream of the first row decreases in front of the disks. The magnitudes of the velocity deficit for the edge and center disk are similar in all cases, and the transverse velocity profiles at x = -1D are almost identical for the different wind farms. When approaching the disks at x = -0.4D, the velocity deficit for WF6 with an aligned arrangement shows a more significant velocity deficit than for the cases with a larger blockage ratio at WF5 and WF7. In addition, WF5 experiences slightly larger jet streams and bypass flow upstream of the array.

The downstream wake velocity measurements at x = 2D show that WF6 experiences the highest velocity deficit behind the first row. As expected, the aligned and laterally offset arrangements differ in the recovery of the wake. For WF5 and WF7, the velocity deficit behind the second row is smaller than the front row. In addition, the velocity deficit for the edge disk in WF5 is 6% higher than the center disk in WF7 behind both rows. Further downstream, the wake recovers towards x = 12D, and it is observed that the velocity in the wake for the center disk in WF7 is closer to the inflow velocity than the other laterally offset disks, indicating a faster recovery. For WF6, the velocity deficit behind the second row is unclear since it looks like the wake recovers. However, compared to the results of Bjørnsen [19] the second row delays the recovery of the wake. At x = 12D, the velocity deficit is largest for WF6 and the edge disk in WF7. An explanation for the edge disk in WF7 is the presence of walls that prevent the wake from recovering. The turbulent kinetic energy in the wake is the highest for WF6, at x = 6D.

For the laterally offset arrangements, the highest turbulence levels occur at x = 8D, where the turbulence is highest in WF5, while the turbulence in WF7 decays faster.

Overall, the setup with the smallest blockage ratio (WF6) shows the most significant velocity deficit upstream, a slower wake recovery, and the highest turbulence levels in the wake. On the other hand, the setup with the highest blockage ratio (WF7) shows a slightly smaller velocity deficit upstream than the different setups. In the far wake, the center disk in WF7 has almost recovered towards 90% of the magnitude for the free-stream velocity. This confirms that the wake for a disk surrounded by shear layers from edge disks will have a faster wake recovery. To sum up the observations from the conducted experiments, the arrangement for a wind farm is essential to optimize the wind farm flows, minimizing the velocity deficits upstream and generating a faster recovery for the wake.

7 Suggestions for further work

When analyzing the results from the performed experiments in this thesis, a number of new challenges for wind energy installations arise. While getting a better understanding of how turbines in a farm affect the flows upstream and downstream, new details have come to mind that could require further investigation.

When conducting measurements for the different arrangements, it was desirable to investigate the wind farm flows. Therefore, in general, the tests have been performed to see how the far wake recovers. Therefore, it could be interesting to analyze how the near-wake for the front row and the second row differs and research how the blockage effect in the second row tends to behave. In addition to investigating the velocity deficits in the wind farm flows, it could be interesting to explore how the axial forces on the disks. Furthermore, exploring how a difference in the thrust force, i.e., different towing speeds affects the behavior of the wakes, could be an interesting study. It would also be desirable to perform the tests using other measurement methods.

Furthermore, this set of experimental data should act as a database for validating analytical and numerical flow models and software tools, such as computational fluid dynamics, to ensure that they predict the correct aerodynamic behavior of the wind farm flows.

References

[1] United Nations Environment Programme, "Green Energy Choices: The benefits, risks and trade-offs of low-carbon technologies for electricity production," 2016.

[2] IEA, "Global Energy Review 2021," 2021. [Online]. Available: https://www.iea.org/reports/global-energy-review-2021

[3] Global Wind Energy Council, "GWEC| Global Wind Report 2021," *Global Wind Energy Council: Brussels, Belgium*, 2021, accessed: 16 august 2021. [Online]. Available: https://gwec.net/wp-content/uploads/2021/03/GWEC-Global-Wind-Report-2021.pdf

[4] J. Bleeg, M. Purcell, R. Ruisi, and E. Traiger, "Wind Farm Blockage and the Consequences of Neglecting Its Impact on Energy Production," *Energies*, vol. 11, no. 6, 2018. [Online]. Available: https://www.mdpi.com/1996-1073/11/6/1609

[5] T. Wizelius, "Vindkraft i teori och praktik," Lund, 2003.

[6] Siemens Gamesa Renewable Energy, "The SG 14-222 DD," May 2020, accessed: 16 august 2021. [Online]. Available: https://www.siemensgamesa.com/newsroom/2020/05/200519-siemens-gamesa-turbine-14-222-ddhttps://www.siemensgamesa.com/newsroom/2020/05/200519-siemens-gamesa-turbine-14-222-dd

[7] Midtfjellet vindpark. Vindparken. [Online]. Available: https://midtfjellet.no/vindparken/

[8] E. Zander, "Wind power, capacity, watts and kilowatt hours – how is it all connected?" 2011, accessed: 8. September 2021. [Online]. Available: http://www.ewea.org/blog/2011/01/wind-power-capacity-watts-and-kilowatt-hours-\T1\textendash-how-is-it-all-connected/

[9] Global Wind Energy Council, "Global Offshore Wind Report 2020," *Global Wind Energy Council: Brussels, Belgium*, 2020, accessed: 16 august 2021. [Online]. Available: https://gwec.net/wp-content/uploads/2021/03/GWEC-Global-Wind-Report-2021.pdf

[10] D. Medici, S. Ivanell, J.-Å. Dahlberg, and P.-H. Alfredsson, "The upstream flow of a wind turbine: Blockage effect," *Wind Energy*, vol. 14, pp. 691 – 697, 07 2011.

[11] C. Garrett and P. Cummins, "The efficiency of a turbine in a tidal channel," *Journal of Fluid Mechanics*, vol. 588, pp. 243 – 251, 10 2007.

[12] T. Nishino and R. Willden, "The efficiency of an array of tidal turbines partially blocking a wide channel," *Journal of Fluid Mechanics*, vol. 708, pp. 596–606, 10 2012.

[13] T. Nishino and S. Draper, "Local blockage effect for wind turbines," *Journal of Physics: Conference Series*, vol. 625, p. 012010, jun 2015. [Online]. Available: https://doi.org/10.1088/1742-6596/625/1/012010

[14] P. B. Hägglund, "An Experimental Study on Global Turbine Array Effects in Large Wind Turbine Clusters," 2013.

[15] A. Segalini and J. Dahlberg, "Blockage effects in wind farms," *Wind energy (Chichester, England)*, vol. 23, no. 2, pp. 120–128, 2020.

[16] P. Ouro, L. Ramirez, and M. Harrold, "Analysis of array spacing on tidal stream turbine farm performance using Large-Eddy Simulation," *Journal of Fluids and Structures*, vol. 91, p. 102732, 12 2019.

[17] P. Ouro and T. Nishino, "Performance and wake characteristics of tidal turbines in an infinitely large array," *Journal of Fluid Mechanics*, vol. 925, p. A30, 08 2021.

[18] R. Garnes, J. W. Jensen, and A. Rogne, "Upstream blockage and downstream wake flow of a wind turbine," 2020. [Online]. Available: https://hdl.handle.net/11250/2679277

[19] J. R. Bjørnsen, "Blockage and wake effects for three laterally spaced wind turbines rotors with lab-scale measurements," 2021.

[20] S. d. J. Helvig, M. K. Vinnes, A. Segalini, N. A. Worth, and R. J. Hearst, "A comparison of lab-scale free rotating wind turbines and actuator disks," *Journal of wind engineering and industrial aerodynamics*, vol. 209, p. 104485, 2021.

[21] M. O. L. Hansen, *Aerodynamics of wind turbines*, 2nd ed. Earthscan, 2008.

[22] J. Manwell, "Wind energy explained : theory, design and application," Chichester, 2009.

[23] "Understanding Coefficient of Power (Cp) and Betz Limit," accessed 21.04.2021. [Online]. Available: http://cdn.teachersource.com/downloads/lesson_pdf/betz_limit_0.pdf

[24] M. Hansen, C. Leikvoll, and M. Vikse, "Multirotor wind turbine - drag," 2021. [Online]. Available: https://hdl.handle.net/11250/2762835

[25] H.-J. Wagner and J. Mathur, *Introduction to Wind Energy Systems: Basics, Technology and Operation*. Cham: Springer International Publishing AG, 2017.

[26] P. Hashemi Tari, K. Siddiqui, and H. Hangan, "Flow characterization in the near-wake region of a horizontal axis wind turbine: Near-wake flow characterization of a horizontal axis wind turbine," *Wind energy (Chichester, England)*, vol. 19, no. 7, pp. 1249–1267, 2016.

[27] C. Steiness. Horns Rev Offshore Wind Farm, Denmark. [Online]. Available: https://i.imgur.com/qruVcnu.jpg

[28] T. Göçmen, P. van der Laan, P.-E. Réthoré, A. P. Diaz, G. C. Larsen, and S. Ott, "Wind turbine wake models developed at the Technical University of Denmark: A review," *Renewable and Sustainable Energy Reviews*, vol. 60, pp. 752–769, 2016. [Online]. Available: https://www.sciencedirect.com/science/article/pii/S136403211600143X

[29] B. Sanderse, "Aerodynamics of wind turbine wakes literature review," 2009.

[30] Z. Shao, W. Ying, L. Li, S. Han, and L. Yongqian, "Multiple Wind Turbine Wakes Modeling Considering the Faster Wake Recovery in Overlapped Wakes," *Energies*, vol. 12, p. 680, 02 2019.

[31] E. Branlard and A. R. Meyer Forsting, "Assessing the blockage effect of wind turbines and wind farms using an analytical vortex model," *Wind Energy*, vol. 23, no. 11, pp. 2068–2086. [Online]. Available: https://onlinelibrary.wiley.com/doi/abs/10.1002/we.2546

[32] P. A. Lynn, "Onshore and offshore wind energy : an introduction," Chichester, 2012.

[33] T. M. Letcher, *Wind Energy Engineering - A Handbook for Onshore and Offshore Wind Turbines*. Elsevier, 2017. [Online]. Available: https://app.knovel.com/hotlink/khtml/id:kt011FU2D4/wind-energy-engineering/case-study-westermost

[34] A. Olczak, T. Stallard, T. Feng, and P. K. Stansby, "Comparison of a RANS blade element model for tidal turbine arrays with laboratory scale measurements of wake velocity and rotor thrust," *Journal of Fluids and Structures*, vol. 64, pp. 87–106, 2016. [Online]. Available: https://www.sciencedirect.com/science/article/pii/S088997461530058X

[35] S. Steen, *Motstand og propulsjon propell- og foilteori.* NTNU Trondheim - Institutt for marin teknikk, 2007.

[36] V. L. Okulov, R. F. Mikkelsen, I. V. Naumov, I. V. Litvinov, E. S. Gesheva, and J. N. Sørensen, "Comparison of the far wake behind dual rotor and dual disk configurations," 2016.

[37] J. I. Whelan, J. M. R. Graham, and J. Peiró, "A free-surface and blockage correction for tidal turbines," *Journal of Fluid Mechanics*, vol. 624, p. 281–291, 2009.

[38] Høgskulen på Vestlandet, "MarinLab," https://www.hvl.no/en/about/marinlab/, Hentet 06.08.2020. [Online]. Available: https://www.hvl.no/en/about/marinlab/

[39] Nortek, *The Comprehensive Manual for Velocimeters*, Nortek, Nov. 2018, accessed: 16.03.2021. [Online]. Available: N3015-030-Comprehensive-Manual-Velocimeters_1118.pdf

[40] MathWorks, "makima." [Online]. Available: https://www.mathworks.com/help/matlab/ref/makima.html#mw_e8ee1c8c-2cc3-46c4-90c4-c3208804ff4e